THE IMPLEMENTATION OF QUANTUM DOTS IN PHOTOVOLTAICS: FROM SEMICONDUCTOR-PLASMON INTERACTIONS TO CURRENT VISUALIZATION

By

J. Scott Niezgoda

Dissertation

Submitted to the Faculty of the

Graduate School of Vanderbilt University

in partial fulfillment of the requirements

for the degree of

DOCTOR OF PHILOSOPHY

in

Chemistry

May 2015

Nashville, TN

Approved:

Sandra J. Rosenthal, Ph.D.

David E. Cliffel, Ph.D.

Janet E. Macdonald, Ph.D.

Ronald D. Schrimpf, Ph.D.

To my brothers and parents, an outstanding bunch

and

To the most perfect woman I know, Anita

ACKNOWLEDGEMENTS

The work presented in this dissertation would not have been possible without financial support from the National Science Foundation EPSCoR program, and TN-SCORE in particular, which allowed me to perform research and establish significant community outreach relationships.

First, Sandy: you must have seen something in me from the get-go (please don't say it was my heritage); you gave me a shot and gave me confidence to pave my own path. You have allowed my colleagues past and present, and me personally to retain a sense of self during the arduous graduate process. Your understanding, cool headedness and humor are precious things for a PI to possess. Plus, you've taught me how to save lots of time by writing next to nothing in emails. Thank you, truly, I am proud to be a part of your research tree.

I must also thank my committee profusely. I never expected, when entering graduate school, that I could have such a supportive and engaging Ph.D. committee. To Dr. David Cliffel, your perspectives are seemingly endless and although your obligations to other students' committees are endless as well, you are always engaging and sharp. Dr. Janet Macdonald, getting to know you over past 5 years has been a sincere joy. You've given me perspective on what I myself strive to accomplish and your utter enthusiasm is contagious. And Dr. Ronald Schrimpf, the most fortunate choice I made early in my graduate career was to take your course. You exposed me to a subject matter to which I was instantly hooked and the likes of which could not have been presented more elegantly (I finally used it, Chapter IV!).

Thanks to all my Rosenthal group members for enduring me and for your friendship, I wish you all the very best. Especially to my desk mate of four short years, Joe Keene, who as I type this, less than 24 hours ago witnessed the birth of his first daughter. Dr. Amy Ng, for your hard work and willingness to truly collaborate. Thanks to Dr. James McBride for somehow always managing to put up with the shenanigans of the people that surround him—James, you were a huge help.

Thanks to Dr. Tony Hmelo for being a bottomless well of help throughout the years. Thanks to the entire VINSE staff for all your hard work and upkeep of all the instruments I frequented. Thanks to John Fellenstein and the entire machine shop, your precision is unmatched. To Chanse Hungerford for your expertise in LabVIEW, thank you for making my device testing possible. Thanks to Dhiraj Prasai and the entire Bolotin lab for the most engaging collaboration I was a part of. To all of those who have helped me throughout the last 5 years, I hope you know who you are and I trust you know how grateful I am to you.

To all my wonderful friends I've made in Nashville, I think we can all agree that our mutual presence has truly made this place feel like home. The original poker crew has grown and shrunk, molded and swelled, but the one underlying theme is that it is always full of lifelong friends. Bunch of crazy biologists (and Tim, and Max). And to Josh and Jessica, is it possible to be this neighborly-fortunate? Thank you all so much.

No written words can justify the amount I owe to my family. The emotional, monetary, comic, comforting and loving support you've given me is cherished. To mom and dad, can you believe I'm not able graduate from any more places, what'll I do? I cannot imagine having a better set of parents to look up to. You've taught me to remain

cool, to pursue happiness and above all else how to be a good person. To Kyle and Alex, we are lucky to have friends who also happen to be our brothers, never forget that.

Finally, to my future wife Anita: we met three weeks before I began the process that is ending here and the last five years with you has been the most fulfilling and special of my life. Your support and confidence in me has truly been a driving factor in my success. You are my best friend and I am infinitely grateful to you for simply remaining who you are. Thank you.

TABLE OF CONTENTS

Page

List of Tables

Page

Table

List of Figures

Page

Figure

Chapter I.

INTRODUCTION

1.1 Current State of Nanotechnology

The field of nanotechnology is undergoing a transition from a mostly exploratory science to one of real industrial significance. Materials that were once touted for their possible application to various hypothetical needs are being purchased by companies and incorporated enthusiastically into a wide swath of products. Baseball bats utilize resins embedded with carbon nanotubes, spray-on superhydrophobic coatings are sold in department stores, aerogels are being used for light weight thermal insulation, graphene transistors are being sold to cell phone companies; the list goes on. The exploration of matter at the nanoscale is a self-perpetuating cycle in which the need for better characterization of a known material instigates the development of advanced analytical techniques that, in turn, allow for the discovery more new nanomaterials.

Currently, 2-dimensional semiconductor materials,[1,2] plasmonic materials[3,4] and perovskites[5,6] are garnering considerable attention in the literature, a testament to the ever-changing landscape of nanotechnology research, which was dominated largely by graphene and colloidal metals and semiconductors just half a decade ago. Perovskite solar cells, composed of thin films of crystalline $CH_3NH_3PbX_3$ (X= I, Cl, Br) are an extremely exciting form of photovoltaic that has advanced quickly in efficiency from roughly 4% in 2009[7] to a certified 20.1% in 2014[8] and seem particularly poised for successful industrial application. Still, last year marked the inaugural Gordon Conference on Colloidal Semiconductor Nanocrystals, which was very well attended and full of active research projects pursuing answers to yet-to-be understood phenomena and

innovative applications. The Rosenthal group at Vanderbilt focuses on a wide breadth of topics concerning the study of semiconductor nanocrystals—or quantum dots (QDs)—from spectroscopy of fundamental physical processes[9-11], to cell surface protein tracking[12-14], synthetic studies of improved or novel QD types[15-18] and the integration of QDs into energy saving application such as LEDs and photovoltaics (PVs).[19-23] The remainder of this introduction will pertain to background on work I performed as a member of the Rosenthal group that dealt with the implementation of QDs in PVs.

A

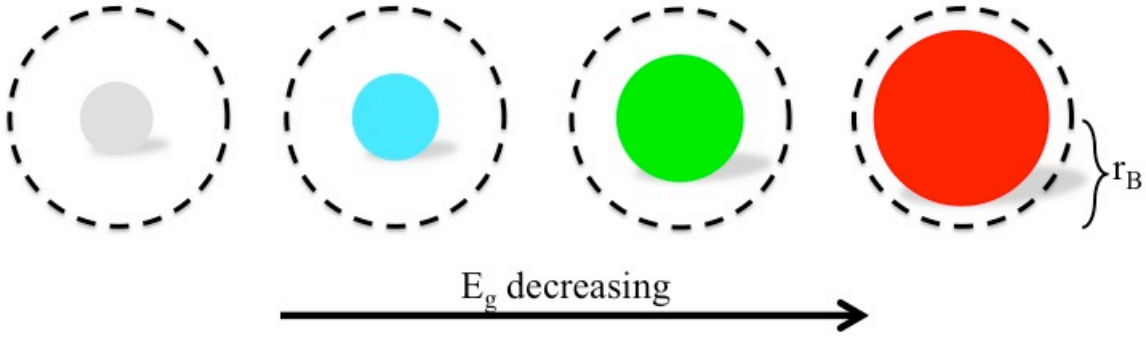

B

Figure 1.1: (A) Animation showing effect of QD size on band gap with dashed circle representing the Bohr radii. (B) Image of CdSe QDs, increasing diameter left to right.

1.2 Quantum Dots and Quantum Confinement

Quantum dots are individual particles of semiconductor material whose radii are smaller than that of the material's Bohr exciton radius—the distance at which an excited electron prefers to orbit its corresponding hole (Figure 1.1). A semiconductor nanocrystal within a dielectric background having such a small size causes confinement of excitons in all three spatial dimensions, an effect known as quantum confinement. The resulting system is one whose energies levels can be described by classic particle in a box theory and deviate from that of the bulk material in that they become discretized. This discretization can be visualized directly as distinct features within absorption spectra and can be understood as representative of a sort of transitory material state between highly distinct atomic-like quantum energy states and the continuous energy bands seen in bulk semiconductors (Figure 1.2). QDs can exist as colloidal suspensions, each dot being coated with a given surfactant molecule which is used to both passivate its surface electronically as well as ensure that the QDs remain crystallographically isolated when in solution to prevent agglomeration.

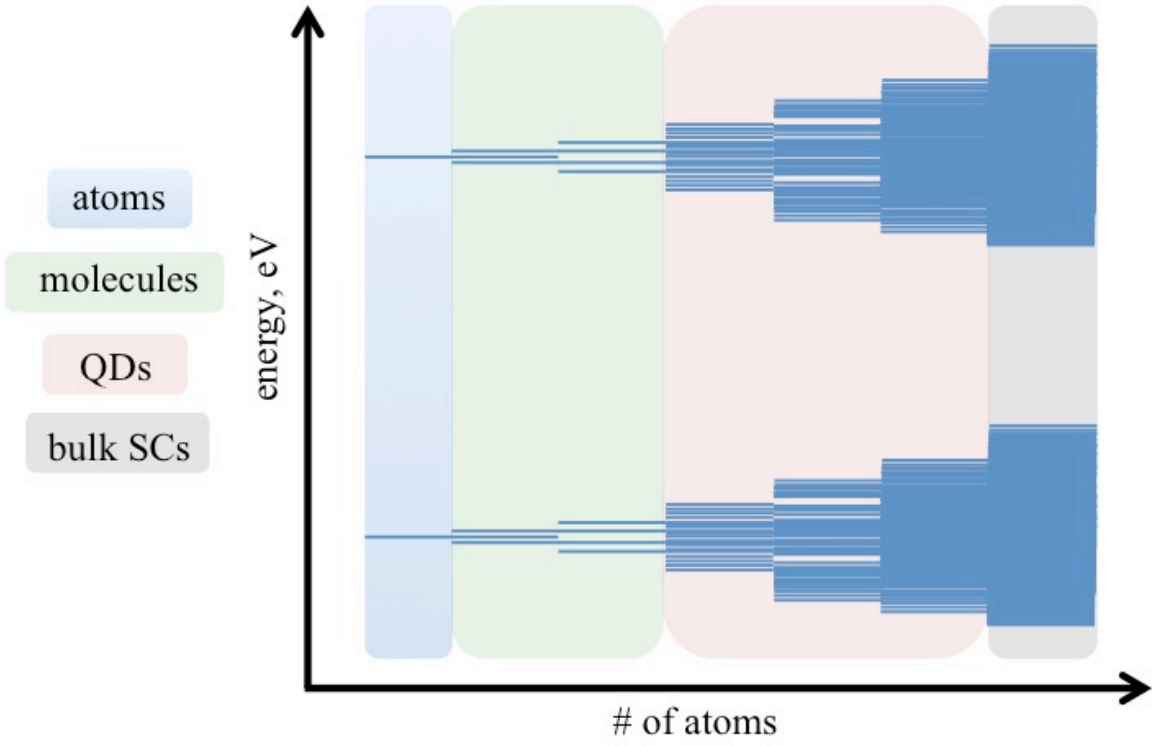

Figure 1.2: Schematic showing the transition from atomic-like states the to formation of band structure as the number of atoms in the system increases. Generally, when the number of atoms is $>10^5$, valence and conduction bands become continuous, mimicking bulk properties. QDs exhibit band properties somewhere between that of single atoms and molecules and bulk semiconductors, which can be visualize in the "pockets" of blue interspersed with low state density regions in the energy landscape. The bands shown in the diagram are meant to be a general representation of the process of energy band formation; in reality, these bands more closely represent the *band edge* density of state landscape because the interior of bands form before the more sparse edges. Since the Fermi level lies within the gap in a semiconductor, the optical and electronic properties of QDs tend to be dominated by this region of pocketed energy states.

Alexey Ekimov observed these quantum confinement effects in the early 1980s[24], however the first reports of QD colloidal synthesis and modeling was performed by Louis Brus in the years following.[25] In Brus' theoretical analysis, he derived an equation (Eq. 1), which is essentially a corrected energy eigenvalue for the added effects of quantum confinement in an excitonic system.

$$E = \frac{h^2}{4R^2}\left[\frac{1}{m_e} + \frac{1}{m_h}\right] - \frac{1.8e^2}{\epsilon_2 R} + \frac{e^2}{R}\overline{\sum \alpha_n \left(\frac{S}{R}\right)^{2n}} \quad (1)$$

E in this equation represents the energy increase with respect to the bulk bang gap value. Notice the three terms in the equation all incorporate the radius of the particle, *R*. The first term in the above equation represents "energy of localization", which is generally the energy increase associated with confining electron hole pairs to dimensions smaller than would naturally occur. The second term represents the Coulombic attraction between the excited charges and is negative, signifying a relaxation effect on the overall system. The third is deemed "solvation energy" and refers to instantaneous energy values associated with electric fields created as charges move through a low volume dielectric medium, which are normally negligible at bulk volumes. As an example, this equation can be used to calculate the total shift of a CdS QD with R = 20 Å ($E_{g,\,bulk}$ = 2.58 eV, m_e^* = 0.19, m_h^* = 0.8, ε = 5.7) to 0.43 eV, which agrees very well with synthetic work that was subsequently published.[26]

The discovery of quantum confinement and the proliferation of quantum dot synthetic procedures ushered in a sea change with respect to what engineers and materials scientists once thought possible with electronic systems. A given material no longer had a static band gap—they were now malleable and a function simply of tweaks in the

synthetic parameters. Charge transfer processes now had the potential to be intimately controlled by precise band alignment engineering. Inorganic semiconductors could now be spun-cast into films, alleviating the need for high vacuum and/or high heat deposition procedures. They also exhibit extremely good absorptive properties, with molar extinction coefficients generally in the range of $\varepsilon = 10^5\text{-}10^6\ M^{-1}\ cm^{-1}$ [27-29], and concentrated oscillator strengths[30], which beckoned application to nonlinear optics, photovoltaics and LEDs.

This excitement was vindicated through thousands of publications in the decades following the inception of QDs. In fact, this year marks the first for widespread industrial application of QDs as emitters in display applications. Major television makers are retooling their product catalog around the incorporation of QDs due to their sharp emission peaks and unmatched color rendering capabilities. Indeed, it seems only a matter of time until QD technologies are commonplace in the industrial sector.

1.3 Photovoltaics

1.3.1 History and Physical Basis

While the first patent for an industrially viable photovoltaic (PV) device was given to Robert Ohl of Bell Labs in 1946, some may be surprised to learn that A. E. Bequerel first observed the PV effect many years prior in 1839 while measuring electrical leads from gold and platinum plates placed in aqueous solution under sunlight. Simply put, PVs materials harness electromotive forces stemming from Galvani, or built-in potentials to pass light-excited electrons through a circuit. The voltage stemming from

the built-in potentials combined with the current stemming from the electromotive force generates a power in watts that is usable so long as the PV is under illumination.

It comes as no surprise that the first modern PV, or solar cell, was born out of Bell Labs in the late 1940s. It was around this time that Bardeen, Brattain and Shockley were developing the first transistor and Bell Labs was truly at the forefront of the silicon-based world in which we find ourselves today. Semiconductor theory was forming rapidly and solid-state physicists such as Shockley were rapidly deducing many of the same formulas engineers still use today to design semiconductor-based technologies. The first commercially available solar cell was released in 1955 and was based upon what would become the ubiquitous silicon p-n junction (Figure 1.3).

At the interface of a p-n junction (x=0 in Figure 1.3B) exists a "space charge region" in which the two materials transfer majority carriers in order to neutralize the strong potential that would otherwise occur between the two layers if they were separated by a dielectric. Throughout this charge exchange process, the Fermi level within the system remains constant while the vacuum, conduction and valence band levels "bend" with the changing electrical potential with respect to the static Fermi level. This region of band bending—the space charge region, or commonly the "depletion region" due to the scarcity of free charges therein—exhibits a changing potential gradient over a distance, which translates to an electric field (eV/m). Electron-hole pairs generated in this depletion region will be effectively pulled in opposite directions through the p-n junction towards their respective electrodes. In the diagram below, excited holes will relax energetically to higher potential towards the left and travel as majority carriers through the p-type layer towards the cathode, and vice versa for excited electrons.

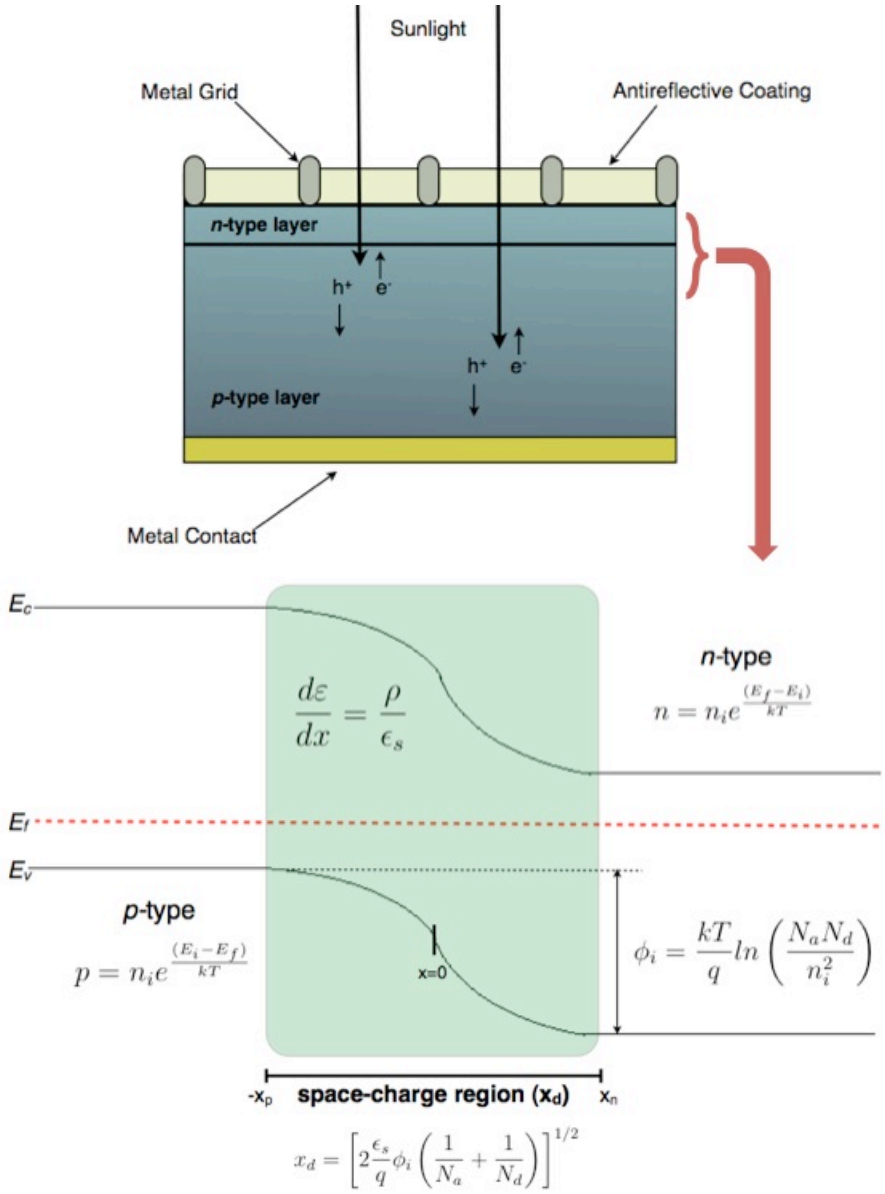

Figure 1.3: Drawing of a typical p-n junction photovoltaic cell, much like the one first commercialized at Bell Labs in 1955, utilizing a relatively heavily doped n-type Si on its anodic side and a moderately doped p-type Si on its cathodic portion. Charges excited under illumination are separated under the influence of the electric field with the depletion region (highlighted in green below) at the p-n junction and accelerated to their corresponding electrodes. The depletion region width (x_d) is a property of the dopant density of the two layers.

1.3.2 Detailed Balance Efficiency Limit

In 1960, years after the commercialization of p-n junction solar cells, William Shockley, along with his coworker Hans Queisser, released an article while working in the newly established Silicon Valley that detailed what has come to be known as the Shockley-Queisser Limit.[31] In their work, they ascribe a *detailed balance limit* to the efficiency of single junction p-n junction solar cells, which pertains to the situation in which recombination and absorption processes are totally optimized. The limit can be summarized in the following term:

$$\eta(x_g, x_c, t_s, f) = t_s u(x_g) v(f, x_c, x_g) m\left(\frac{v x_g}{x_c}\right) \tag{1}$$

in which η is efficiency and is a function the four variables. x_g is the band gap divided by thermal sun energy (E_g/kT_s), x_c is the ratio of the solar cell temperature to that of the sun, t_s is the probability that an incident photon creates an electron hole pair, and f is a geometrical and transmission factor. The elegance of this seminal paper is in its ability to apply relatively simple black body physics and geometrical considerations to the modeling of the photovoltaic effect. For a further explanation, the first term represents the ultimate efficiency of the PV:

$$u(x_g) = hE_g Q_s / P_s \tag{2}$$

where Q_s is the flux of photons greater than E_g per unit area per second, h is Planck's constant, and P_s is the power of the incident solar light. The second term can be simplified as the ratio of the open circuit voltage, V_{OC}, to the maximum possible voltage, which could be attained from the cell, V_g, which is simply the gap voltage and would

occur with no temperature. Shockley and Queisser derive this second term for voltage as a function of the aforementioned geometrical and transmission-based *f* term from Eq. (1):

$$f \equiv f_c f_\omega t_s / 2 t_c \tag{3}$$

in which f_c is the fraction of recombination-generation which is radiative, f_ω is the geometrical factor dependent upon the solid angle subtended by the sun and angle incident upon the cell, t_c is the probability that an incident photon will generate an electron-hole pair, and the factor of ½ derives from the fact that light falls on only 1 of the 2 sides. Lastly, the final variable *m* can be described as the solar cell fill factor (FF), which is simply the ratio of the maximum power generated by the cell under illumination to the nominal incident power:

$$m = I[V_{max}]V_{max} / I_{SC}V_{OC} \tag{4}$$

where $I[V_{max}]V_{max}$ is the maximum power point along the *I-V* curve of the solar cell, and the denominator represents the short circuit current multiplied by the open circuit voltage.

Through all these theoretical considerations, there are two critical conclusions to be drawn. Firstly, based upon the 6000 K black body curve of the sun, the optimal band gap for a single junction p-n solar cell is ~1.3 eV, which is, fortunately enough, within 0.2 eV of the bulk Si bandgap. Second, the maximum thermodynamically limited, detailed balance efficiency for a p-n junction PV device is found to be 30% with a device temperature of 300 K. Exceeding this 30% is an often-cited value that is a sort of "holy grail" for modern solar cell researchers as

nanotechnology blossoms and new ideas, such as those described in the following section, attempt to overcome this thermodynamic limit through innovative approaches.

1.3.3 Generation I, II and III Classifications

The terms generation I, II and III are often used to describe three distinct phases in the development of solar cell research. Generation I photovoltaics are those that were described in section 1.3.1, relying on p-n junction of Si as their active layers. Generally, these solar cells have active layers (Si absorber layers) that are hundreds of microns thick composed of either crystalline or polycrystalline Si (p-Si). These thick active layers are necessary due to the poor absorption properties of Si stemming from its indirect bandgap. In materials with indirect band gaps the electronic transition from the top of the valence band to the bottom of the conduction band requires a change of momentum by coupling the optical transition with a lattice phonon, which greatly reduces the probability that an incident photon will generate an electron-hole pair. Notwithstanding, due to ease of production, relatively low costs, and high Earth abundance of Si, generation I solar cells remain by far the most commonly distributed commercial PV module, accounting for the vast majority of the PV industry.

Generation II solar cells took root mainly in the 1970s and are still an active area of research which is geared towards decreasing the active layer thickness through harnessing materials other than crystalline or p-Si. Theoretically, one should be able to utilize semiconductor materials with direct band gaps, which would require much less material due to their high absorption coefficients. Of note,

$CuIn_{1-x}Ga_xSe_2$ (CIGS), CdTe and $In_{1-x}Ga_xAs$ are all direct band gap materials that have been heavily investigated and to some extent commercialized. CIGS, for instance, is one of the most highly absorbent bulk materials known—requiring ~1 μm for near total absorption—and can be readily placed on mechanically flexible substrates. Recent advances in low temperature deposition processes of CIGS at the Swiss Federal Laboratory EMPA have enabled these flexible PVs to have efficiencies above 20%, which competes with even the most highly efficient crystalline Si devices. It is yet to be seen if these outstanding performers will eventually hold a significant market share of the PV sector, as ousting well established Si technologies has been historically challenging. Lastly, the most widespread generation II PV material commercially speaking is amorphous silicon (a-Si), which is essentially Si glass. a-Si has historically been used in applications which require small amounts of power—most notoriously the small solar cells atop handheld calculators—due to its intrinsically poor performance compared to p-Si. However, a-Si is advantaged by the fact that it can deposited rather easily with plasma enhance chemical vapor deposition (PECVD) over large areas, thereby bypassing the general ingot route necessary with other Si types.

Generation III solar cells, while they have a somewhat convoluted definition, generally pertain to modern innovative photovoltaic architectures that attempt to overcome the Shockley Queisser ~30% efficiency limit. Techniques for this approach include any one or combination of the following: advanced solar concentrators such as photonic or plasmonic arrays[32,33], band gap gradient tandem solar cells aimed at generating current from all wavelengths of sunlight while

retaining sufficient open-circuit voltage (V_{OC}) values[34], organic polymer-based active layers[35-37], dye-sensitization in electrolytic PVs (Grätzel cells)[38,39], and finally the usage of QDs as absorbers[40-42], among others. Initially, quantum dots were touted as ideal absorbers in PVs due to the potential for exploitation of somewhat exotic properties such as multiple carrier generation per photon and a "photon bottleneck" effect that refers to a dramatically slowed thermalization process in QDs.[43-45] However, in hindsight it seems that perhaps QDs are most advantageous due to their ability to be implemented as "solar paints" which would allow for thin films that could be applied easily over large areas in a very cost effective manner. Regardless, QDs remain one of the most promising generation III materials, having reached 9% efficient PVs in roughly 5 years of intense development of their current most successful architecture.[46,47]

This thesis focuses on the usage of QDs as absorbers in general, with a particular focus on PV applications. Emphasis is given to the chemical modification and optimization of the materials used, while holding steadfast to the ideal of integrating physics and electrical engineering knowledge for the development of a well-rounded understanding of the topics at hand.

Chapter II.

SYNTHESIS & CHARACTERIZATION OF Cu_xIn_yS PLASMONIC QUANTUM DOTS

2.1 Introduction

The global need for renewable and cleaner energy alternatives continues to instigate research in high-efficiency and low-cost photovoltaic devices. Owing to factors such as their tunable band gaps, strong absorption and low cost of preparation, semiconductor quantum dots (QDs) have emerged as an important portion of this global research trend.[40,42] In particular, inorganic solid-state QD photovoltaics (QDPVs) formed by simple layer-by-layer deposition processes have garnered significant attention for their promising incident photon conversion efficiencies (IPCEs).[48] Although still a technology in its infancy, Bawendi, et al., have recently reached 9% IPCE, the highest published value for a QDPV.[47] To date, solid-state QDPV devices have focused largely on the utilization of IV-VI (PbS, PbSe) QDs due to their near-infrared (NIR) conduction band-edge values and established synthetic procedures.

Plasmonics have received considerable attention in recent years for their possible implementation to PV devices[33,49], which would theoretically allow for decreased film thicknesses through light trapping by scattering from nanoparticles within the PV device. Furthermore, if absorbance in the localized surface plasmon resonance (LSPR) mode is resonant with electronic transitions, enhancements in overall current output may be seen through their implementation into QDPVs through the near-field electric field absorption enhancement effect.

Significant overall power conversion efficiency improvements have been achieved in dye-sensitized photovoltaics[50] and photocatalytic systems[51] through the incorporation of SiO_2-coated Au nanoparticles. In each case, the effects of Au plasmonic absorbance is resonantly transferred to either a dye molecule or a peripheral QD; a process in which dye-particle spacing is of great importance. One can foresee the possible benefits of a material in which both the semiconducting and plasmonic electronic modes are centered upon the same particle. Namely, near-field coupling of the plasmonic resonance to electronic excited states would be an optimally intimate process, as opposed to a process which requires these transitions to occur over some distance. This potential was indeed mentioned in a previous report by Luther, et al.: "The LSPR mode, if resonant with excitonic transitions, can enhance (1) the absorption cross-section of the excitonic transition by means of an antenna effect […]".[52] The emergence of LSPRs in semiconducting QDs presents an exciting candidate for realizing this optimized system.

Ternary I-III-VI materials ($CuInS_2$, $CuInSe_2$, $AgInS_2$) constitute a class of compounds advantaged by low toxicity as well as comparable electronic characteristics to the IV-VI semiconductors.[53-55] In particular, $CuInS_2$ (CIS) possesses a bulk direct band gap of 1.45 eV, close to the energy corresponding to the peak black body emission of the sun (~2.2 eV).[56] Considerable strides in the synthesis of CIS QDs have been made in recent years,[57-59] however synthetic routes generally result in QDs with radii larger than that of the Bohr exciton radius of CIS.[60-63] The Bohr radius can be estimated by the relation $r_B = (\varepsilon_{dot}/\mu)a_0$, where $\mu = 1/(m_e^{*-1} + m_h^{*-1})$, a_0 is the hydrogen Bohr radius, and ε_{dot} is the dielectric constant of the bulk material.[64] The constants m_e^{*-1} and m_h^{*-1} are the reduced mass of the electron and hole, respectively, and have been shown to be $m_e^{*-1} \approx$

0.16 m_e and $m_h^{*-1} \approx 1.3\ m_e$ for CIS.[65] This yields a exciton diameter of 8.2 nm for CIS, purporting that significant quantum confinement, and therefore significant band gap engineering due to size control, cannot occur above diameters of ca. 8 nm.

2.2 Experimental

2.2.1 Synthetic Parameters

In a typical synthesis of monodisperse and electronically tunable chalcopyrite copper indium sulfide ($Cu_xIn_yS_2$) semiconductor quantum dots (QDs) with LSPRs that are tunable over a range of near infrared (NIR) frequencies, 1 mmol of copper (II) acetylacetonate ($Cu(acac)_2$), 1 mmol of indium (III) acetylacetonate ($In(acac)_3$), 1 mmol dodecylphosphonic acid (DDPA), 2.5 g trioctylphosphine oxide (TOPO), and 2.5 g hexadecylamine (HDA) are heated to 140 °C, dried and degassed under vacuum for 10 minutes and subsequently purged with argon and cooled to 120 °C with compressed air. The cation precursor solution at this point is a deep, transparent teal. Meanwhile, 0.75 mmol *bis*(trimethylsilyl) sulfide (TMS_2S) is dissolved into 12 mL of previously degassed octadecene (ODE) at 90 °C. Please see section *4.2.1* for detailed TMS_2S handling and storage procedures for the PbS QD synthesis which can be applied directly to the synthesis outlined in this section. The TMS_2S/ODE solution is swiftly injected into the cationic solution and the QDs are left to grow for 3 minutes, at which point they are externally cooled to 40 °C with compressed air. Immediately upon injection of the TMS_2S, the reaction solution darkens to a deep brown, indicating rapid and widespread nucleation. The QDs are precipitated with acetone, then redissolved in octanol and centrifuged. The supernatent is then precipitated with acetone and the dried QDs are

dispersed in nonpolar solvent. Copper (II) acetylacetonate ($Cu(acac)_2$) (trace metal grade), indium (III) acetylacetonate ($In(acac)_3$) (trace metal grade), bis(trimethylsilyl)sulfide (TMS_2S) (synthesis grade), trioctylphosphine oxide (TOPO) (90%), hexadecylamine (HDA) (90%), octadecene (ODE) (90%) were obtained from Sigma-Aldrich.

2.2.2 UV-VIS-IR; TEM; XRD; RBS Characterization

High-resolution transmission electron microscopy (TEM) images were taken on a Philips CM20 200 kV TEM. Samples were prepared by placing a drop of purified nanocrystals diluted in hexanes to an optical density of <0.1 onto an ultrathin carbon-on-Formvar TEM grid (Ted Pella, Inc.), and wicking away any excess solvent. UV−vis−NIR absorption spectra were obtained on a Varian Cary 5000 UV−vis−NIR spectrophotometer for constant scans from 400 to 3000 nm. X- ray diffraction (XRD) scans were obtained using a Scintag X1 θ/2θ automated powder X-ray diffractometer with a Cu target (λ 1.54056 Å), a Peltier-cooled solid-state detector, and a zero-background, Si(510) sample support.

Rutherford backscattering spectrometry (RBS) was performed using a custom-built setup.[66] Samples were prepared by coating the surface of a pyrolytic graphite substrate (Carbone) with purified nanocrystals diluted in hexanes to an optical density of 0.4−0.6, wicking to remove excess solvent. Experiments were performed in a high vacuum chamber (<10−6 Torr) with a 1.8 MeV ^{4}He ion beam at normal incidence. Backscattered ions were collected at an angle of 176° with a solid-state detector. Spectra were analyzed according to Feldman and Mayer,[67] yielding the elemental composition of

the nanocrystals. Unfortunately, this RBS system was permanently disassembled in 2013. A separate and newer Pelletron RBS system was installed in the Free Electron Laser lab on Vanderbilt's Campus that same year, however studies performed on CIS quantum dots on this newer system did not yield satisfactory data. It was determined that both signal collection rate was too low and that the resultant stoichiometry values were too wildly opposed to findings on both the older RBS and new ChemiSTEM EDS system to render the findings trustable or publishable.

2.3 Discussion of $Cu_xIn_yS_2$ System

2.3.1 Size and Band Gap Tuning

Figure 2.1a shows the absorption spectra for samples composed of various sizes of QDs. For simplicity's sake, the band gap of each of the four represented samples was assumed to correspond to the onset of absorption determined from the x-axis intercept of their corresponding Tauc plots, and each batch will heretofore be represented by its respective value. The absorption onset was tuned from 2.1 (620 nm) to 1.5 eV (800 nm), after which point the band gap ceases to vary significantly with changes in diameter.

The transmission electron microscopy (TEM) images in Figure 1(c,d) indicate spherical QDs with narrow size distribution, which is corroborated with size dispersion analysis shown in Figure 2.3. The uniform crystal lattice fringes suggests that the particles are single crystalline, while X-ray diffraction (XRD) patterns show the crystal structure to correlate with chalcopyrite CIS (Figure 2.1b). The chalcopyrite crystal structure is a ternary analog of the typical cubic zincblende in which the c-direction is lengthened by a certain amount due to stretching of the lattice stemming from the

differing cation identities. Generally, a chalcopyrite unit cell consists of a rectangular prism of two zincblende-like primitive cells stacked along the c-axis.

Several reaction parameters must be altered in order to preserve the stability and spherical shape while achieving a desired diameter. Specifically, while the smaller particles require large amounts of TOPO for stabilization, spherical seeds exhibit preferential growth along the <001> directions with addition of higher concentrations of TMS_2S. This effect amounts to the creation of rods in the presence of equimolar amounts of TOPO/HDA with increases in sulfur (Figure 2.2). Rod growth is suspended by the reduction of the TOPO to HDA ratio, promoting stable spherical particle formation at larger sizes.

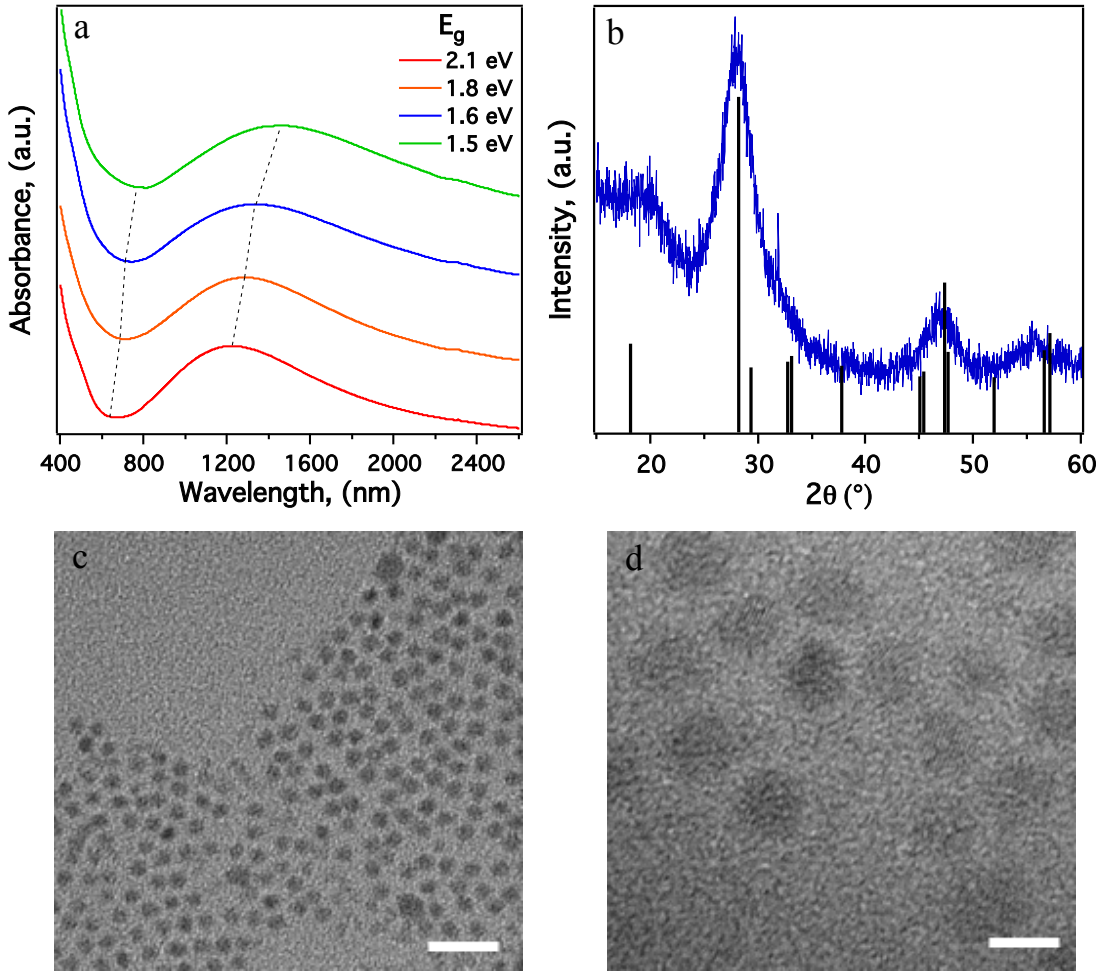

Figure 2.1: (a) Absorption spectra from 400-2600 nm for samples of varying band gap; 2.1 eV band gap (red), 1.8 eV band gap (blue), 1.6 eV band gap (orange), 1.5 eV band gap (green). Dashed lines show trends in changes in band gap and LSPR peak values. (b) XRD spectrum of 1.5 eV band gap QDs compared to standard for chalcopyrite $CuInS_2$ (JCPDS #27-0159). TEM images (c,d) showing dispersity of 4.0 nm CIS dots, scale bars represent 20 and 5 nm, respectively.

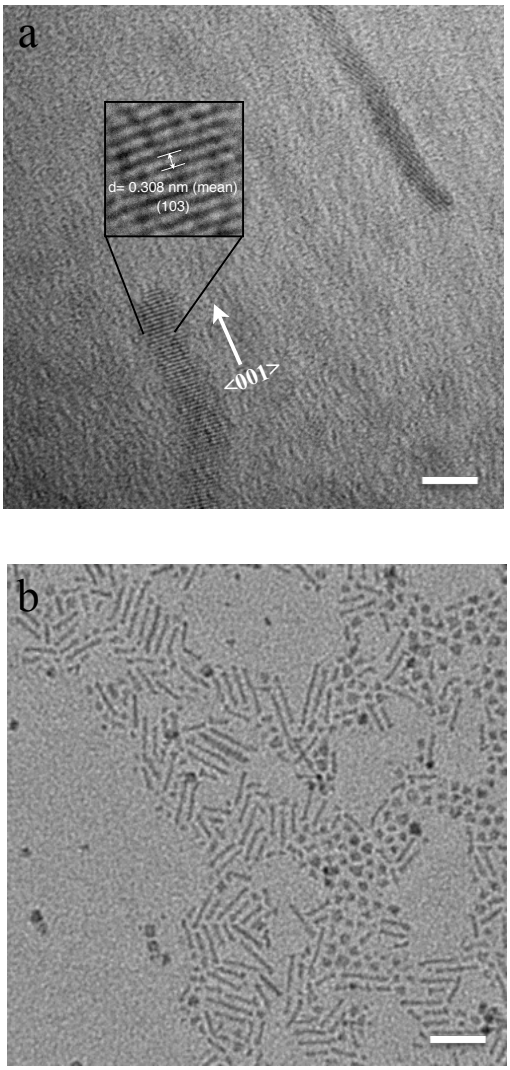

Figure 2.2: HR-TEM images showing rod growth at unity TOPO:HDA ratios for attempted large particle synthesis. Rod growth was suspended by decreasing TOPO:HDA. (a) Image showing growth occurs along <001> directions, inset shows fringe measurement representing (103) face (scale bar represents 5 nm). (b) Image of large collection of rods (scale bar represents 20 nm).

Increases in diameter are achieved by a two-fold process involving augmentations in both sulfur precursor and DDPA amounts. Decomposition and reaction of TMS_2S occurs at a very high rate, causing particle formation to be rate-limited by the reactivity of the cationic precursor. Therefore, altering the reactivity of the Cu(II) and In(III) precursors through addition of higher equivalents of DDPA allows for the formation of larger QDs through stoichiometric changes in sulfur precursor. Due to the aforementioned high reactivity of TMS_2S, temperature has a less controllable effect on the final size of QDs, in comparison to previously published work.[10,12] Table 2.1 lists specific reaction parameters for the formation of QDs with gradual changes in band gap.

Table 2.1: Reaction parameters for synthesis of $Cu_xIn_yS_2$ QDs with varying diameters

TMS_2S (mmol)	DDPA (mmol)	TOPO: HDA[a]	diameter (nm)	band gap (eV)[b]
0.75	1	1:1	4.0 ± 0.5	2.1
1.25	1.5	3:7	4.4 ± 0.5	1.8
1.5	2	1:4	4.9 ± 0.4	1.6
2	2.5	0:1	5.6 ± 0.5	1.5

[a]Based on a 5.0 g total mixture. [b]Calculated from the wavelength corresponding to onset of absorption determined from Tauc plot x-axis intercepts.

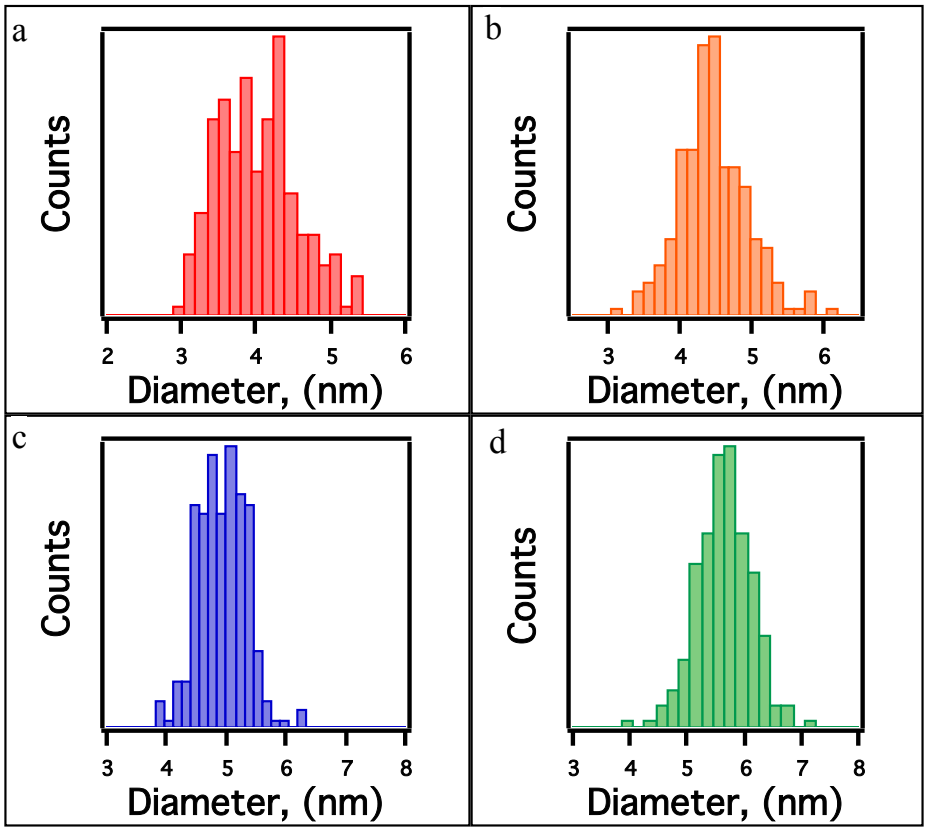

Figure 2.3: (a-d) Histograms showing size distribution for 200-QD sample measurements; (a) 2.1 eV band gap- 4.0±0.5 nm (red), (b) 1.8 eV band gap- 4.4±0.5 nm (orange), (c) 1.6 eV band gap- 4.9±0.4 nm (blue), (d) 1.5 eV band gap- 5.6±0.5 nm (green).

2.3.2 LSPR Characterization, Drude Theory

Notably, the QDs exhibit size dependent broad absorbance in the near infrared (IR). To the best of our knowledge, there have been no previous reports of this sub-band gap absorbance in any of the typical IV-VI, II-VI or I-III-VI QD species. Sub-band gap absorbance can arise from several factors such as scattering, inner-conduction band absorption[68], and sample impurities. However, we can conclude that this absorbance is a

result of LSPRs due to a shift in absorbance maxima with changes in indices of refraction (*n)* of solvent species (Figure 2.4).[52] Additionally, one could assert that solvatochromism is responsible for this sensitivity to *n*, but this possibility is refuted by two factors. (1) The π^* scale of solvent polarity values used in solvatochromic effect studies are relatively low for the solvents used in this study (compared to a dimethylsulfoxide standard value of 1.000): carbon tetrachloride, 0.294; tetrachloroethylene, 0.277; carbon disulfide, 0.514.[69] (2) The shifts in the proposed LSPR peak wavelengths are on the order of 14-23 nm, compared to typical solvatochromic shifts in QDs that are on the order of less than 1 nm.[70]

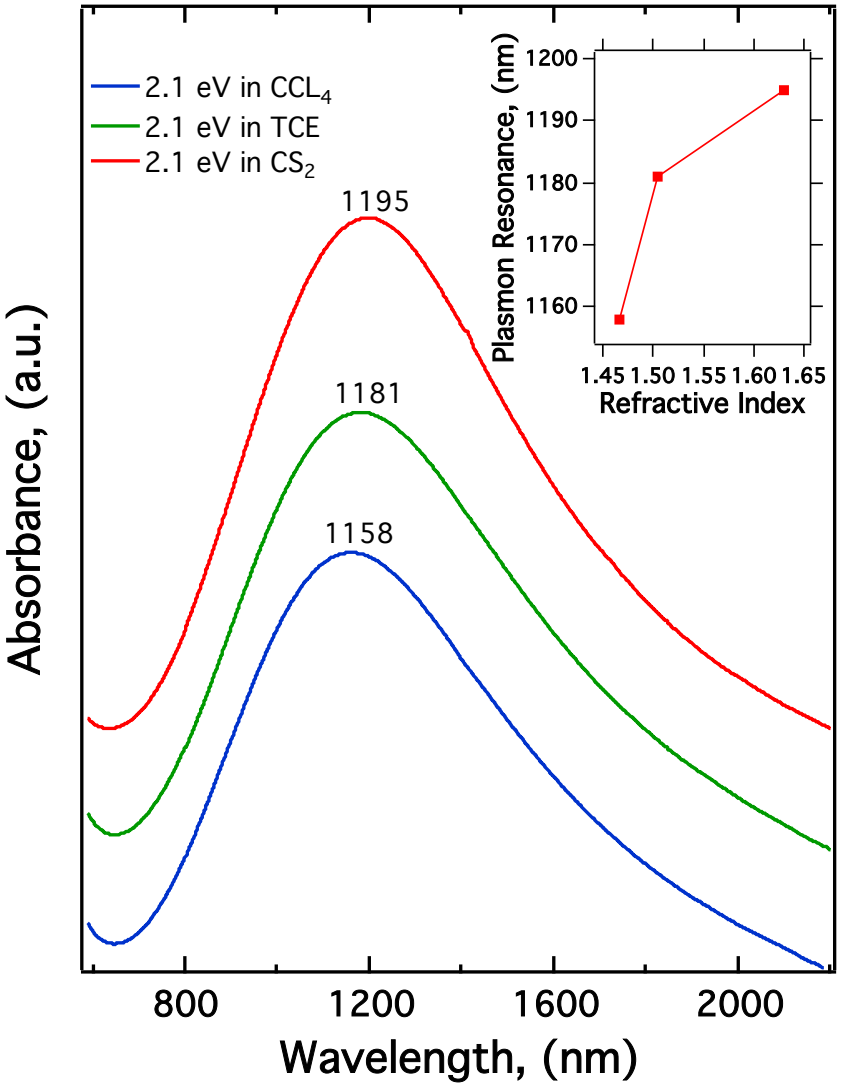

Figure 2.4: Absorption spectra in differing solvents for 2.1 eV band gap sample; carbon tetrachloride (blue), tetrachloroethylene (green); carbon disulfide (red). Inset graph shows the dependence of LSPR maximum on index of refraction of solvent (250 nm/RIU).

These QDs exhibit a plasmonic sensitivity of ~250 nm per refractive index unit (nm/RIU), which is comparable to those in previous reports of $WO_{2.83}$ nanorods (280 nm/RIU)[71], $Cu_{2-x}S$ QDs (350 nm/RIU)[25], silver nanoprisms (200 nm/RIU)[72], or gold nanoshells (130 to 360 nm/RIU).[73] Notably, this sensitivity is not linear, as seen on the inset of Figure 2, generally because of refractive effects caused by the ligand shell. This allows the LSPR absorbance maxima to be efficiently tuned not only by the size of the QDs, but also by altering the index of refraction of the surrounding medium.

Elemental analysis was performed by way of Rutherford backscattering spectroscopy (RBS), which provides a highly sensitive method for determining accurate elemental composition ratios (Figure 2.5).[74] Due to the small QD size in our samples, peak-broadening severely limits the applicability of XRD for elemental analysis purposes. Likewise, inherent errors associated with inductively coupled plasma mass spectrometry (ICP-MS), such as the difficulty in gaining sulfur concentration, restrict its viability in this report. The RBS results (Figure 2.5) show cation deficiencies, which is an unexpected result due to the sulfur deficient precursor stoichiometries. Specifically, the 2.1 eV and 1.6 eV band gap samples were found to have stoichiometries of $Cu_{0.88}In_{0.95}S_2$ and $Cu_{1.01}In_{0.91}S_2$, respectively.

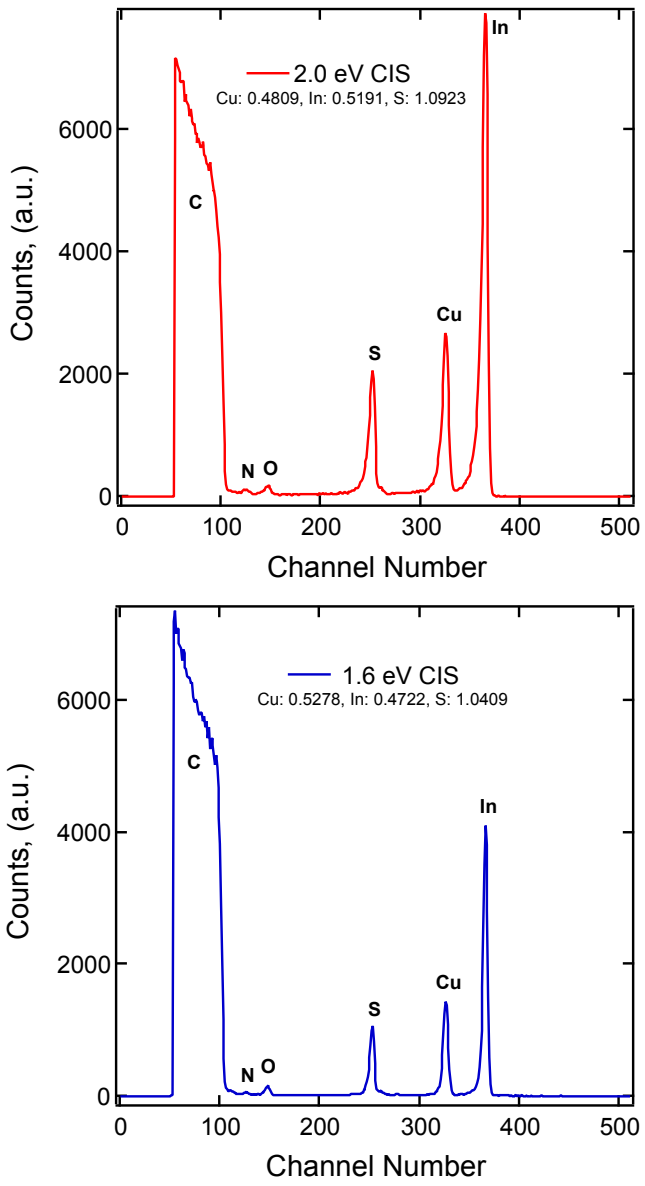

Figure 2.5: Rutherford backscattering spectra of E_g= 2.0 and 1.6 eV samples. Channel numbers correspond to specific scattering angles of incident $^4He^{2+}$ nuclei based upon the atomic nucleus from which it was scattered (higher channel numbers denote higher atomic masses). Curve areas can be calculated and used to determine overall stoichiometries based on a Bi standard, the specifics of which are outlined in the report by Feldman and Mayer mentioned above.

Reports have cited cation stoichiometric deficiencies, which effectively give rise to heavily p-type materials, as the source of LSPRs in chalcogenide QDs.[6,25] These cation vacancies effectively as acceptor points within the crystalline lattice, opening states within the valence band and deepening the Fermi level to lower energies. Dopant density values reported in these studies are obtained through solving equations which relate dopant density to LSPR frequency in bulk, rather than actual experimental data such as Mott-Shottky analysis for QDs. Specifically, the Drude approximation is used to extrapolate dopant density values through their relation to *calculated* bulk plasma frequency estimates. As performed by Alivisatos and coworkers[25], Drude theory for bulk materials is used to estimate doping densities in quantum dots through experimentally measured values. The plasma frequency (ω_p) of the free carriers in the dots is related to the LSPR energy (ω_{sp}) by the following:

$$\omega_{sp} = \sqrt{\frac{\omega_p^2}{1+2\varepsilon_m} - \gamma^2}$$

ε_m is the dielectric constant of the surrounding medium. We have omitted the ligand shell effects for this value and taken the external matrix as solely TCE ($\varepsilon_m = 2.28$). The value γ represents the full-width half max. For the 2.1 eV sample in TCE, with LSPR maximum at 1.05 eV and FWHM of 0.9 eV, $\omega_p \approx 3.3$ eV. Dopant density depends on plasma frequency as:

$$\omega_p = \sqrt{\frac{N_h e^2}{\varepsilon_0 m_h}}$$

where m_h is the hole effective mass, estimated as $1.3m_0$, where m_0 is the electron mass.[21] From these calculations, we estimate N_h to be 2.6 x 10^{20} cm^{-3}, which is within an order of

magnitude of the only other studies of which we are aware that predicts N_h QDs in this manner.[25,28] If these ~4.0 nm wide dots are taken to be spheres with volumes of ~34 nm^3 (3.4×10^{-20} cm^{-3}), this data suggests that there would exist ~nine holes per dot. This extremely low amount of calculated free carriers per dot leads us to speculate there are limitations to the applicability of these equations to QDs of this size regime. We feel that experimental dopant density values are needed for a true understanding of the QD system due to the frequent behavioral discrepancies present between bulk materials and their quantum-confined counterparts.

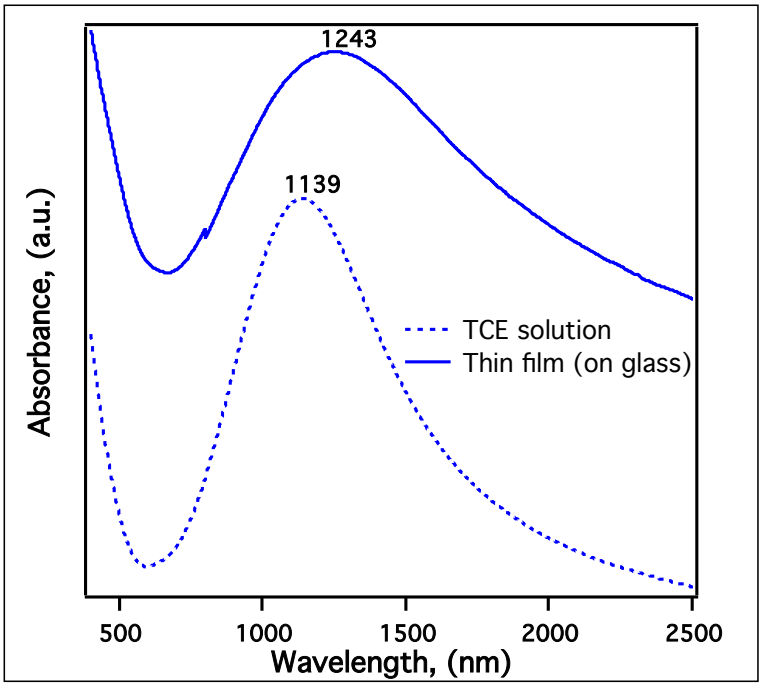

Figure 2.6: Absorption spectra of single sample in TCE (dashed line) and as a spun-cast thin film on glass (solid line). The absorption onset value remains constant while the LSPR peak shifts by ~100 nm.

The insensitivity of the LSPR absorption and value to air exposure may render these QDs favorable for solid-state QDPV applications. Figure 2.6 shows the absorbance spectrum of a sample of 1.8 eV (~4.5 nm) CIS QDs in TCE and as a spun-cast thin film. The LSPR peak in the thin film is slightly broadened with respect to the solution, and its maximum is shifted by ~100 nm. This shift is in reasonable agreement with our sensitivity of 250 nm/RIU (*n* for TCE and air are 1.51 and 1.00, respectively).

Chapter III.

THE EFFECT OF LSPR-ON-EXCITON ABSORPTION IN SIMPLE QUANTUM DOT PHOTOVOLTAICS

3.1 Introduction

The photovoltaic (PV) industry is involved in a constant struggle with the fossil fuels sector to produce price competitive energy on the cost per watt scale. This effort has spurred interest in new-generation solar cell motifs that attempt to realize these goals. In particular, one preeminent tactic for achieving lower overall cost per watt has been simply reducing active layer film thicknesses, however this approach must be realized while not sacrificing necessary light absorption. In thin film silicon technologies, active layers as thick as hundreds of micrometers are commonplace due to the relatively low absorptivity of crystalline and amorphous silicon. Limitations such as these have spurred interest in alternative light absorbing media such as quantum dots, which exhibit decidedly higher molar absorptivities and allow for film thicknesses of less than 1 μm,[48] as well as the implementation of plasmonic metallic nanopatterning and nanoparticles for increased light trapping and absorption cross-sections.[75]

Localized surface plasmon resonances (LSPRs) are electromagnetic excitations of free carriers at the interface of a dielectric and a nanoparticle. These excitations result primarily in a highly localized near-field electric field enhancement around the nanoparticle at resonant energies, which subsequently decays to either far-field scattering of the incident photon or phonon-coupled thermalization into the dielectric background. The realization of "plasmonic solar cells" has long been a challenging goal of PV researchers,[76] however recent advances in nanomaterial synthetic control and

characterization have led to sweeping advances and a proliferation of new ideas. To wit, increases in overall light absorption and short-circuit current (J_{SC}) resulting from plasmonic effects have led to marked efficiency enhancement in dye-sensitized solar cells (DSSCs),[39,50,77,78] as well as organic and inorganic thin film devices.[32,35,79-84] These enhancements generally rely upon either far-field subwavelenth scattering to concentrate incident photons in an absorber layer, or "antenna" effects in which the plasmonic near-field excitation serves to increase the absorption cross-section at resonant wavelengths. Through these effects, LSPR-functionalization may also mitigate the negative impacts of photonic surface texturing—another popular method for augmenting light absorption—such as increases in surface recombination and overall volume of depletion region, as well as the challenges associated with texturing very thin films.[85]

In the past several years, a limited number of publications have detailed the characterization and the mechanistic interpretation of semiconductor nanoparticles that possess LSPR modes.[49,52,71,86-88] These new systems are of wide-ranging interest due to their possible applicability in the fields of non-linear optics,[89,90] LSPR-enhanced light-emitting diodes,[91] and single, quantized plasmon generation,[92] among others.[33] The plasmon bands in typical $Cu_{2-x}(S/Se)$ semiconductor nanocrystals (NCs), such as those reported by Zhao, et al.,[49] and Luther, et al.,[52] are understood to originate from the heavy p-type dopant densities due to the oxidative leaching of copper atoms out of the NC lattice. These acceptor-like copper vacancies generally increase over time as the redox process proceeds toward equilibrium, resulting in gradually denser hole populations and thus, according to the Drude model, an increase in the bulk plasma- and LSPR frequency and intensity. The resultant LSPR modes of these copper deficiencies serve as an

interesting foundation for a new system in which plasmonic and excitonic absorption are centered upon the same particle; an architecture that does not rely on antenna effects to span a physical distance. However, the experimental observation of their possible benefits has remained a challenge because of the inevitable oxidation of Cu_{2-x}(S/Se) NCs upon exposure to air. Furthermore, perhaps the most commonly utilized ligand species for $Cu_{2-x}S$ NCs in particular is 1-dodecanethiol, which suppresses possible surface chemistry modifications by virtue of its high binding affinity and limits their applicability to thin film architectures that require distance-dependent dot-to-dot charge transfer.[93]

The synthesis and characterization of ternary $Cu_xIn_yS_2$ quantum dots with band gaps tunable from 1.5-2.1 eV and LSPR modes in the NIR was described in the previous section and outlined in a published report, as outlined in Chapter 2.[15] This study presented, for the first time, LSPR-expressing, quantum-confined Cu-In-S (CIS) particles suitable for PV and photocatalytic (PC) applications due to both their modifiable surface chemistries as well as LSPR peak stability from the time of reaction through storage in air for several weeks. I-III-VI_2-type semiconductors are suitable candidates for PV and PC applications because of their NIR bulk band gaps, high absorption coefficients and reduced toxicity compared to compounds such as the ubiquitous cadmium and lead chalcogenides. As such, several attempts have been made in the last several years to amend CIS quantum dots as light absorbers in both PV and PC devices[60,94-101], with recorded incident photon conversion efficiencies (IPCEs) for PVs as high as 4.20% reported by Li, et. al.[102]

Normally, CIS NC preparation methods result in particles with charge neutral stoichiometries resembling those of the precursors, and consistently lacking plasmon

modes.[55,60,62,63,87,103] In those studies, stable polymorphs which deviate from the "standard" $Cu_{1.0}In_{1.0}S_{2.0}$ elemental composition are formed when excesses of cationic positive charge present in the precursor stoichiometries and final crystal structure are balanced by incorporation of excess S^{2-} anions. In all of these polymorphs, a net neutral charge is achieved through stoichiometries such as $Cu_{2.0}In_{1.0}S_{2.5}$ and $Cu_{1.0}In_{2.0}S_{3.5}$ owing to oxidation states of (I) and (III) for copper and indium, respectively. In our previous report concerning plasmonic CIS (plasmonic-CIS), Rutherford backscattering spectroscopy (RBS) data showed that the QDs represented therein formed as cation deficient particles whose crystal structures lack charge neutrality. It has been known for decades that Cu and In vacancies (V_{Cu} and V_{In}) in I-III-VI semiconductors act as intrinsic acceptors,[104,105] thereby suggesting that our plasmonic-CIS samples exist as heavily p-doped semiconductors. The Drude model was used to extrapolate a corresponding dopant density of $N_h = 2.6 \times 10^{20}$ cm^{-2}, which was on par with similar LSPR-expressing semiconductor studies.[52,71] Importantly, it was clear through the experimental procedure and subsequent characterization that these QDs were synthetically produced with inherent plasmonic modes, differing from those of copper chalcogenide species in that they are not formed as the result of gradual oxidation. The RBS data suggested that the plasmonic-CIS reaction, rather than forming intermediate crystalline phases such as those in $Cu_{2-x}S$ ($x = 1, 0.2, 0.03$), seemed to form randomly cation deficient samples ($Cu_xIn_yS_2$; $x, y \geq 0.85$). The uniqueness of this reaction—that the inherent mechanism of crystal formation seems to result in massive amounts of cation deficiencies—led us to speculate on whether it could be used as model system for discretely examining the effects of these plasmonic-enhanced excitonic particles.

3.2 Synthesis and Verification of non-Plasmonic "Twin"

3.2.1 Synthetic Parameters

For the observation of the influence of these plasmonic modes on a model system to be experimentally sound, it is compulsory to attain a non-plasmonic-CIS system, differing only in elemental stoichiometries (and therefore presence of LSPR modes). In other words, CIS QDs of the same size, surface chemistry and band gap must be synthesized that are stably non-plasmonic in order to offer an effective experimental control. We developed a synthetic method based on a heavily modified procedure reported by Pan, et al.,[57] which successfully meets all these criteria.

Copper (II) acetylacetonate [$Cu(acac)_2$] (trace metal grade), indium (III) acetylacetonate [$In(acac)_3$] (trace metal grade), indium (III) chloride ($InCl_3$) (98%), copper (II) chloride ($CuCl_2$) (trace metal grade), sodium diethyldithiocarbamate [Na(DEDC)] (reagent grade), bis(trimethylsilyl)sulfide (TMS_2S) (synthesis grade), phenylphosphonic acid (PPA) (99%), hexadecylamine (HDA) (90%), and octadecene (ODE) (90%), were obtained from Sigma-Aldrich.

For the synthesis, diethyldithiocarbamate (DEDC) salts of the cation precursors were used as both cation and S^{2-} sources. The preparation of these precursors involves a simple ion exchange reaction to form insoluble DEDC salts: 50 mL distilled H_2O is combined with with 0.505 g $InCl_3$ (~2.5 mmol) and 0.380 g $CuCl_2$ (~2.5 mmol) in separate beakers. These solutions were added slowly to separate beakers containing 1.126 g Na(DEDC) (~6.5 mmol) in 100 mL H_2O at 60 °C and allowed to stir for 5 minutes. The white $In^{3+}(DEDC)_2Cl$ and dark brown $Cu^{2+}(DEDC)_2$ precipitates were filtered over frit and washed 3 times thoroughly with H_2O. The DEDC salts were dried in a 100 °C oven

in air overnight, and stored in a desiccator. It is important to note the substoichiometric amount of $InCl_3$ salt used to form the In(DEDC) salt. It was found that using a 1:3 molar ration of indium to DEDC salt (for full complexation of In^{3+}) renders the In^{3+} ion essentially unreactive likely due to excessive steric hindrance from the presence of 3 bulky $DEDC^-$ ligands.

For the synthesis on non-plasmonc CIS, 0.280 g In(DEDC) and 0.180 g Cu(DEDC) were added to 10 mL ODE in a 50 mL 3-neck round bottom flask and heated to 120 °C with magnetic stirring under vacuum, and subsequently to 200 °C under Ar. The flask remained at 200 °C until all cationic salts were fully dissolved, at which point the temperature was reduced to 100 °C. Generally speaking, the indium salt takes longer to dissolve than the Cu counterpart, and the complete dissolution can be identified by stopping the stirring and looking at the bottom of the reaction flask for any remaining bits of white In(DEDC) salt in the dark brown precursor solution. In a separate vial, a 2 M solution of HDA in ODE was prepared and heated to 90 °C with magnetic stirring. It is important to keep this vial up to temperature because it rapidly solidifies in syringe needles when cooled, making injection impossible. 12 mL of the 2 M HDA:ODE solution at 90 °C was injected in the cation flask at 100 °C and let react for 10 minutes, then cooled to 40 °C with compressed air. QDs were separated equally into 4 vials and precipitated with acetone under centrifugation at 6500 rpm for 5 minutes. After decanting supernatant acetone, the QDs were dispersed in 6 mL each of toluene and centrifuged at 6500 rpm for 10 minutes. The supernate is reserved and the quantum dots therein were precipitated with acetonitrile under centrifugation at 6500 rpm for 10 minutes. The QD pellets were dissolved in appropriate nonpolar solvent for storage or use.

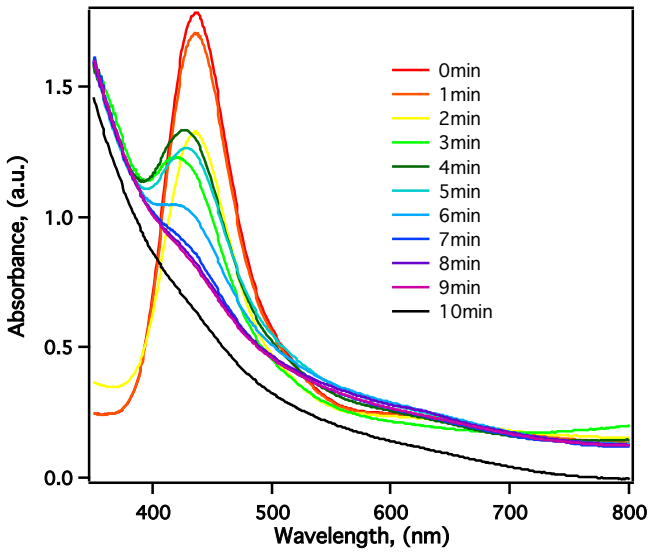

Figure 3.1: Absorption spectra in 1-minute interval samples of a single non-plasmonic CIS reaction showing gradual decomposition of DEDC precursors into crystalline CIS. The large singular peak at ~460 nm and broad peak at ~610 nm in the 0- and 1-minute samples corresponds to the absorption of the precursor only, which are seen to gradually disappear during the course of the 10-minute reaction. Significant QD seed formation is taken to occur at some time between 2 and 3 minutes due to the onset of continuous absorption.

3.2.2 UV-VIS-IR; ^{1}H, ^{15}N, ^{31}P NMR; STEM-EDS Mapping

The reaction results in stable non-plasmonic-CIS particles, which for the purposes of this report have been tuned to ca. 5 nm in diameter and exhibit an absorption onset at 750 nm (Figure 3.2), rendering them highly geometrically and excitonically similar to plasmonic-CIS. Furthermore, the non-plasmonic-CIS lacks any detectable plasmonic absorbance in the IR, and do not readily undergo oxidative processes which would render them plasmonically active in these experiments (Figure 3.3).

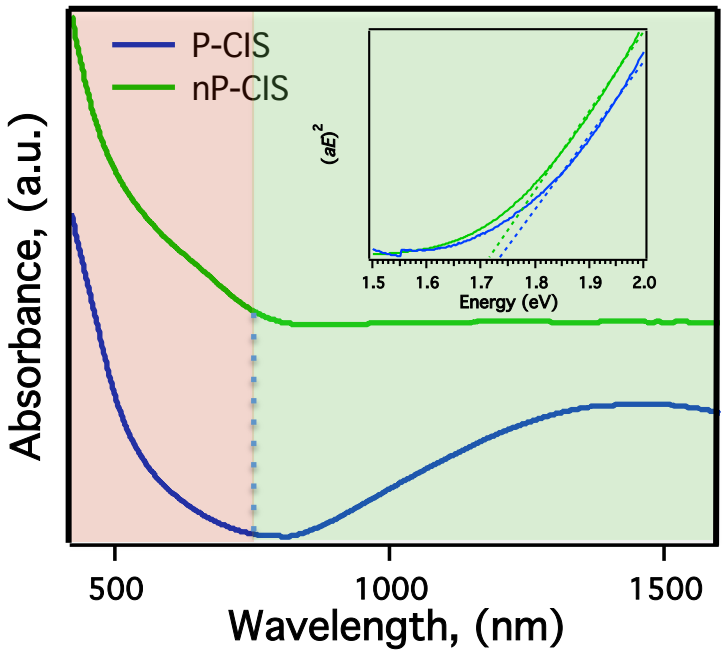

Figure 3.2: Absorbance spectra of plasmonic (blue) and non-plasmonic CIS samples. Spectra are separated on the y-axis to better compare excitonic (light red) and plasmonic (light green) absorbance sections. Both spectra are taken on samples suspended in tetrachloroethylene. A Tauc plot is shown in the inset, exhibiting the optical band gap similarity to within ±0.1 eV between the two samples.

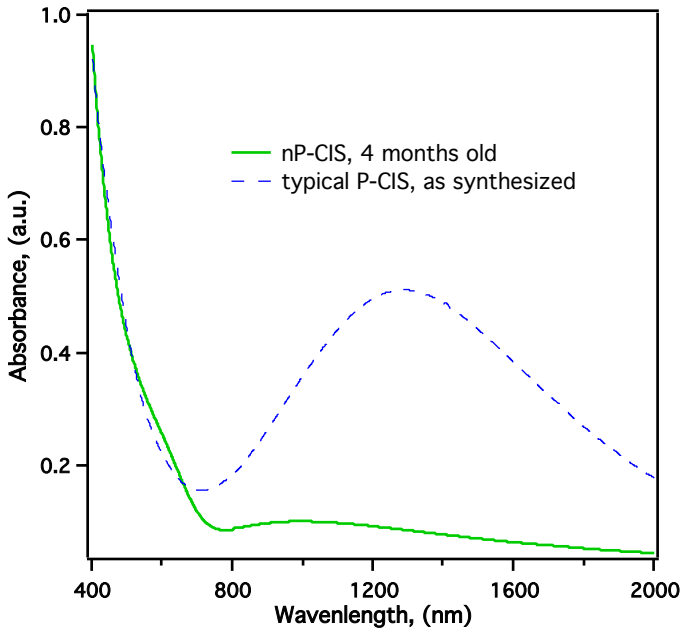

Figure 3.3: Absorption spectrum of a 4-month-old sample of non-plasmonic CIS stored in ambient air. An extremely broad and weak feature, centered at roughly 1000 nm, was found to appear at roughly 3 months, with no noticeable change in absorption at earlier dates. A typical as-synthesized plasmonic-CIS spectrum is shown for comparison of intensities of these peaks. This data is presented to showcase the assertion that, on the time scales over which our experiments are performed, the non-plasmonic CIS particles do not undergo experimentally significant changes.

In order to verify the surface chemistry consistency between the non-plasmonic-CIS and the plasmonic-CIS samples, ^{1}H, ^{14}N, and ^{31}P NMR spectroscopy on both types of CIS was performed (Figures 3.4, 3.5). ^{1}H and ^{31}P NMR measurements were obtained using a 400 MHz Brüker AV400 NMR spectrometer, and ^{14}N measurements with a 500 MHz Brüker DRX500 NMR spectrometer.

A

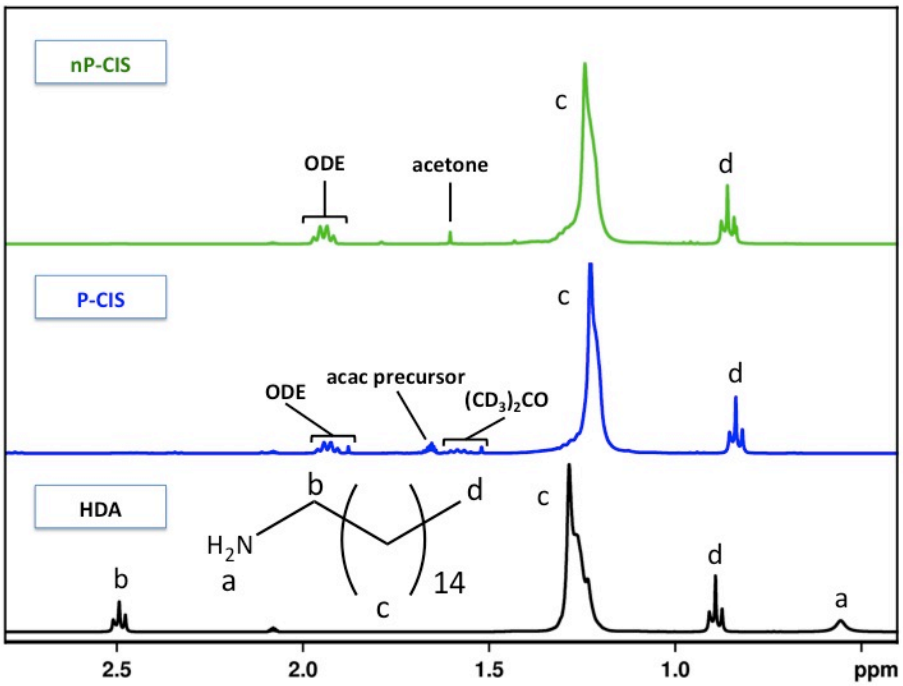

B

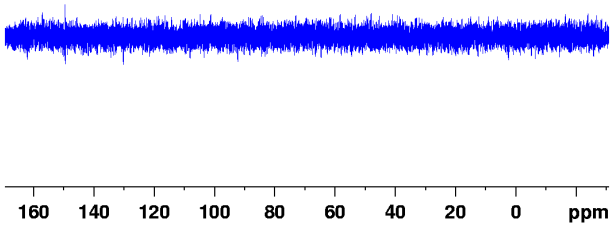

Figure 3.4: (A) ^{1}H NMR spectra for non-plasmonic-CIS, plasmonic-CIS and unbound HDA in toluene-d8. Both QDs experience characteristic peak shifting resulting from the altered electronic environment near the particles' surfaces. Resonance from "a" and "b" hydrogens (inset HDA molecule) is not detected due, again, to proximity to QD surface. Latent amounts of ODE are found in spectra both types of CIS QDs and are labeled in both traces. Likewise, since deuterated acetone was used in initial clean ups for P-CIS, but subsequently found to be unnecessary, acetone was used for the nP-CIS samples, both of which are seen in the corresponding spectra. (B) ^{31}P NMR spectrum of plasmonic-CIS

sample showing no P-resonance whatsoever.

The ^{1}H NMR spectra for unbound HDA, plasmonic-CIS and non-plasmonic-CIS in toluene-d8 are shown in Figure 3.4. Resonance corresponding to the amine ("a") and carbon-1 ("b") protons is not resolved in the QD samples due largely to quadrupole effects in the proximity of the charged surface of the crystals. Correspondingly, the alkyl chain ("c") and terminal $-CH_3$ ("d") protons exhibit an upfield shift from unbound HDA of ~0.05 ppm in both QD samples. Chemical shifts are a trait common to QD NMR studies due to proton proximity to the partially charged crystal surface.[106] ODE is present in very small amounts in both QD spectra as a nonbinding precursor impurity and its contribution to alkyl peaks "c" and "d" can be subtracted from the two peaks through normalization to the ODE alkene peak, yielding the signal due solely to bound HDA in both QD samples. Most importantly, aside from solvent peaks in both as well as a trace amount of acetylacetonate precursor in the plasmonic-CIS sample seen in the well-defined multiplet at ~1.65 ppm, the NMR spectra suggest compositionally identical surface chemistries for the two types of QDs. Further, the lack of aromatic signal in the ^{1}H NMR spectrum, as well as the lack of any signal whatsoever in the ^{31}P NMR spectrum of the analysis of plasmonic-CIS leads to the conclusion that phenylphosphonic acid (PPA), while presumably acting as a stabilizing agent that regulates the reactivity of the cationic precursors during the QD formation process[62] and ensures spherical crystal growth, does not act as a surface-coordinating ligand.

A

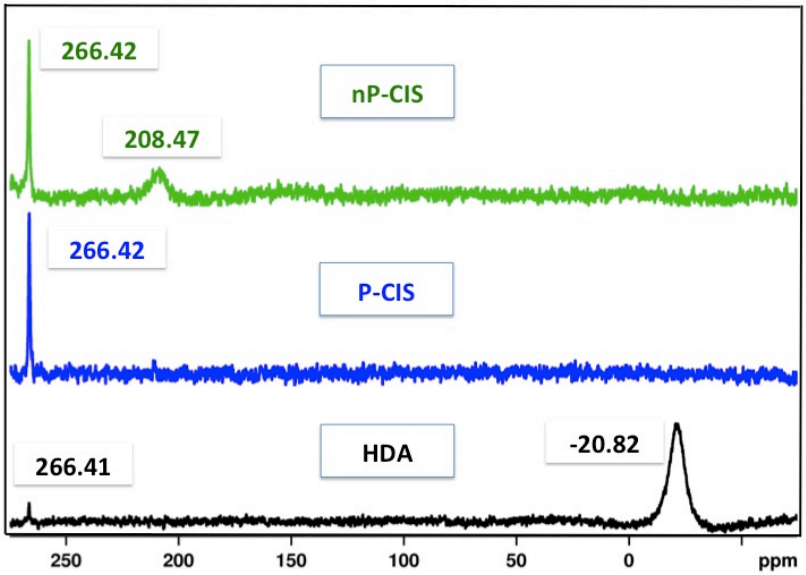

B

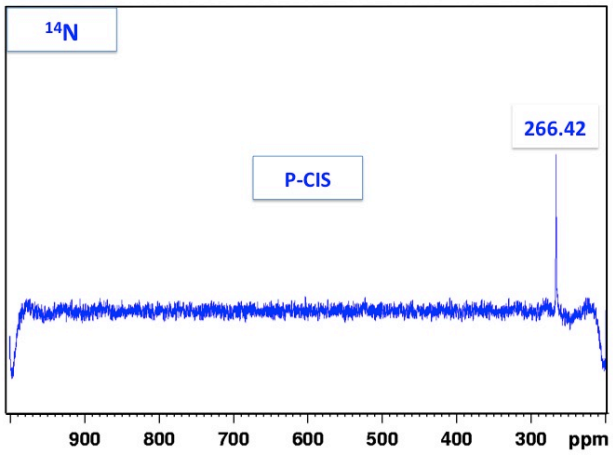

Figure 3.5: (A) ^{14}N NMR spectra for the same samples in toluene-d8. The lone nitrogen atom in bound HDA appears far downfield (208.5 ppm) in the non-plasmonic-CIS sample with respect to unbound HDA (-20.8 ppm). No nitrogen resonance is detected for plasmonic-CIS samples regardless of scan width, which is attributed to extreme peak broadening stemming from highly partially charged plasmonic-CIS surface, which can be seen in the bottom spectrum above. This is hypothesized to be due to the washing out of

nitrogen nuclei resonance in P-CIS samples due to the high density of unpaired spin states in their lattice. (B) Ultra wide scan shows no resonance for ^{14}N nuclei in NMR spectrum for plasmonic-CIS samples.

^{14}N NMR spectra of the same samples studied above in toluene-d8 are shown in Figure 3.5. All three spectra contain a sharp peak at ~266.4 ppm, which can be found in the pure toluene-d8 spectrum and is therefore independent from our QD and HDA analysis. The strong peak at ~20.8 ppm in the unbound HDA spectrum corresponds to the lone nitrogen in the HDA molecule. A highly pronounced resonance shift of ~187 ppm is seen in the non-plasmonic-CIS sample, indicating significant nitrogen deshielding as a result of its interaction with the crystalline surface. Initially, we sought to validate our assumption that the nitrogen-containing DEDC anions present in the non-plasmonic-CIS synthesis were not acting as bound species in the product. In showing that there is only a single ^{14}N NMR peak in the non-plasmonic-CIS spectrum as well as no ^{1}H NMR peaks attributable to DEDC, we were confident in this assertion. However, perhaps more intriguingly, whereas it may be hypothesized that further peak shifting would occur in the plasmonic-CIS QD samples due to enhanced overall QD charge, it was not expected that the HDA signal would be completely absent. Regardless of scan width, no ^{14}N resonance from the HDA-ligated plasmonic-CIS was observed. Although this observation leads to the possible assertion that ^{31}P atoms near the surface of the plasmonic-CIS QDs would also be fully shielded and therefore not detectable in NMR spectra, we feel confident in the binding of solely HDA to the surface of plasmonic-CIS QDs based on the following

observations: (1) the integration of peaks “c” and “d” in the ^{1}H NMR spectrum (less the contribution from ODE) corresponds to the same integration for unbound HDA, (2) the absence of aromatic signal resulting from PPA in ^{1}H spectra, and (3) the relatively high sensitivity of ^{31}P NMR spectroscopy compared to that of ^{14}N (relative sensitivity for equal numbers of nuclei at constant field; $^{1}H : {}^{14}N : {}^{31}P = 1.000 : 1.01 \times 10^{-3} : 6.64 \times 10^{-2}$).

TEM images were obtained using an FEI Tecnai Osiris equipped with ChemiSTEM® EDS capability to show the elemental homogeneity of individual particles and gain further stoichiometric characterization in both the plasmonic- and non-plasmonic-CIS batches (Figures 3.6, 3.7).

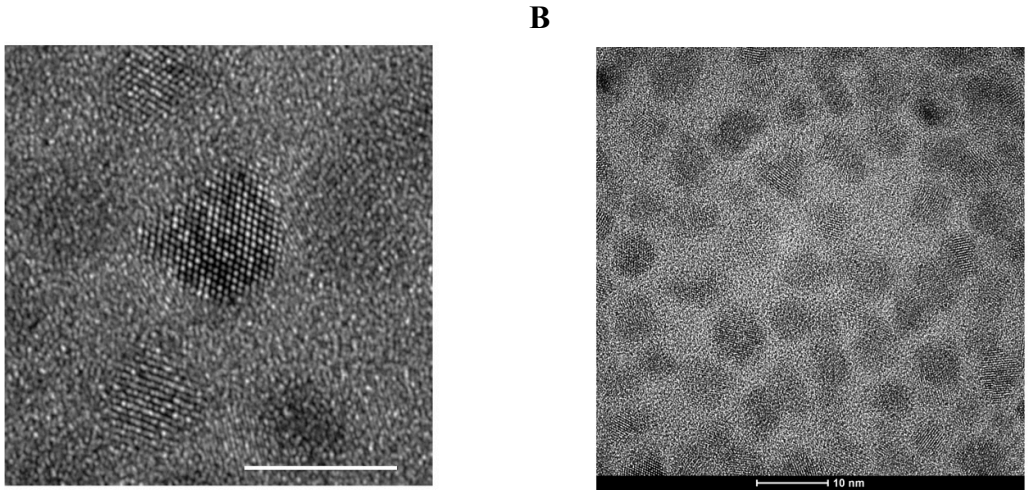

Figure 3.6: (A, B) HRTEM images of non-plasmonic CIS particles with scales bars of 5 and 10 nm, respectively. Particles show good crystallinity and similar size to plasmonic-CIS particles shown in the previous section, which is corroborated by the absorption spectra.

STEM-EDS studies were generally performed with beam spot size set to 4 and a beam current of 0.866 nA. SiN grids were used for these images with $CuInS_2$ QDs because of the low quality of Ni and Ti grids with respect to unavoidable contamination and Cu-background signal. As can be seen in both EDS map images, the particles are homogeneously alloyed, rather than sequestered into Cu-rich and In-rich portions. The randomly cation-deficient nature of the plasmonic-CIS particles is witnessed in the analysis of the corresponding EDS spectrum. In this case the EDS data yields a stoichiometry of $Cu_{1.11}In_{0.72}S_2$ and $Cu_{0.99}In_{1.14}S_2$ for plasmonic- and non-plasmonic-CIS, respectively, reflecting the aforementioned overall stoichiometry trends responsible for the presence or absence of LSPRs in these particles.

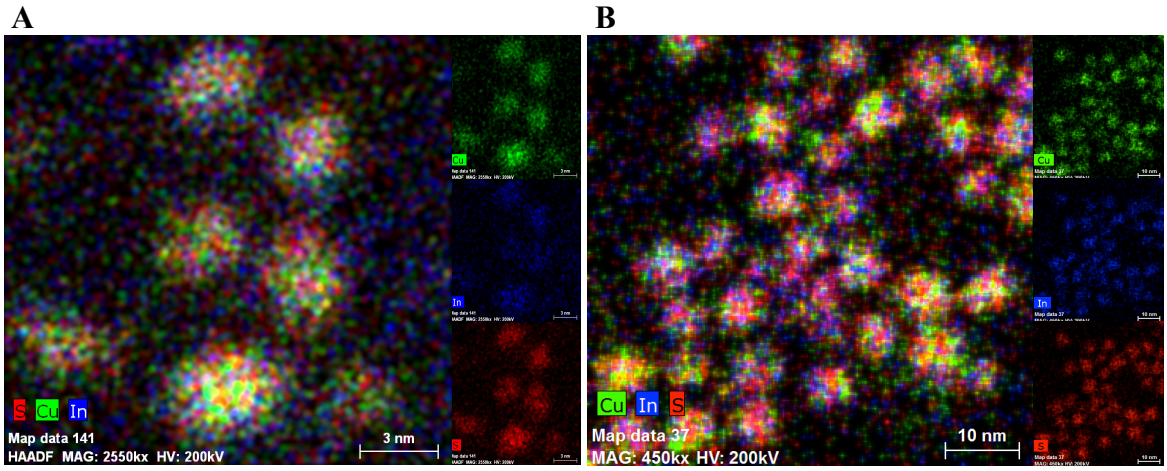

Figure 3.7: EDS-map images of a cluster of non-plasmonic-CIS QDs (A) and a cluster of plasmonic-CIS QDs (B) with scale bars of 3 and 10 nm, respectively. In each image, copper (green) and indium (blue) exist in relative homogeneity rather than being heavily sequestered. Atomic ratios for the two shown samples were calculated to $Cu_{0.99}In_{1.14}S_2$ (A) and $Cu_{1.11}In_{0.72}S_2$ (B). The overall cation deficiency reflects the fundamental

assertion behind the proposed origin of plasmonic modes in plasmonic-CIS QDs, as opposed to the relatively stoichiometric non-plasmonic-CIS QDs.

3.3 Proposed Synthetic Origin of LSPRs in $Cu_xIn_yS_2$ Quantum Dots

Figure 3.8 illustrates the process that we believe leads to the formation of plasmonic modes in plasmonic-CIS QDs as well as the lack-there-of in the non-plasmonic-CIS analogue. In the non-plasmonic-CIS synthesis, DEDC salts of indium (III) and copper (II) are dissolved and heated in a reaction flask with only ODE present. As stated before, ODE is a simple mono-unsaturated carbon chain acting solely as a chemically inert solvent that remains a passive observer during the crystal formation process. The dithiocarbamate anion moieties serve as a sulfur source for the QDs and their decomposition is catalyzed by the injection of a solution of nucleophilic HDA ligands dissolved in ODE. Importantly, the metallic cations and anions share a similar chemical environment in the precursor and growth environments, which presumably allows for a paced and stoichiometric crystal growth process resulting in the formation of relatively few crystalline vacancy defects. Further, this DEDC decomposition occurs gradually upon injection of HDA, with a time of roughly 10 minutes for full decomposition at a growth temperature of 100 °C (Figure 3.1).

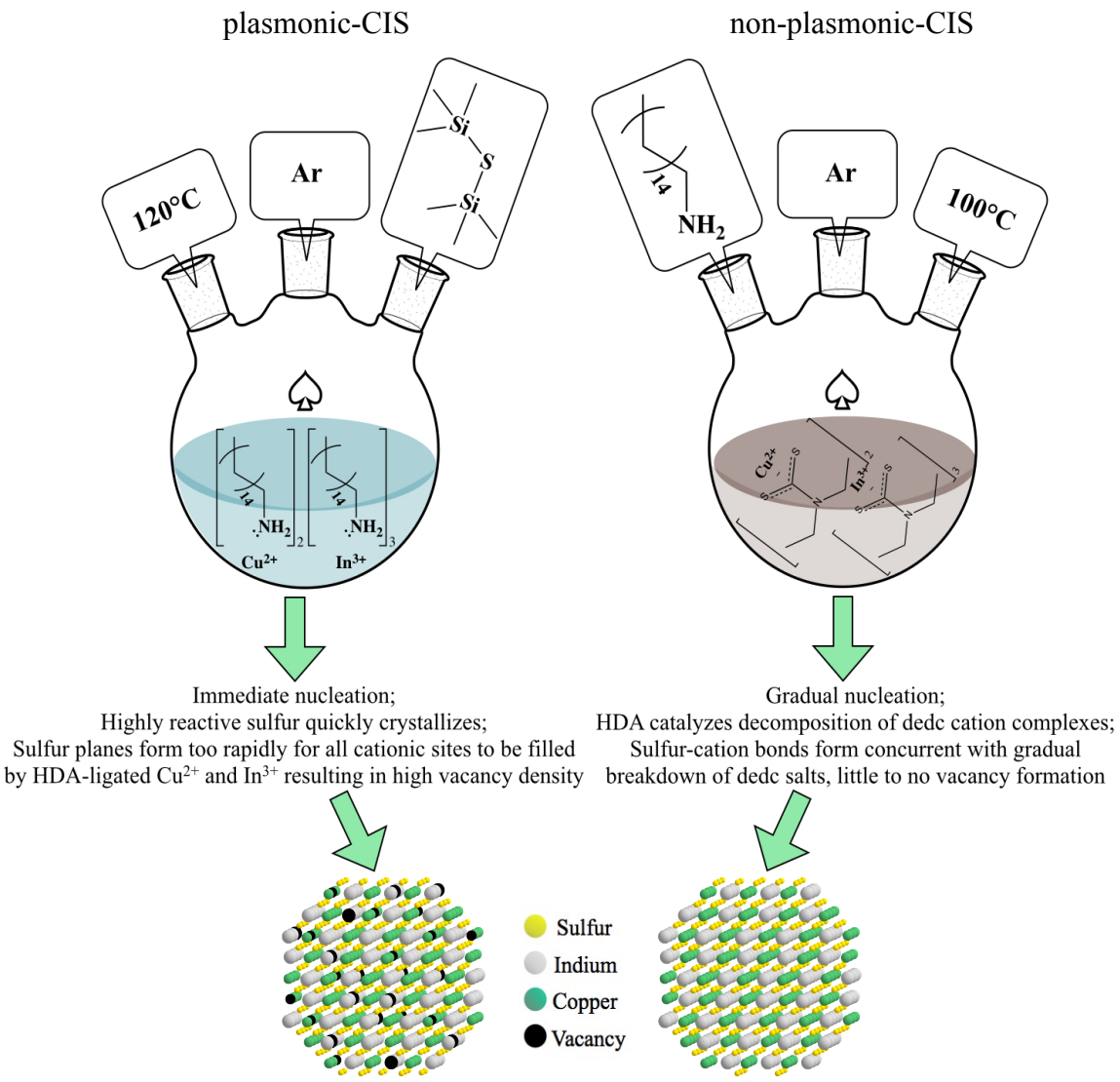

Figure 3.8: Schematic outlining synthetic pathways of plasmonic- (left) and non-plasmonic-CIS (right) QDs as well as proposed mechanism for origin of LSPR modes in plasmonic-CIS samples. While both batches involve an injection step, the plasmonic-CIS synthesis entails the injection of the highly reactive sulfur source, bis(trimethylsilyl) sulfide, to a solution of cation-ligand complexes. The rapid crystal growth, particularly of the sulfur crystallographic planes, in plasmonic-CIS is thought to hinder complete filling of all cationic sites within the QDs, effectively instilling cationic vacancies and ensuring p-type dopant behavior and thus LSPRs. This is in contrast to the more gradual growth of

non-plasmonic-CIS QDs stemming from the decomposition of the cation-DEDC complexes up injection of the nucleophilic HDA molecules.

In contrast, the formation of the plasmonic-CIS particles occurs in a more hectic chemical environment in which the cadenced growth associated with the non-plasmonic-CIS formation is compromised. In this reaction, HDA molecules form ligand-cation complexes in the reaction vessel prior to QD formation. The presence of these complexes is evidenced by the fact that without the addition of HDA in the reaction vessel, the ODE and PPA on their own do not render the Cu (II) and In (III) acac salts soluble. It is not until a nucleophile such as HDA is added to the reaction mixture that the white $In(acac)_3$ and teal $Cu(acac)_2$ solids dissolve, forming a homogeneous precursor. Bis(trimethylsilyl) sulfide (TMS_2S) is a relatively common sulfide anion source in nanocrystal syntheses, particularly those of PbS QDs,[107] because it affords a clean and highly reactive anion source which is known to generally produce monodisperse samples. We hypothesize that the combination of the extremely labile S^{2-} anions with the rather stable and bulky HDA-cation species supports a crystal growth mechanism in which sulfur planes form at a rate that restricts the complete filling of cationic sites. Once growth is quenched through the complete depletion of the TMS_2S, stable HDA-capped particles with inherent cation vacancies result (Figure 3.8).

3.4 Rationales for and Design of Simple Photovoltaics

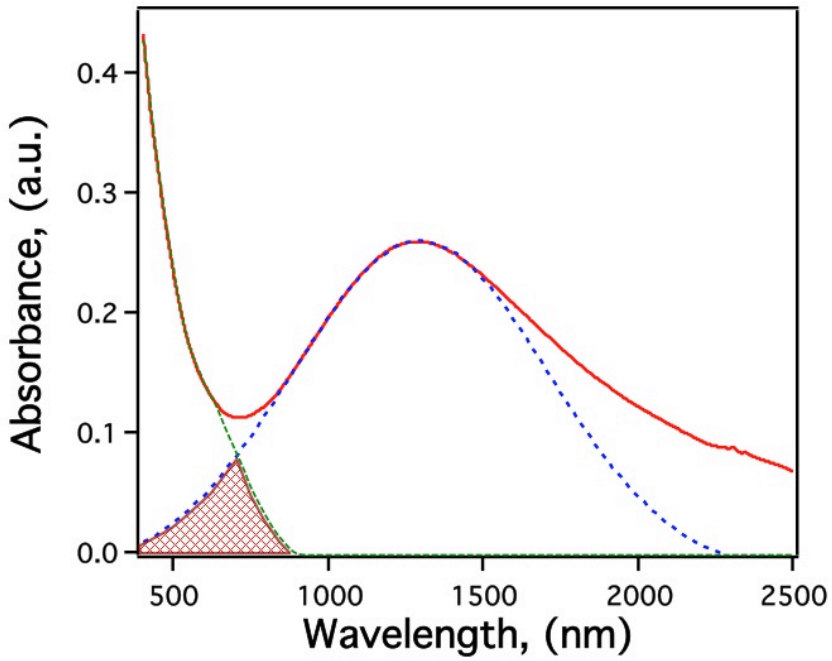

Figure 3.9 Typical plasmonic-CIS absorption spectrum showing peak overlap that facilitates plasmon coupling to photons of energies greater than the band gap. The LSPR peak has been fitted to a Gaussian function, while the excitonic peak has been extrapolated to our best approximation. The red crosshatch pattern highlights the region of overlap. This figure is meant to illustrate the necessity of some form of overlap between frequencies associated with the excitation of plasmon modes and those responsible for band gap excitation; the extrapolation and Gaussian fits are in no way meant to be quantitative.

3.4.1 Plasmon-Exciton Overlap

Crucially, in order to witness any PV efficiency enhancement whatsoever, the LSPR modes in these plasmonic-CIS QDs must exhibit overlap with band gap excitations

for the reason that plasmons must couple with optical transitions in order to observe an antenna effect. This effect is similar to that seen in Forster resonance energy transfer (FRET) studies in which virtual photons can only be transferred from a donor to an acceptor substance through available energy states in both substances. At first observation the two excitation peaks may seem separated, however closer examination of the optical density values in all samples at the minima between the excitonic and plasmonic portions of the plasmonic-CIS absorbance spectra leads to a different conclusion. Figure 3.9 illustrates this observation in showing the necessary peak overlap in a representative plasmonic-CIS absorption spectrum. The LSPR peak has been fit to a Gaussian, and the excitonic continuous peak has been extrapolated to our best approximation. Considering that all spectra taken for these samples are performed under fully blanked conditions in tetrachloroethylene (TCE), the optical density for this sample of ca. 0.1 at the minimum near 690 nm is indicative of peak overlap, which we highlight in the red crosshatch pattern. Importantly, this overlap occurs within the portion of the visible spectrum at which the black body emission of the sun is maximal.

3.4.2 Experimental

Simple quantum dot sensitized solar cell (QD-SSC) devices were prepared from both the plasmonic-CIS and non-plasmonic-CIS samples (Figure 3.10). With the non-plasmonic-CIS devices functioning as controls, this experiment allowed us to gauge the influence of the plasmonic resonant coupling to excitonic modes in the plasmonic-CIS on photovoltaic performance. It is important to note that these solar cells, for simplicity's sake, were not manufactured with the acquisition of high relative IPCE values in mind,

but rather to function as simple PV devices that serve as a benchmark for *comparison* of data between the two types of QDs. Measured electronic parameters are generally much lower than those of typical QD-SSC devices, including those of $Cu_1In_1S_2$ QD-SSCs[38], leading to impractically low efficiency values. Areas of improvement include QD loading, TiO_2 electrode thickness optimization and composition, electrolyte optimization, and band alignment engineering, etc.

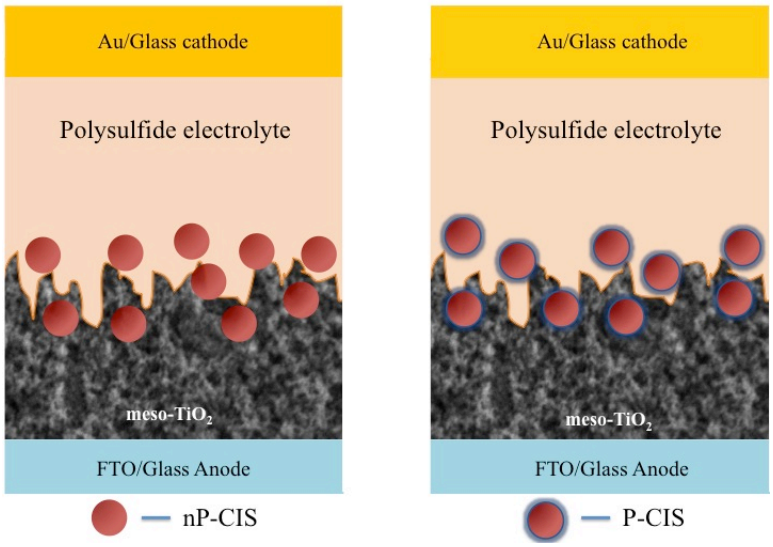

Figure 3.10 Representation of the photovoltaic devices employed to test differences in performance between plasmonic- and non-plasmonic-CIS QD. The cells were assembled identically in every way aside from the species of QD adsorbed to the *meso*-TiO_2 anode.

TiO_2 nanoparticle paste was prepared in house following previously published procedure.[108] 12.5 mL ethylene glycol was placed in a 3-neck round bottom flask and heated to 90 °C with the variac set to 25% in order to have a gradual temperature increase. Once at 60 °C, 2.8 mL titanium isopropoxide was added to the ethylene glycol,

followed by the addition of 10.8 g of citric acid at 70 °C. These additions gradually solvated in the ethylene glycol en route to the 90 °C endpoint. Meanwhile, 5.25 g of Degussa P25 titania nanoparticles (Sigma Aldrich) were added to a mortar. Once at 90 °C, the pale yellow ethylene glycol solution was taken off heat and added to the titania in the mortar. The mixture is then ground vigorously with a pestle for 15 minutes. The paste was diluted 1:3 in ethanol, and 3 drops were spun onto pre-cleaned SnO_2:F (FTO) coated glass slides (MTI TEC 7) at 2500 RPM for 30 seconds. FTO electrodes were cleaned with 3 20-minute sonication cycles in 3% Triton in DI-water, acetone, and isopropanol, respectively. The FTO substrates were rinsed with acetone between each sonication step, and dried with nitrogen once fully cleaned. The TiO_2 anodes were annealed at 450 °C for 1 hour in air and stored for up to 1 week before use. TiO_2 electrodes were soaked in a bath of 1 M 3-mercaptopropionic acid (MPA), which acts as a linking molecule, and 0.1 M H_2SO_4 in acetonitrile over night and subsequently rinsed with acetonitrile and toluene, then placed in a bath of QD solution (either plasmonic-CIS or non-plasmonic-CIS) of 10 mg/mL (optical density of 30 at λ = 500 nm) for 72 hrs. The slightly brown QD-sensitized TiO_2 electrodes were then rinsed thoroughly with toluene and dried in air. Due to the very thin films of TiO_2 formed by this procedure, the color change was not particularly drastic. Gold electrodes were evaporated onto 1”x1” glass cover slips in a Angstrom resistive deposition system. Polysulfide electrolyte was synthesized by dissolving a mixture of 0.5 M Na_2S, 2.0 M S and 0.2 M KCl in a 70% by volume solution of methanol in water. In order to form discreet contacts, 6 reservoirs were created with a rectangular hole punch in a slip of Surlyn tape and placed on the Au electrode. Each reservoir was filled with 7 μL of polysulfide electrolyte, onto which the

QD-conjugated electrodes were carefully pressed and held together with binder clips. An image of a completed typical device can be seen below in Figure 3.11. Current-voltage characteristics were obtained immediately after device assembly by way of a Sciencetech SF150B solar simulator with AM1.5G filter (class A spectral match, class B non-uniformity) connected to a Keithley 2400 sourcemeter controlled by Labview software. The lamp was calibrated to 1.00 full sun with an NREL certified silicon reference diode. The electrode active areas were defined with black tape apertures. Data from 30 devices each of plasmonic-CIS and non-plasmonic-CIS were collected and analyzed on a custom LabVIEW program prepared with help from Chanse Hungerford in the Fauchet lab in the Vanderbilt Department of Engineering.

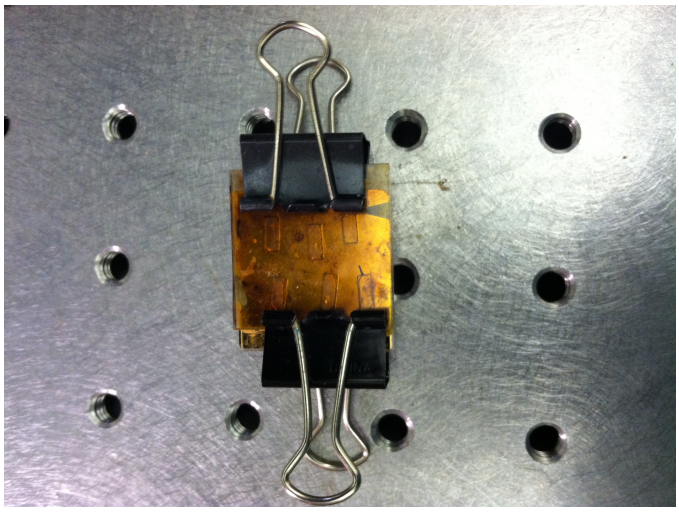

Figure 3.11: Example of complete QD-SSC with 6 reservoirs for sulfur electrolyte.

3.5 Comparison of Photovoltaic Parameters

Figure 3.12 exhibits a set of *J-V* curves that represent the trends in the overall data analysis. Most strikingly, the plasmonic-CIS-sensitized solar cells (plasmonic-CIS-SSCs)

exhibit, on average, 11.5% higher efficiency values than their non-plasmonic counterparts. This efficiency comparison is supported by an unpaired *t*-test resulting in an appropriate *p*-value at a 90% confidence level. *We attribute this increase in performance to a bolstering of absorbance stemming from the plasmonic near field effects present in the plasmonic-CIS-SSCs*. Simplified, this data suggests that more photons absorbed leads to more electrons harvested.

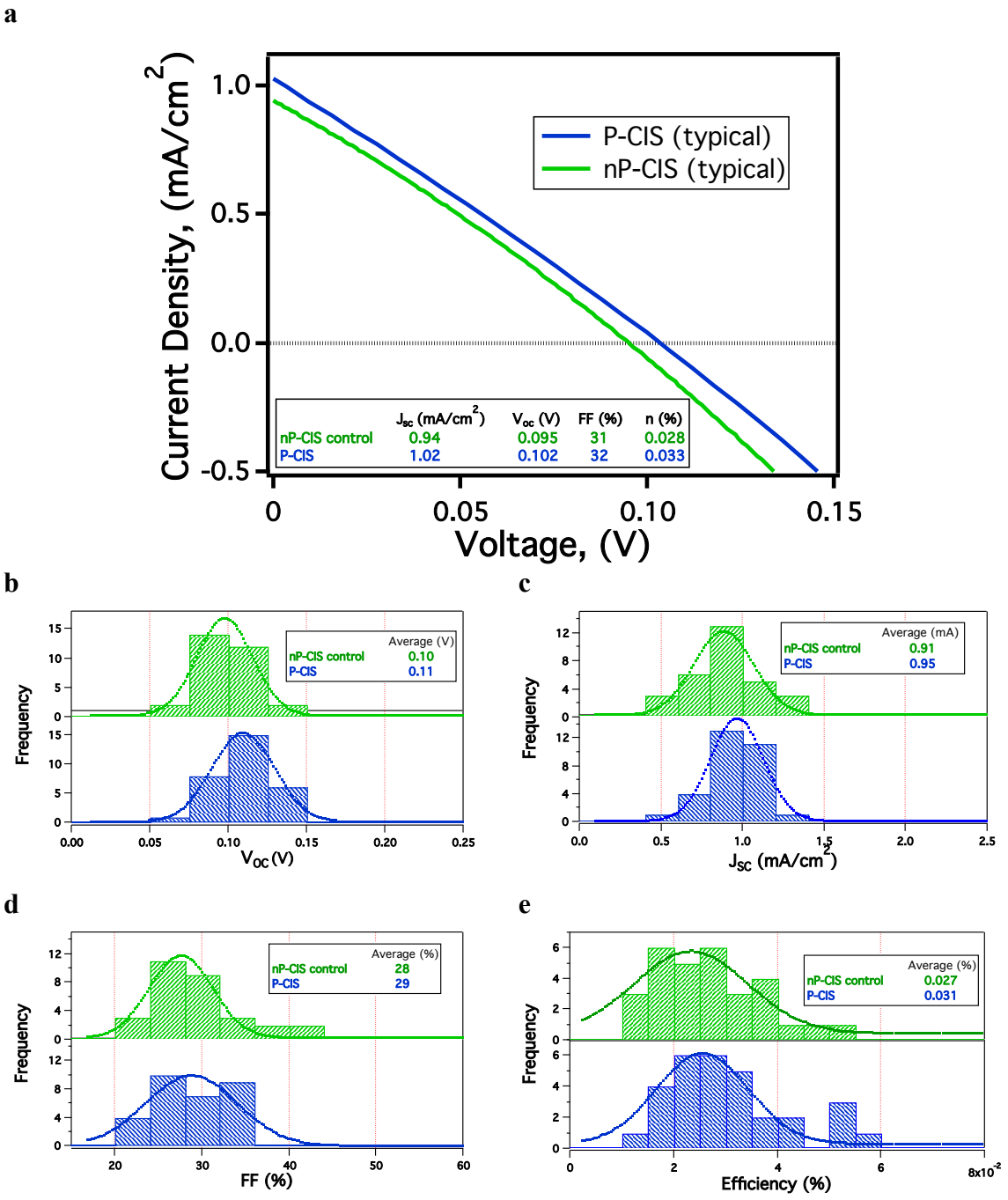

Figure 3.12 Electronic characterization parameters corresponding the plasmonic- (blue) and non-plasmonic-CIS (green) devices. (a) Set of typical *J-V* curves measured under simulated AM1.5G solar simulator at 100 mW cm^{-2} for the two types of QD-SSCs. Relatively superior V_{oc} and I_{sc} values are witnessed for the plasmonic-CIS-SSC by virtue

of increased light absorption and subsequent current generation due largely to LSPR near-field coupling at plasmonic-CIS QDs. (b-d) Histograms showing data for 30 devices each of non-plasmonic- and plasmonic-CIS-SSCs with corresponding distribution fits. On average, plasmonic-CIS-SSCs have efficiencies 11.5% better relative to their non-plasmonic counterparts.

While the root cause of augmented light absorption in plasmonic-CIS-SSCs with respect to J_{sc} are quite straightforward (more absorbed photons leads to more charge excitation), the origin of V_{oc} enhancement are perhaps less conspicuous. The difference in average V_{oc} parameters for the two devices is rather small (0.11: 0.10 V, 10%), however it is still reasonable to expect enhanced V_{oc} in plasmonic-CIS-SSCs for two reasons. First, boosts in light generated current (I_L) result in increased V_{oc} according to

$$V_{oc} = \frac{nkT}{q} ln\left(\frac{I_L}{I_0} + 1\right) \quad (1)$$

where n is the ideality factor, kT/q is the thermal voltage, and I_0 is saturation current which is a function of recombination in the cell. Secondly, V_{oc} scales logarithmically with carrier concentration as

$$V_{oc} = \frac{kT}{q} ln\left(\frac{(N_A+\Delta n)\Delta n}{n_i^2}\right) \quad (2)$$

where kT/q is thermal voltage, N_A is hole concentration, Δn is excess carrier concentration and n_i is intrinsic carrier concentration which is constant for a given crystal type.[109] In this way, V_{oc} values for plasmonic-CIS-SSCs benefit from the nature of the QDs themselves, namely their increased hole concentrations and the current-bolstering LSPR modes that result therein.

It should also be noted that while there does exist a small difference in average V_{oc} values under illumination, the fact that they are not *vastly* different values suggests the two systems are alike enough in their band structures and densities of states (DOS) to form a valid comparison. Sizable decreases in V_{oc} could be expected if the plasmonic-CIS QDs experienced dominant non-radiative relaxation pathways through midgap states compared to the non-plasmonic-CIS samples. Sargent and coworkers have shown that, generally speaking, organic-ligated QDs exhibit non-charge-balanced surfaces due to incomplete passivation,[66] which is detrimental to both current and voltage performance in QD PVs.[110] Nevertheless, while there is little doubt mid-gap states are present in both samples due to unpassivated surface states seen in presumably all organic-coated QD systems, it seems that acceptor sites *within* the plasmonic-CIS crystalline structure do not contribute to heavily detrimental midgap states in any significant manner with respect to V_{oc}, compared to the non-plasmonic-CIS.

Fill factor (FF) values suffer from detrimental amounts of series and shunt resistances presumably stemming for poor device optimization. It is important, again, to note that previous reports concerning "optimized" CIS-based QD-SSCs of similar architecture have shown FFs upwards of 45% and IPCEs of roughly 4%,[102,111] both of which are competitive with parameters of analogous Cd- and Pb-chalcogenide-based QD-SSCs in the literature.

note: Much of the of the above chapter was adopted with permission from: Plasmonic CuxInyS2 Quantum Dots Make Better Photovoltaics Than Their Nonplasmonic Counterparts. J. Scott Niezgoda, Eugene Yap, Joseph D. Keene, James R. McBride, and Sandra J. Rosenthal. *Nano Letters* **2014** *14* (6), 3262-3269. Copyright 2015 American Chemical Society.[22]

Chapter IV.

ELECTRON BEAM-INDUCED CURRENT STUDIES IN PbS QUANTUM DOT THIN FILM PHOTOVOLTAICS

4.1 Introduction

4.1.1 QD-Based Photovoltaics

In the years prior to 2010, QD-based photovoltaics (PVs) existed essentially as an interesting topic to which nanomaterials researchers could point as a totally electrically tunable and extremely low cost, low material paradigm for future-generation alternative energies.[42] In these years, much of the global attention to QD PVs was centered upon harnessing QDs as stable and highly absorbent inorganic analogs to ruthenium dye molecules in Grätzel cells (dye sensitized solar cells) adhered to TiO2/ITO electrodes with a liquid or polymeric electrolyte hole transporter, deemed QD sensitized solar cells (QD-SSCs).[41,112-119] In particular, the Kamat lab at Notre Dame published a considerable canon of studies utilizing CdSe QDs—and, subsequently $CuInS_2$ QDs—in which they have recently achieved upwards of 5% incident photon conversion efficiency (ICPE), no where near the roughly 15% needed to make these devices truly industrially viable.[120] These devices are advantaged by the ability to reach relatively high V_{OC} and FF values because the liquid electrolytes in general can be very good hole transporters, limiting back recombination at the QD-TiO_2 interface. However, the single monolayer of QDs simply cannot absorb enough light to produce technologically relevant J_{SC} values at this time and these devices seem to be stagnating in terms of their yearly efficiency enhancements.

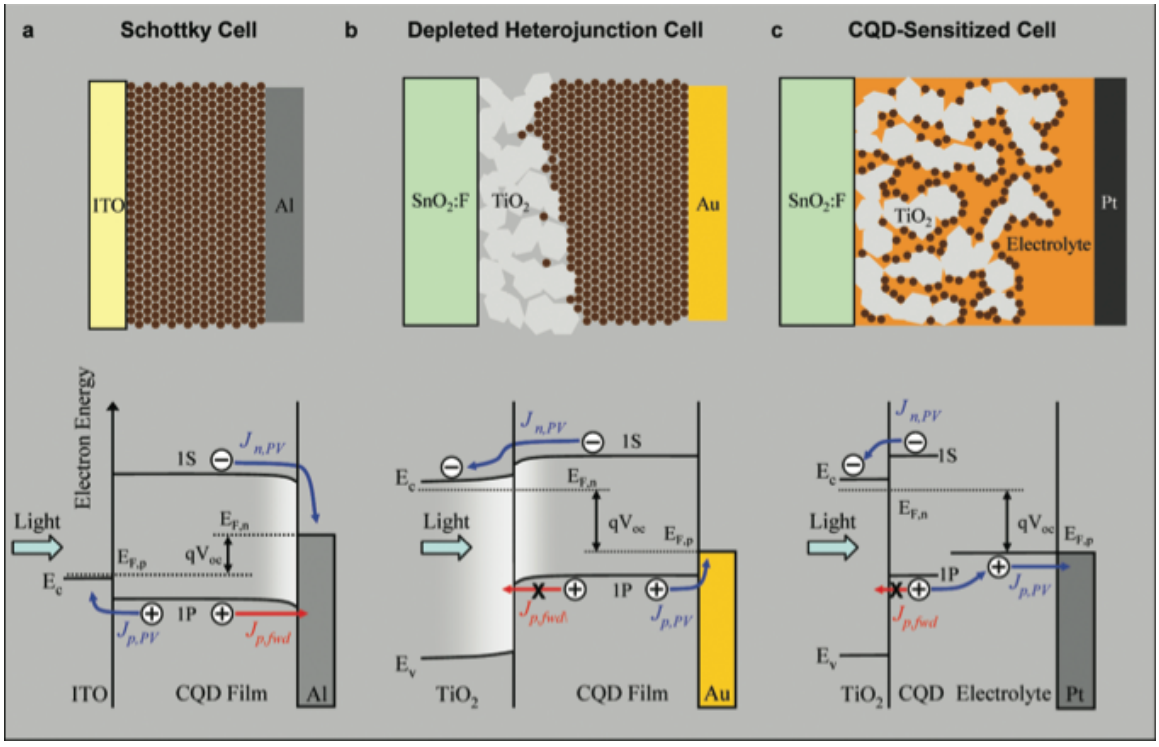

Figure 4.1: Schematic depicting the three main architectures of QD-based PVs, adapted with permission from Pattantyus-Abraham, et al., copyright 2015 American Chemical Society.[121] (a) Shottky junction PbS QD PV. Light enters through the ITO cathode and progresses toward the back Al Shottky junction. Minority electrons often must travel the entire length of the QD film in order to be collected, a process, which is highly unfavorable. (b) Depleted-heterojunction colloidal quantum dot (DH-CQD) solar cell. A heterojunction exists between QDs and a metal oxide, in this case TiO_2, is employed as a rectifying junction. Excitation occurs at the anode, and the device is designed so that ideally the entire active layer is within the depletion region of the p-n junction. (c) QD-SSC (labeled here "CQD-sensitized cell" for "colloidal quantum dot"), an analog to dye sensitized electrolytic PVs. These devices are disadvantaged by being limited to a monolayer of active absorbers as well as the presence of finicky liquid electrolytes.

An attractive alternative to QD-SSCs are those that utilize solid thin films of QDs which mimic more classic generation I and II PV architectures. The elimination of liquid in these devices increases the stability of them to corrosion and any leakages that may occur, and the solution layer-by-layer processability of thin films suggests a straightforward transition to industrial manufacturing. Early reports of thin film QD solar cells were quite simple and relied heavily on Schottky junction architectures in which a transparent conductive electrode (ITO) acts as an cathodic window and a back contact anode of aluminum forms a Schottky junction with the QD active layer,[122-124] which can be succinctly visualized in Figure 4.1, adopted from a subsequent 2010 report from the Sargent lab at the University of Toronto.[121] Schottky junctions, or barriers as they are often called, are rectifying junctions between a semiconductor and a metal. In the case of PbS QD-based PVs, the Al-PbS Schottky junction funnels electrons into the Al anode through band bending to the deep work function of Al while blocking the passage of holes—hence the term "barrier". Generally speaking, the high density of charged surface states in ITO causes the Fermi level to be pinned at the ITO-PbS interface which all but eliminates band bending at this ohmic interface, however the ITO in this case continues to act as a workable cathode. Besides this, the efficiencies of Schottky devices suffer from the fact that illumination occurs at the ohmically contacted side, creating the requirement that minority carrier electrons in the p-type PbS film often travel the entire width of the active layer in order to be collected. The low diffusion length of both holes and electrons in QD thin films renders this architecture disadvantageous from the start. Schottky junction QD PVs are generally limited to below 2% IPCE values.

With the 2010 introduction of the so-called depleted-heterojunction colloidal quantum dot photovoltaic (DH-CQD PV) in the paper from which the above figure stems, the field of QD PVs witnessed a burst of interest, proliferation, and, perhaps for the first time, a real possibility of industrial viability. The term "depleted-heterojunction" refers to the interface between a wide band gap metal oxide (in this case TiO_2) and QD layer (PbS), the dimensions of which are engineered tuned so that, ideally, the entirety of the PbS active layer is within a depletion region. *DH-CQD solar cells attempt to harness the electric field-driven current, which takes place within a depletion region of an active layer, in order to eschew the horrible charge carrier diffusion lengths (average distances which electrons and holes can diffuse without the influence of an electric field) in QD solids*. Besides the advantage of fully drift-driven current production, DH-CQD solar cells also have the advantage of having light enter at the rectifying anode side, promoting minority carrier separation.

The main point to emphasize in this study is as follows: whereas with classical semiconductor thin film systems (p-Si, a-Si, GaAs, CdTe, etc.) there have been considerable efforts to classify their electrical properties to befit accurate modeling and charge transport properties *ab initio*, QD solids are inherently difficult to model and characterize at this time. Their reliance on hopping-based transport, abundance of organic molecular moieties, and, perhaps most importantly, the sensitivity of their doping profiles to surface treatments and varying stoichiometric inconsistencies renders QD thin films an inherently challenging engineering problem. To this point, an empirical basis for the optimization of DH-CQD devices is highly desirable for the researchers within the field.

4.1.2 Electron Beam-Induced Current Microscopy

Electron beam induced current (EBIC) studies offer an exciting and relatively new method for visualizing current production within the active layer of a photovoltaic cell. In EBIC, electrons in the form of a high energy focused and rastering beam from either a scanning electron microscope (SEM) or a scanning transmission electron microscope (STEM) are used to excite electron-hole pairs, mimicking photons. Leads collect current production from the front and back electrodes which is spatiotemporally correlated to create what eventually becomes a "map" of current production in a given device cross section. A current amplifier set up is used to attain experimentally relevant current values. EBIC is ideal for new experimental generation III devices employing very thin absorber films because one is able to couple the EBIC recording with high-resolution microscopy in the sub micron realm. In this study Dr. Amy Ng, a previous group member in the Rosenthal lab, performed the cross section milling, preparation and EBIC measurements (thorough details on EBIC testing and sample preparation specifics as they pertain to this project should be found in her dissertation document[125]) on devices that I synthesized, altered and for which I acquired I-V characteristics.

4.2 Experimental

4.2.1 Synthesis of PbS Quantum Dots

The PbS QDs in the study, for reasons which will be explained in subsequent sections, must be highly monodisperse and of the utmost crystallinity, with surface ligands that are both stably bound and easily replaceable. A popular synthesis developed by Hines and Scholes is able to produce high yield reactions at low temperatures with

relatively inexpensive reaction precursors.[107] The reaction conditions and setup are particularly important in the formation of PbS quantum dots with respect to Cd and Zn chalcogens and ternary I-III-V compounds. It took many failed reactions yielding stably soluble, yet simply low quality quantum dots for a process to be optimized for application to thin films. The following procedure is sufficient for formations of high quality PbS quantum dots of varying size.

Pb(II) oxide (>99%), bis(trimethylsilyl)sulfide (TMS_2S) (synthesis grade), oleic acid (>90%) (HOA) and octadecene (ODE) (90%), were obtained from Sigma-Aldrich. It was found that ultrapure oleic acid did not make a noticeable difference from the reagent grade 90% batches and the price difference was sufficient to continue usage of the less expensive reagent grade. TMS_2S is never opened outside of a glovebox and should always be handled with care. Similarly, PbO should be handled with extreme care. Inhalation or ingestion of any kind is very toxic and glassware should be rinsed thoroughly with organic solvents prior to sink water rinsing.

For the synthesis of E_g=1.3 eV (955 nm) PbS QDs with diameters of 3.5 nm, 2 mmol PbO (0.45 g) is combined with 1.5 mL HOA and 18.5 mL ODE in a 100 mL 3-neck round bottom flask with magnetic stir bar. The flask is connected to a Schlenk line with temperature probe, vacuum/purge gas valve and septum on its three necks and heated to 95 °C under roughing pump vacuum overnight. Achieving a high vacuum or even mTorr is not particularly necessary in this stage; the vacuum atmosphere serves to ensure complete removal of both dissolved oxygen as well as any water present in the precursors or produced during the Pb-oleate creation as the O^{2-} anions from the PbO precursor combines with two equivalents of protons from HOA molecules. This is a

crucial step in the production of high quality PbS QDs—the reaction solution must be completely free of water and oxygen. On the same Schlenk line, and during the same overnight night vacuum cycle, 10 mL of ODE is added to a separate 25 mL 3-neck round bottom flask with septum which is heated to 80 °C overnight under the same vacuum atmosphere. The next day, the flasks are purged with argon and the Pb-oleate flask is increased to 120 °C in preparation for growth.

For the TMS_2S injection step, 0.5 mmol (0.120 mL) is pulled into a plastic 1 mL syringe in the glovebox, which is capped and wrapped in Parafilm. The syringe is quickly transferred from the antechamber to the back of the fume hood. Care is taken to wear full protective equipment including oversized gloves, goggles and lab jacket. The TMS_2S is injected into the pure ODE flask and allowed to fully incorporate, at which point the stirrer is stopped and the ODE/ TMS_2S is pulled into at 30 mL syringe with an 18-gauge needle. The 18-gauge needle is quickly replaced by a 12 gauge injection needle and the solution is injected as swiftly as possible into the 120 °C Pb-oleate solution. Nucleation occurs immediately with the highly reactive S source and growth is quenched essentially immediately. The reaction is removed from the heating mantle and cooled to 50 °C externally with compressed air. The reaction contents are split between four centrifugation vials and each is filled with acetone and centrifuged for 10 min at 7,500 RPM in ambient air. The supernate is discarded and each pellet is dissolved in ~5 mL toluene, followed by flocculation with acetone and a subsequent 10 min, 7,500 RPM centrifugation step (x2). Finally, the pellets are dissolved in another 5 mL toluene and flocculated with ethanol, followed by the same spin cycle. For QDs synthesized for application to solar cells, the final pellets are kept dry and quickly brought to the clean

room for storage in the Angstrom glovebox. The QDs are then dissolved in 10.2 mL octane in the glovebox. 0.2 mL of the solution is reserved and removed from the box to be massed. A 0.1 mL aliquot of the stock QD solution is placed in a tared metal weigh boat and allowed to evaporate. The new weight of the boat and dried dots (multiplied by ten) yields the concentration of the stock solution in mg/mL. The stock solution is then diluted in the glovebox to 38 mg/mL with octane and stored for device fabrication.

As a final note, changing the ratio of HOA:ODE in the precursor reaction vessel modulates QD size. For this study, PbS QDs of E_g=1.3 eV which are band-level optimized for current production in DH-CQD PVs were synthesized as described above. Additionally, larger QDs of E_g=0.83 eV were synthesized for reasons which will be described in subsequent sections. The synthesis of these QDs is performed in the exact manner as for that of the smaller QDs, the only difference being that the Pb-oleate precursor reaction vessel is void of ODE, with 18 mL of HOA instead (0.45 g PbO, 18 mL HOA). The extreme excess of HOA decreases the reactivity of Pb^{2+} cations during the injection step, leading to less concurrent nucleation processes and allowing those fewer sites of nucleation to grow into larger crystals until the S source is depleted. The large dots are cleaned up and stored in the exact manner as the smaller dots.

A

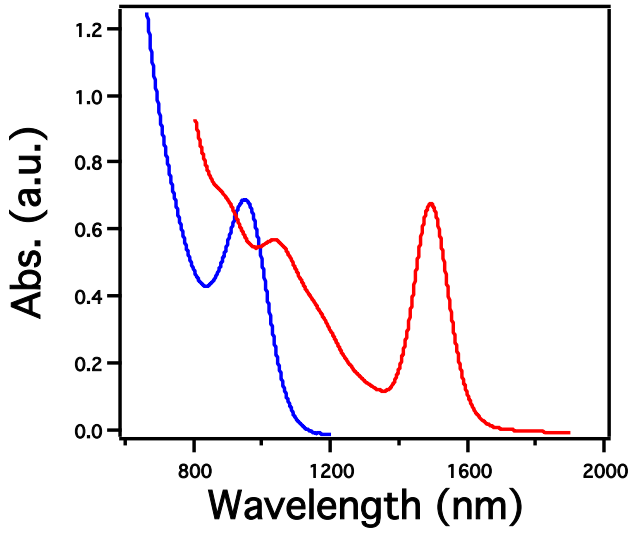
Abs. (a.u.)
1.2
1.0
0.8
0.6
0.4
0.2
0.0
800
1200
1600
2000
Wavelength (nm)

B

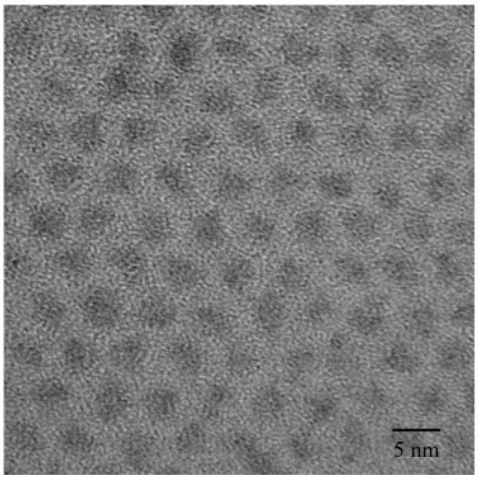
5 nm

C

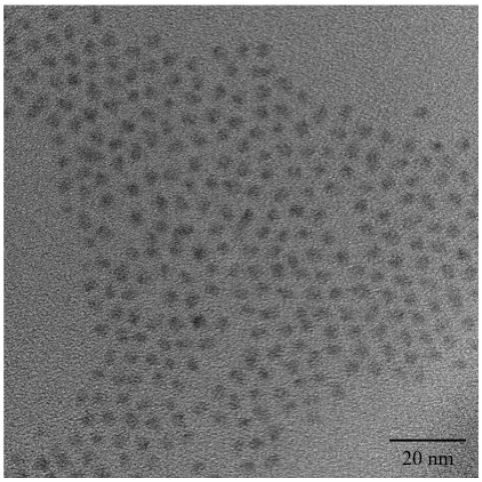
20 nm

D

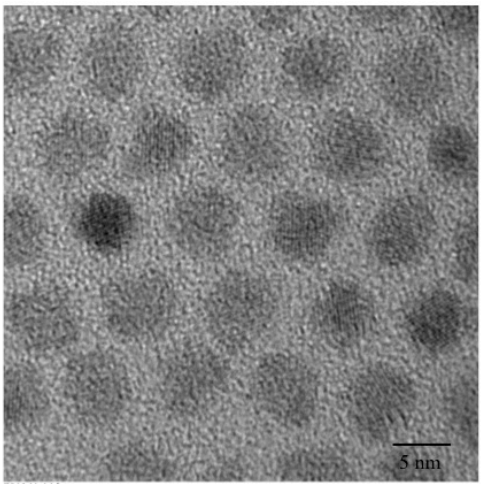
5 nm

E

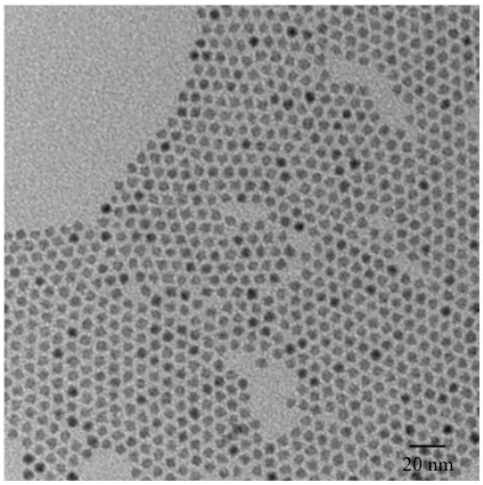
20 nm

Figure 4.2: (A) VIS-IR absorption spectra of E_g = 1.3 eV (955 nm) (blue curve) and E_g=0.83 eV (1500 nm) (red curve) PbS QDs. Strong and narrowfirst excitation features in the curves suggests narrow size dispersity and crystallinity. (B-C) HRTEM images of 1.3 eV QDs described by the blue curve in "A", and (D-E) show similar images of the 0.83 eV batch of larger diameter QDs described by the red curve. Both batches display narrow size dispersion and form hexagonal packed thin films when deposited on TEM grids.

4.2.2 Assembly of PbS Quantum Dot Solar Cells

The construction of DH-CQD PbS PV devices begins with the preparation of the TiO_2 anodes, adapted from similar methods common to these devices.[85] FTO electrodes were cleaned with 3 20-minute sonication cycles in 3% Triton in DI-water, acetone, and isopropanol, respectively. The FTO substrates were rinsed with acetone between each sonication step, and dried with nitrogen once fully cleaned. Generally speaking, 6 electrodes were prepared at a time due to size constraints of the sonicator (a single evaporation dish was used to hold FTO) as well as the tube furnace. $TiCl_4$-water baths were used on two separate occasions in the preparation of TiO_2 electrodes—first, as a thin seed layer and subsequently as a means to interconnect the spun-cast thin film. Accordingly, the fully cleaned FTO substrates are placed in a 50 mM $TiCl_4$ bath which is prepared by carefully injecting 0.65 mL $TiCl_4$ (from glovebox) into an evaporation dish containing 50 mL DI water at 70 °C on a hot plate in the back of a fume hood. A thermocouple is used to as a thermometer; the temperature settings on hotplates do not yield accurate results. When preparing these solutions, a large amount of "smoke" will be

created and great care must be taken to not expose oneself to these fumes, which is a combination of TiO_2 nanoparticles and HCl vapor. The FTO electrodes are soaked in this bath for 30 min at 70 °C, then annealed in the tube furnace in ceramic boats with the following heating cycle: 25 °C to 500 °C, 20 min; 500 °C for 60 min; 500 °C to 25 °C, 20 min. In reality, the final cool down step generally takes much longer than 20 minutes.

For these electrodes, commercial TiO_2 paste purchased from Dyesol is used, which consists of P25 TiO_2 nanoparticles dispersed in terpineol, a pleasant-smelling organic aromatic with proper solubility and viscosity for spin coating procedures. The concentration of TiO_2 in the spin coating solution, at least in all the studies performed in this study, scales linearly with the final thickness of the annealed film. For a 500 nm thick film, 0.155 g TiO_2 paste is diluted with 0.47 g ethanol in an eppendorf tube and vortexed until fully dissolved. For the spin coating procedure, 10 drops of the diluted pasted are applied to the $TiCl_4$-treated FTO electrodes on the spin coater and the solution is allowed to spread for several seconds. The electrode is then spun at 300 RPM for 5 seconds, followed by 1500 RPM for 45 seconds. After removing from the sonicator, an ethanol-soaked cotton swap is used to wipe a corner of the electrode clean for an eventual contact. These electrodes are then placed on the center of a hotplate which is then set to 390 °C for 30 min. This process burns off most of the organic material in the thin film (the electrodes will turn light brown in the process before becoming clear again).

A final $TiCl_4$ bath, identical to the previous one, is performed and the electrodes are washed thoroughly with DI water and dried with compressed nitrogen. They are annealed once again with the same 500 °C process and stored for future use for up to 1 week outside of the glovebox, or indefinitely inside of the glovebox.

Inside the N_2-filled glovebox, a solution of 1% by volume (100 mL total) solution of 3-mercaptopropionic acid (MPA) in methanol is prepared in a capped jar, while another jar is reserved for pure methanol. The devices are assembled in a layer-by-layer fashion in the glovebox which has been developed and optimized for what has been found to yield acceptable results in the VINSE cleanroom. The exposed FTO corner of a TiO_2 electrode is covered with copper tape and is then placed on the spin coated in the cleanroom glovebox and spun at 2500 RPM for 45 seconds. Once up to the RPM set point, 3 drops of the 38 mg/mL solution of PbS QDs is applied to the electrode. After the spin cycle, the device is removed from the spin coater by the copper tape corner with tongs and dipped into the MPA solution 4 consecutive times (roughly one second per dip) and then the same in the pure methanol to rinse the device of displaced HOA ligands and excess MPA molecules. These three steps constitute one "layer". Each layer deposits roughly 20 nm of solid MPA-coated QD thin film. As an aside, the MPA ligands act to not only allow QD-QD coupling to facilitate charge transport, but also to render the thin film insoluble in nonpolar solvents, thereby preventing it from being washed away with further QD additions.

After achieving the desired device thickness, the QD layers should be glossy and largely consistent. The devices are then placed face down in the custom mask for cathode evaporation (note: prior to any device assembly, one should check that all the FTO electrodes being used are able to fit in the custom mask—MCI Corp. does not do a good job of controlling the size of FTO substrates and they can often be too large for the brass mask). The devices and mask components are passed through the antechamber and loaded through to the glovebox side into the resistive evaporator chamber of the

Angstrom deposition system, which is stocked with sufficient Au and Ag pellets in the corresponding source locations. A program is prepared for the deposition of the electrodes in a resistive evaporator located within the Angstrom deposition system, which deposits 20 nm Au and 300 nm Ag. The MoO_3 deposition layer for these studies is usually skipped, as benefits from the MoO3 interlayer which has been reported in the literature were not witnessed in these efforts.[126] The deposition is run in "auto" mode with 0.2 Å/s Au and 2.0 Å/s Ag. After deposition, the devices are removed through the glove box side and placed face down in wafer holders and are not removed from the glovebox until they are ready to be tested.

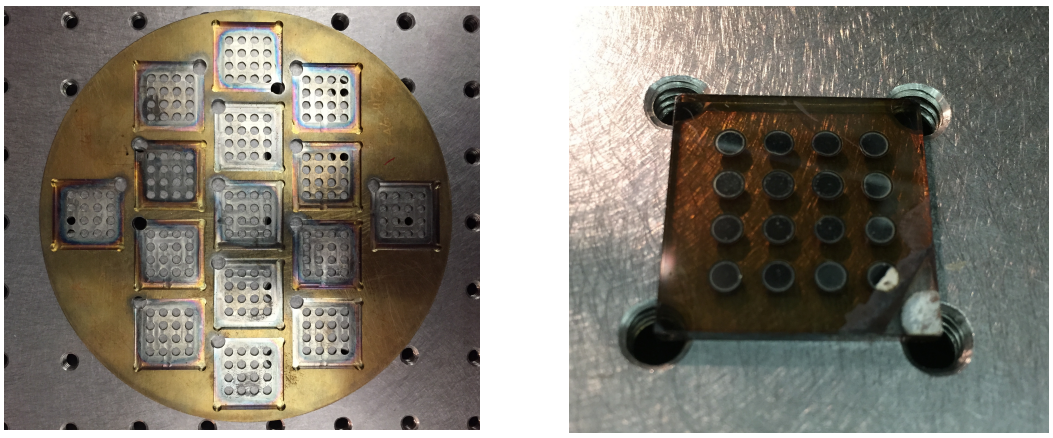

Figure 4.3: Images of the custom cathode deposition mask (left) and well as a completed PbS DH-CQD PV device. Notice the glossiness of the device contacts and brown PbS layer. Attaining smooth and crack-free films was a challenging endeavor, which required considerable personalization and optimization as the procedures reported in the literature were not successful when attempting to replicate. Each of the 16 contacts was measured for every device, yielding a considerable amount of data compared to previous designs.

4.2.3 Design of Testing Apparatus and Testing of Devices

A fully custom setup for the testing for PV devices was designed and assembled for the pairing of devices made using the brass mask to the solar simulator located in SC 7910 (Figure 4.4). The testing setup consists of a plastic device holder with 16 spring-loaded leads matching each deposited cathode contact, and 1 lead matching the back FTO anode contact. The single anodic lead is connected with an alligator clip straight to the Keithley 2400 sourcemeter. The 16 cathode leads are fed into a breadboard connected to a multiplexer shield (Mux Shield II) atop an Arduino Uno module. The mux shield filters all but one lead at a time into the Arduino unit, and is controlled by the LabVIEW program (designed with considerable help from Chanse Hungerford in the Fauchet lab at Vanderbilt). The Arduino has an output lead that is then run to the Keithley for I-V characterization. An iris aperture is placed between the Sciencetech AM1.5 solar simulator and the device holder in order to illuminate only the contact that is being measured. The lamp measuring distance is calculated to 1.00 Sun every 6 months with an NREL certified PV standard provided by Dr. Nathaniel Smith at Middle Tennessee State University. The device area that corresponds to this mask and testing setup is 0.071 cm^2 and V sweeps are taken from -0.5 to 1.0 V, at 0.02 V steps with 250 ms stoppage between each reading. The program automatically archives the result of each reading with a bitmap image of the I-V curve and a .txt file of the I-V data as well as efficiency and electrical characterization parameters. For each contact, a dark curve is taken prior to acquiring an illuminated curve (there is a switch for dark/light on the LabVIEW panel which causes the program to save data as light_ or dark_).

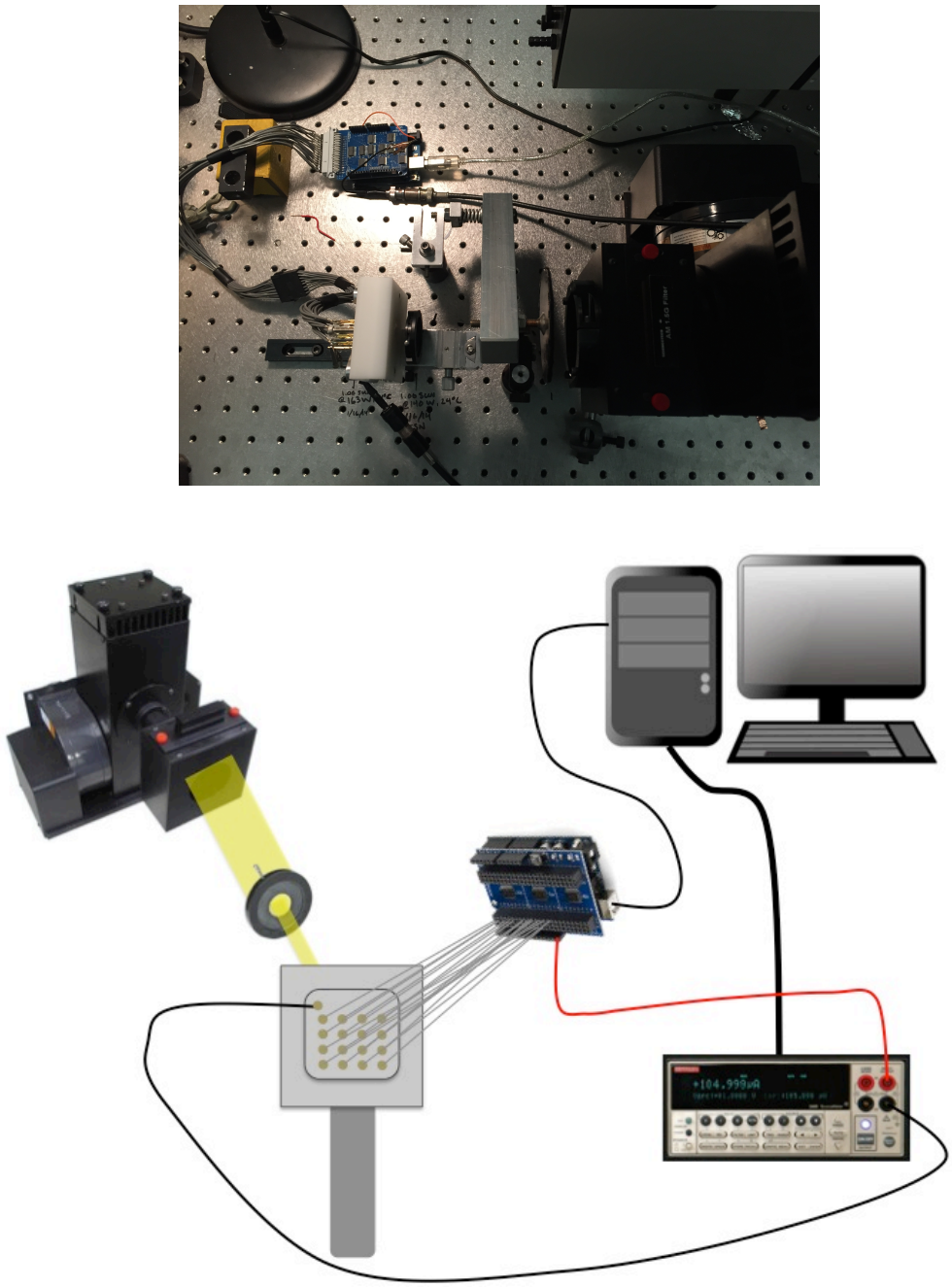

Figure 4.4: (above) Image of the testing setup. For the simplicity, a schematic was prepared and is shown below. Light for the AM1.5G solar simulator is shown onto the a single contact of the device holder through an iris aperture. All 16 cathodic leads are run into an Arduino module with a multiplexer shield, which reads from LabVIEW to filter

all signals but the one corresponding to the contact being measured. That signal is then run out to the Keithley that is also linked to LabVIEW for the voltage sweep and I-V curve characterization statistics.

4.2.4 Preparation of Cross Sections, EBIC Measurements

As mentioned before, Dr. Amy Ng performed all preparations of import pertaining to the acquisition of cross sections and EBIC in this project. Briefly, cross sections used for STEM-EDS chemical mapping protocols were obtained through a dual-beam Ga^{3+} focused ion beam (FIB) lift out procedure of completed PbS DH-CQD devices for which electrical characterization had already been performed. The device lamella is attached to an Aduro sample holder, which is used as a typical TEM sample grid for imaging, as seen in the figure below.

A

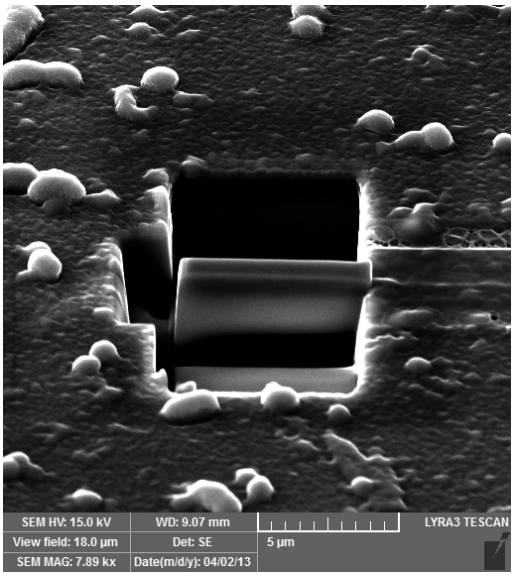

B

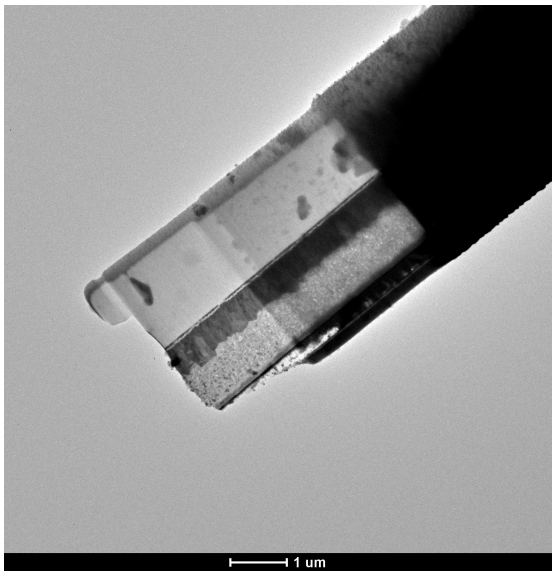

Figure 4.5: (A) A cross section of a completed PbS QD device used for STEM-EDS cross sectional imaging, imaged with a Ga beam in a dual beam FIB during the etching process, pre lift out. (B) Image of a completed cross section post lift out, positioned on an Aduro sample holder used for the STEM-EDS cross sectional images seen in this chaper.

The preparation of samples for EBIC studies differs completely from those of cross sectional imaging. Rather than performing FIB on these samples, which implants significant amounts of gallium atoms throughout the device and severely hinders device performance. For EBIC sample preparation, a full device is essentially cut into smaller and smaller pieces with a diamond saw until a desired size is reached. The device cross section is then polished with argon ions and fit into a sample holder, which in our case is a commercial holder manufactured by Gatan (SmartEBIC). The cross sectional exposed counter electrodes of the device are attached to leads and the EBIC study is performed on an S4800 Hitachi SEM.

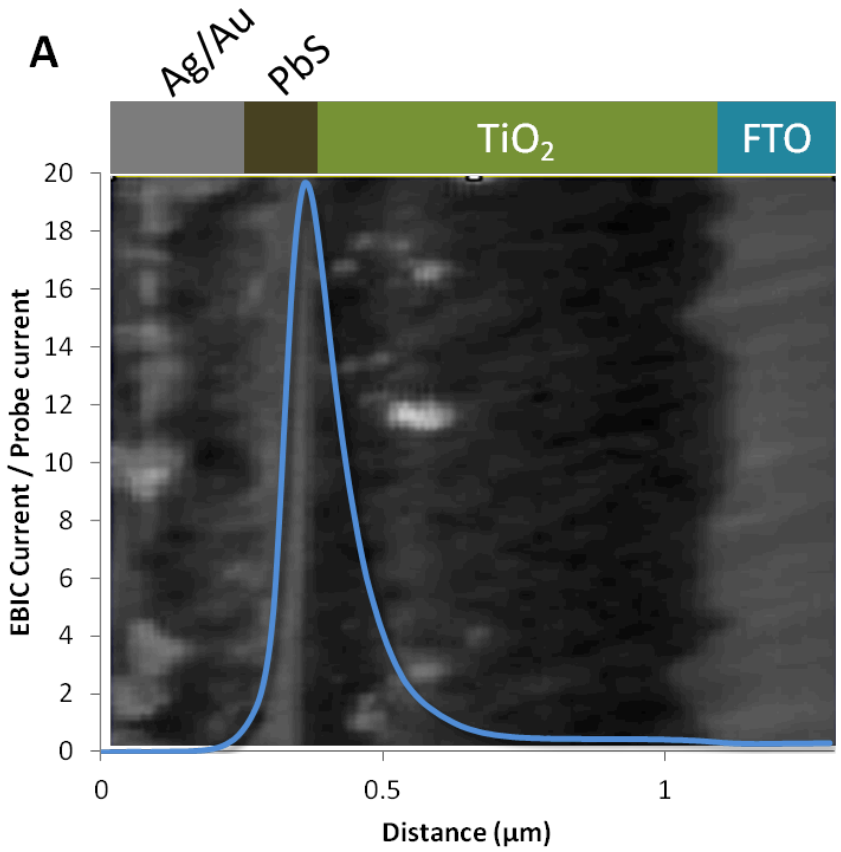

Figure 4.6: A sample EBIC trace (blue) for a prototype PbS DH-CQD PV, overlaid on an image showing the corresponding device being tested. The identity of the layers is shown above the EBIC curve. Peak EBIC current occurs slightly to the left of the p-n junction, inside the PbS layer, and decays quickly towards the Au cathode. Signal decays more slowly in the TiO_2 layer for reasons that will be discussed in later sections, and it completely lost within the FTO electrode.

An undesired effect of note pertaining to EBIC is the difference in total energy of an electron in an SEM beam traveling through a high potential gradient compared to even the most energetic photon emitted from the sun. The current generation per given volume in any solar cell under irradiation of an electron microscope beam is therefore extreme

compared to sunlight—indeed, a single incident electron can excite on the order of 10^3 electron hole pairs through inelastic scattering and secondary electron processes. Furthermore, the scattering volume for secondary electrons within a given layer can have radii of well over 100 nm, as can be seen in the Monte Carlo simulations in Figure 4.7. This scattering volume is the reason for the observation that peak current productions tend to lie slightly (~40 nm) into the active layer away from the p-n heterojunction. At this point within the active layer, a large portion of the electron-hole pairs generated—or, similarly, the majority of the scattering volume—are contained within the PbS active layer, as opposed to the case in which the beam is centered upon the p-n junction and a large portion of the interaction volume is centered in the TiO_2 layer.

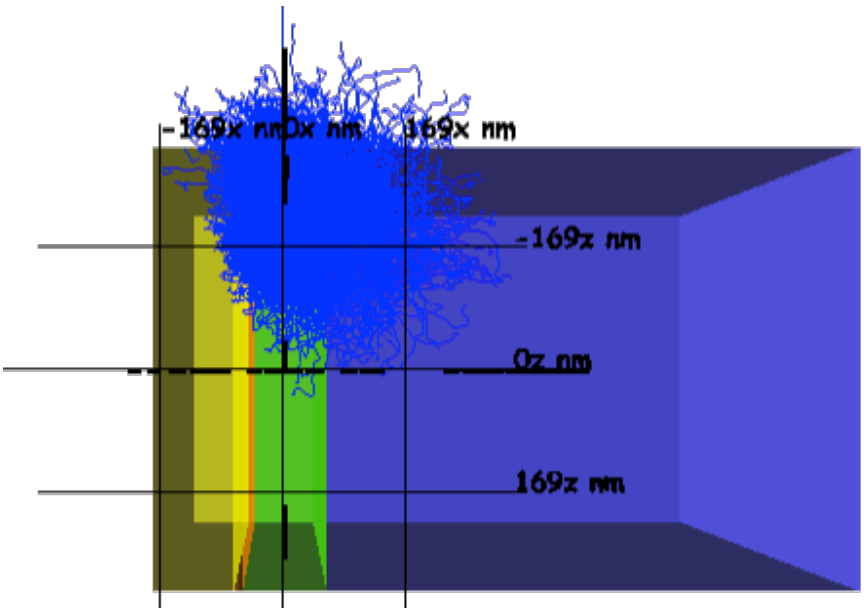

Figure 4.7: Monte Carlo simulation of simple heterojunction PV device, employing Si as the absorber layer for simplicity, in order to show normal secondary electron generation volume. Incident electron beams not only generate considerable amounts of current, but indeed create that current in some cases rather far from the spot of excitation.

4.3 Visualizing Effects of Polydispersity

This project encompasses the investigation of two general concepts pertaining to DH-CQD PVs, devices that are rendered relatively difficult to model due to hopping-based charge transport and extremely high trap densities, among other reasons. The first of these two device topics is geared towards visualizing the effect of QD size polydispersity in active layer thin films. This effect has been discussed in previous literature which showed through AM 1.5 illumination device measurements that shallow electronic traps formed from increasing amounts of low band gap QD inclusions results in significant losses in open-circuit voltage (V_{OC}) by lowering the electron quasi Fermi level.[127] We sought to visualize the effect this polydispersity has on the current propagation in these same PbS QD films: how does the inclusion of shallow traps effect the current production profile in the absorber layer? Is current decreased evenly throughout the entire active layer, or can shallow traps be largely overcome in regions of heavy depletion?

Three device cross sections were studied with EBIC, differing only in their active layer composition: (1) "pristine" layer composed of E_g=1.3 eV PbS QDs only: (2) 5% b.v. E_g=0.85 eV doped film: (3) 20% b.v. E_g=0.85 eV doped film. In all three devices, the PbS layer was kept very thin in order to absolutely ensure total space-charge depletion in the active layer. In this way, all electron hole pairs (EHPs) formed in the PbS travel under the influence of an electric field, nullifying the need for diffusion current, and allowing us to judge losses in current ideally based solely upon shallow trap recombination.

For the pristine device, the peak onset begins near the Au/PbS interface, extending with maximum signal roughly 40-30 nm into the PbS layer from the PbS/TiO_2 junction

followed by gradual decay into the TiO_2. Peak current production occurs near the p-n junction due to the short distance minority carriers (electrons) must travel to reach the TiO_2 electrode. In the case of non-pristine devices of 5% b.v. inclusion of low E_g QDs, the measured macroscale PV parameters (Table 4.1, Figure 4.9) were—while experimentally significant (ca. 11% deviations in both V_{OC} and J_{SC})—not profound enough to be definitively witnessed in EBIC traces.

With 20% b.v. of the same low E_g QDs, the pronounced effect of minority carrier trapping is obvious in both the EBIC signal traces as well as the current-voltage characterization (Figure 4.8). These average line profiles of the EBIC maps indicate maximum current generation and collection is near the device p-n junction; however, with the more defected device, the onset of collection is more spatially delayed than the pristine device. This is, to be clear, not to say that EHPs aren't being formed within the region of the active layer near the Au, but rather that those electrons that *are* being excited (presumably the same amount as in the pristine and 5% defect devices) are generally unable to travel the width of the PbS layer without succumbing to the potential wells that stem from the high density of defects. The hole mobility, on the other hand, is maintained throughout the three devices as indicated by optimum current production values within the region in which majority hole carriers have the farthest to travel to recombine in the gold electrode. This can be explained by the stasis of the valence band value with respect to vacuum under changes in quantum confinement energy in PbS QDs.[128] Furthermore, while the current values taken from the EBIC measurements can not be used quantitatively in and of themselves, it is telling to notice that the trend in current production for the graph in Figure 4.8 mimics that of the bulk characteristics of

the devices tested under illumination. Namely, that both the J_{SC} values and the peak EBIC current values are roughly 2:1 for the pristine:20% defected devices.

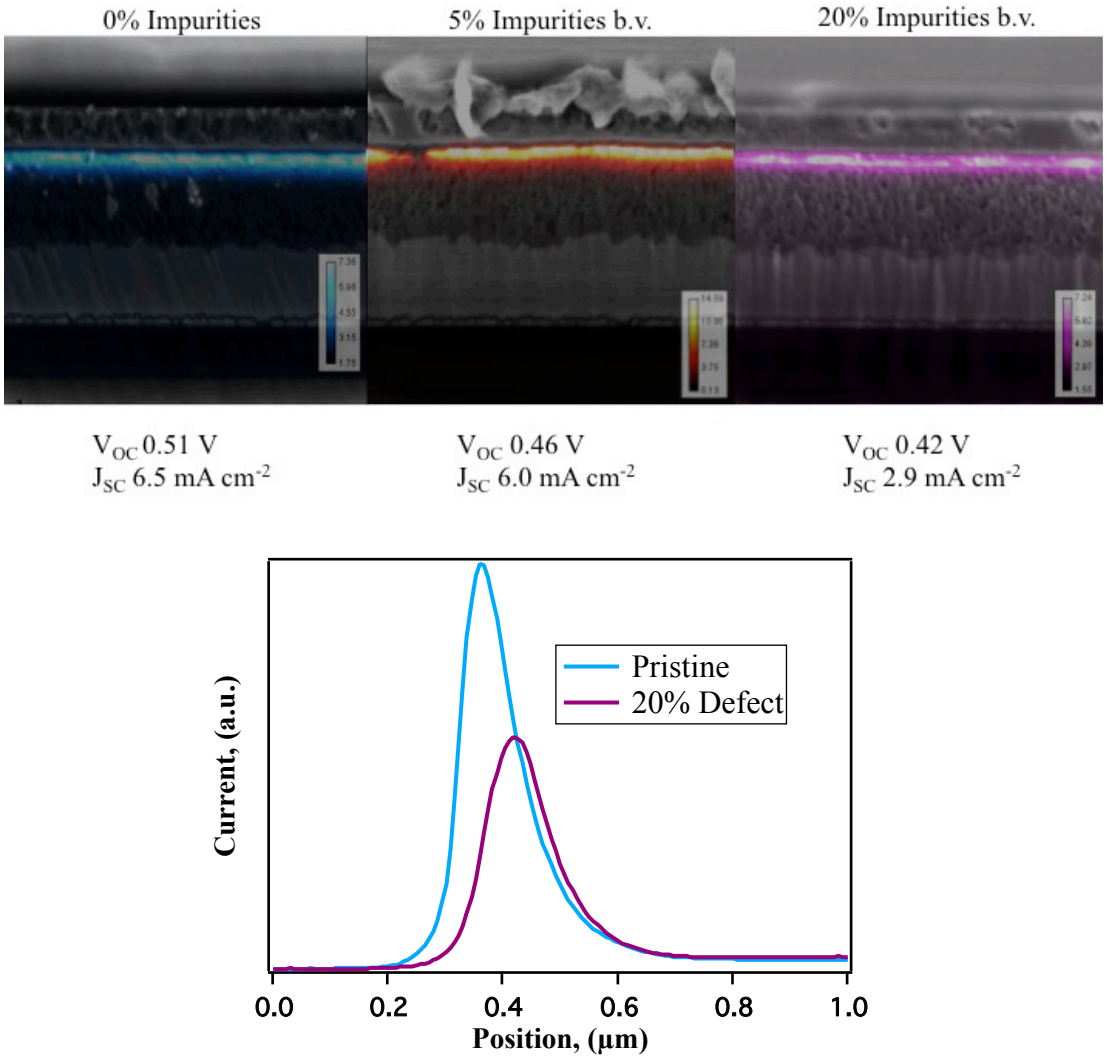

Figure 4.8: (top) EBIC maps of devices containing varying defect densities with corresponding V_{OC} and J_{SC} values. Upon close inspection it is possible to see that the spatial extent and strength of the highly defective device is slightly less than that of the pristine device. More tellingly, the curves below show the onset of current production on a normalized x-axis (the Au/PbS interface is at 0.2 micrometers on the x-axis for both curves). Aside from a depleted signal, onset begins further from the Au/QD interface in the defected device that represents the inability of excited electrons to reach the TiO_2 if exposed to high trap density.

4.4 Corroboration of Electrical Engineering Estimations with EBIC Data

4.4.1 Considerations for Device Optimization

As previously mentioned, perhaps the single largest difficulty faced by researchers attempting to optimize these devices is the comparatively extremely low lifetime of charge carriers in QD thin films. The high density of recombination centers in the form of not only the aforementioned shallow traps stemming from size dispersity, but also deep chemical traps on the surfaces of QDs in the form of nonradiative recombination centers such as dangling bonds, renders excited charges highly susceptible to parasitic pathways that detract from both current production and maximum active layer thickness. This limit on thickness in turn detrimentally affects the total achievable absorption of the PbS layer and diminishes their current applicability in industry.

More specifically, the practical thickness of a CQD device is limited to roughly the sum distance of the depletion region and diffusion length. This diffusion length for CQD solids is estimated to 10-100 nm.[46] The dopant density for MPA-capped PbS QDs has been calculated with Mott-Schottky analysis to be roughly $p \approx 2 \times 10^{16}$ cm^{-3},[121] and literature dopant values for TiO_2 mesoporous films start at $n \approx 1 \times 10^{16}$ cm^{-3}.[129-131] When taking in to account the estimation of ~250 nm for the depletion region inside the PbS active layer resulting from the heterojunction of the similarly-doped PbS-TiO_2 layers,[46,132] the current limit for active layer thickness in MPA-capped PbS DH-CQD PVs is roughly 300 nm—less than a third of the 1 μm thickness that would be required for complete absorption.[133,134] And so, the issue of optimization—the goal of reaching beyond the 10 and 15% efficiency rating—is one based in both chemistry and electrical engineering. Chemists strive to better "seal up" the surface, as it were; to block off the

non-radiative deep trap pathways that are inherent in all QD samples. Electrical engineers strive to circumvent the inevitable fact that these defects do and will certainly exist to some extent, while retaining the material properties that render QDs such attractive candidates for solar cell absorber layers in the first place.

Recently, a comprehensive study was performed outlining the resultant properties of differing chemical treatments on PbS QDs that stands as a testament to the sheer adaptability of the material and beckons for application of a method such as EBIC.[135] In the report, Voznyy, et al., used field effect transistors (FETs) to determine the effect of simple chemical treatments on PbS QD samples and found not only was the dopant density was effectively tunable over several orders of magnitude (~10^{14}-10^{18} cm^{-3}), *but that they were tunable over several order of magnitude as both* p-*type and* n-*type materials*. This intricate tunability led to devices that were able to harness a PbS QD p-n homojunction and ideally extend the depletion region further than possible in the TiO_2 heterojunction architecture.[136] However, performance enhancements were not as dramatic as hypothesized and were only witnessed through modest improvements in V_{OC} and FF. When studies such as this, in a field that constantly emerges and evolves like that of QD PVs, fail to produce as planned, techniques like EBIC provide an invaluable piece of the puzzle en route to optimization.

This section serves to exhibit the ability of EBIC to directly image effective charge carrier collection domains. As the first study of its kind, it is anticipated that the findings herein can be extended to myriad experimental devices to determine paths forward for optimization based upon experimental determination of their true inner workings.

Table 4.1 PbS DH-CQD Device Electrical Characterization

Device	PbS avg thickness (nm)	TiO_2 avg thickness (nm)	η (%)	V_{OC} (V)	J_{SC} (mA/ cm^2)	Fill Factor FF	Shunt R_s (Ω)	Series R_{sh} (kΩ)
Pristine	70	640	1.3	0.51	6.5	0.43	350.3	3.36
5% defects	100	750	1.2	0.46	6.0	0.42	356.4	2.45
20% defects	85	600	0.56	0.42	2.9	0.45	705.1	6.13
Thinnest	120	350	1.1	0.51	6.9	0.32	490.7	1.45
Average	230	310	1.5	0.53	9.7	0.29	438.0	1.46
Thickest	430	330	0.84	0.49	6.1	0.28	783.7	1.67

4.4.2 Imaging the Charge Collection Region in a PbS Active Layer

At this point, we focus on the modulation of PbS film thickness with the goal of setting a precedent for the imaging of current collection profiles correlated to *ab intio* predictions and device design. Monodisperse samples of E_g = 1.3 eV PbS quantum dots were used to construct PVs in the same manner as those described in section *4.4.1*. Three devices were assembled, composing active layer thicknesses of ~100, 200 and 400 nm. As previously mentioned, we expect that, due to the estimation of ~250 nm depletion region and short diffusion lengths, charge collection should not occur at distances roughly >300 nm.

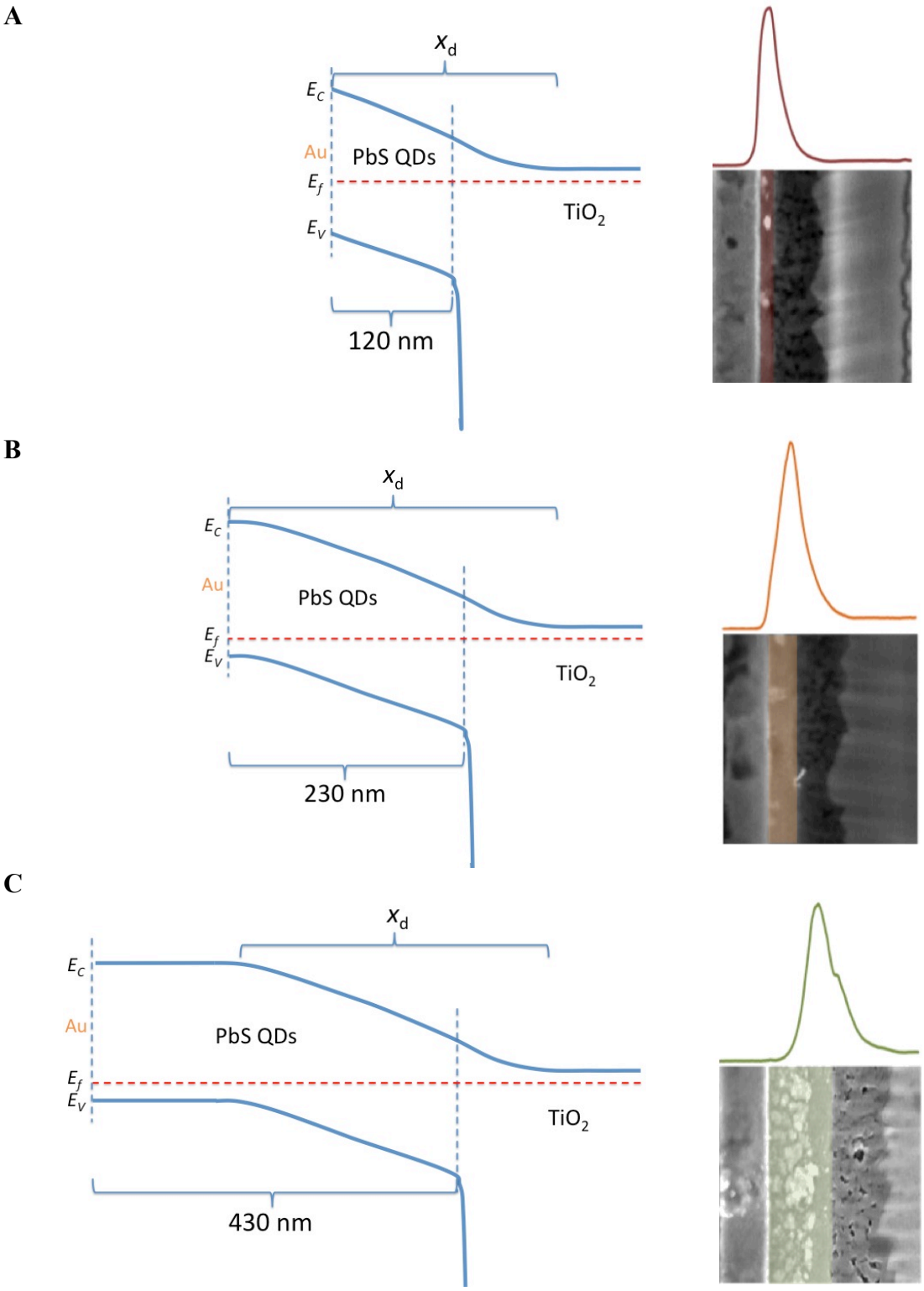

Figure 4.9: (A-C) Band diagrams are correlated to device cross sections with EBIC traces. PbS QD active layers are highlighted in colors matching their EBIC profiles. The

bright white layer to the left of each PbS layer is the Au electrode, and immediately to the right of each color-coordinated PbS layer are the TiO_2 electrodes, spatially mimicking the band diagrams to the left.

Figure 4.9 shows the EBIC profiles for these three devices as well as their corresponding band diagrams and electrical parameters displayed in Table 4.1. Firstly, the best performing device was found to be one with a ~200 nm thick active layer. In this device, the spatial extent of current collection is pushed near its hypothetical limit of 250 nm. This assertion is represented in the corresponding band diagram shown in Figure 4.9B, in which the electric field generated within the active layer depletion region can be seen to begin flat-banding as the active layer approaches the Au electrode. As can be seen in the EBIC trace and corresponding cross section, the peak current production occurs nearest the p-n junction and decreases throughout the active layer (highlighted in orange) towards the Au, as is expected. As a note, for all these devices, the baseline "zero" level can be seen in the thick Ag electrode layer to the far left of each EBIC curve. Furthermore, one can observe the effect of beam scattering, which was mentioned in the section concerning Figure 4.7, at the Au-PbS interface in the small amount of current generated within the bright Au layer in the 100 and 200 nm devices. This result is in fact not an artifact, but rather a result of secondary electrons being generated *within* the PbS layer during excitation of the Au or Ag layer. The rapid spatial decay of current production at the PbS/Au interface indicates that the density of the excitatory beam-generated electrons in the film decays quickly away from the original excitation location.

The 100 nm-thick device exhibits lower efficiency and J_{SC} values than the 200 nm device due simply to less overall light absorption stemming from less material in the active layer. However, as can be seen in Figure 4.9A, the entire width of the active layer in the 100 nm device, highlighted in red, produces current. Electron-hole pairs formed near the back of the device (at the Au-PbS interface) are able to dissociate under the influence of the built in field in the depletion region and be swept efficiently to corresponding electrodes, just like in the 200 nm device. Indeed there is not much of note in the EBIC analysis of this device as it functions nearly identically to the device twice its thickness.

The 400 nm thick device lends definitive evidence to the ~300 collection distance limit mentioned at the beginning of this section. The band diagram for this device exhibits a ~150 nm flat-band potential region in the PbS QD layer as it approaches the Au interface and charge depletion in the active layer ceases to be. The band diagram is mimicked remarkably well in the corresponding EBIC data for the 400 nm device. Current production tails off to baseline roughly 150 nm from the Au-PbS interface, indicating the inability of electron-hole pairs to be separated in the absence of an electric field and the propensity for recombination therein. As seen in Table 1, the 400 nm device suffers from poor performance compared to the 200 nm device, however these decreases result from different reasons than those mentioned in the 100 nm device. In fact, in all likelihood more light is absorbed in the thickest device, however two detrimental processes are at work in this instance: (1) more light is wasted in the thickest film due to absorption deep in the active layer of the device (towards the Au) which results in charge recombination due to ineffective carrier separation, and (2) decreased majority carrier

(hole) effective collection efficiency once holes enter the flat-band portion of the active layer en route to the Au cathode. The elimination of these effects depends on interplay between extending diffusion lengths in QD solids and widening the active layer depletion region.

4.5 STEM-EDS Cross Sectional Mapping

Throughout the process of performing EBIC on PbS CQD devices, there was a persistent and unexpected attribute of the current profiles. Upon inspection of the current vs. position curves in figures 4.8 and 4.9 it seemed as though an inexplicable amount of current production was occurring hundreds of nanometers from the p-n junction within the TiO_2 layer. When speculating on the basis for this current, one could assert that when inspecting the band diagram of the device, there is technically no reason the TiO_2 would be prohibited from acting as an active layer. Under the solar spectrum, TiO_2 acts as a wide-band gap (3.2 eV) transparent window absorbing a negligible amount of light, however the electrons in high voltage electron beam impart many times more energy upon the device than 3.2 eV. Therefore, we constructed a TiO_2-only Schottky junction cell that consisted simply of the exact same PbS DH-CQD device in the EBIC studies above, only totally lacking the QD layer. In this device a Shottky junction exists at the TiO_2-FTO interface, as can be seen in the EBIC profile in Figure 4.10. The fact that TiO_2 is indeed EBIC active should not be taken to indicate that it is responsible for the current seen within the layer in the PbS DH-CQD devices. Indeed, the extent to which TiO_2 is able to generate current under an electron beam is extremely low and was generally found

to compete with the noise level of the current amplifier in the EBIC testing setup (Figure 4.10B, inset). It was determined that although the TiO_2 is capable of generating an EBIC signal, the current generated is simply totally negligible compared to the current produced near the p-n junction in the PbS layer which completely overwhelms the baseline and would clearly overwhelm any signal from TiO_2 in both spatial extent and sheer magnitude.

A

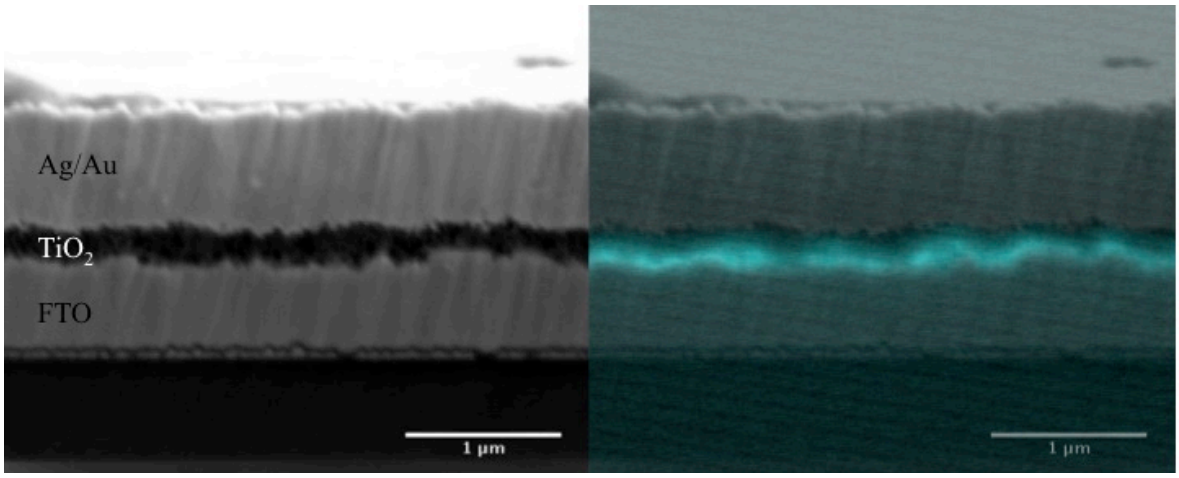

B

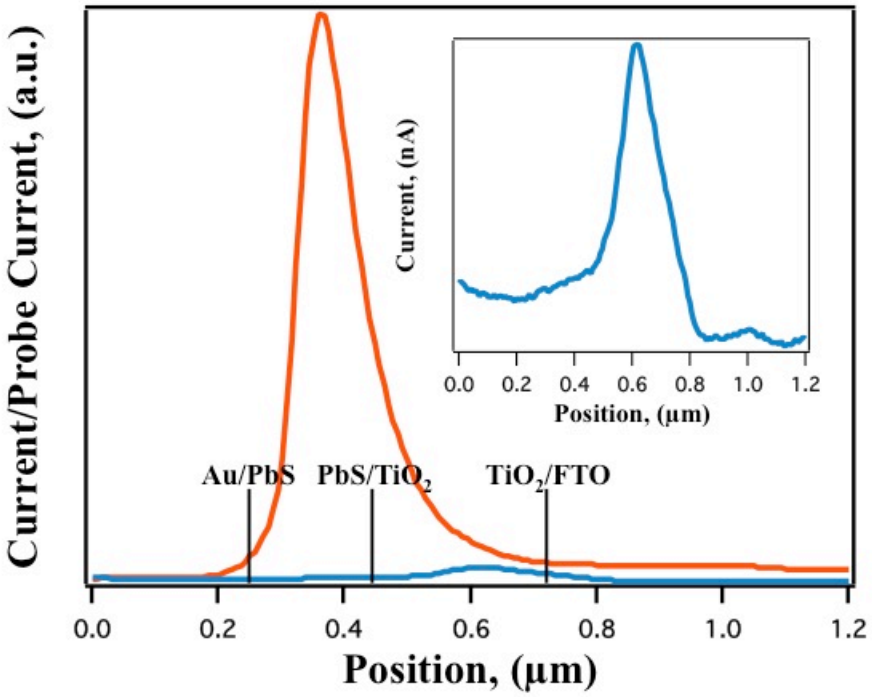

Figure 4.10: (A) Cross section without (left) and with (right) EBIC map overlay showing current production in TiO_2-only device. Very little current was produced, which can be visualized in the high background in the overlay, and qualitatively explained in the fact that in order to visualize any current production above baseline, a 480 pA beam current was needed (roughly 20x that needed in PbS QD devices). (B) Graph showing beam

current-normalized EBIC traces of typical PbS QD-based device (orange) compared to signal from TiO_2 (blue). Inset shows profile of raw TiO_2 current production peak. TiO_2-based current production cannot account for the extensive current seen throughout the oxide layer, and is now explained by extensive QD penetration into the TiO_2.

4.5.1 Penetration of Quantum Dots into TiO_2 Layer

STEM-EDS imaging of device cross sections exposed an unexpected finding in the chemical makeup of the mesoporous TiO_2 layer. It was found that Pb and S x-ray signal originated hundreds of nanometers into the TiO_2, away from the QD film-TiO_2 bulk junction. While it was expected that a certain level of penetration would occur in the upper portion of the oxide layer, penetration of QDs was not expected to reach much past ~50 nm, an expectation which is commonly mirrored in device schematics of DH-CQD PVs which tend to depict these interfaces as rather distinct junctions.[110,121,126] In the STEM-EDS images shown in Figures 4.11 and 4.12 PbS QDs can be detected as far down as the compact TiO_2 layer formed during the first $TiCl_4$ treatment in the preparation of the electrode at the TiO_2/FTO interface. We hypothesize that QDs are able to intercalate into small passages in the TiO_2, forming interconnected paths of QDs, much like a sponge soaked with water.

This finding is taken to be accountable for the considerable and gradually declining amount of current produced within the TiO_2 layer. Current decreases both as the density of active absorber lowers at the transition between the QD thin film and TiO_2 layer and as the ability of holes to travel the full distance back to the Au cathode becomes negligible. This layer mixing clearly leads to a less distinct interface, and with this

understanding, the entirety of the TiO_2 film resembles a sort of sparse bulk heterojunction, which has been explored in these devices in the past by installing TiO_2 pillars throughout the PbS QD active layer.[137-139 140]

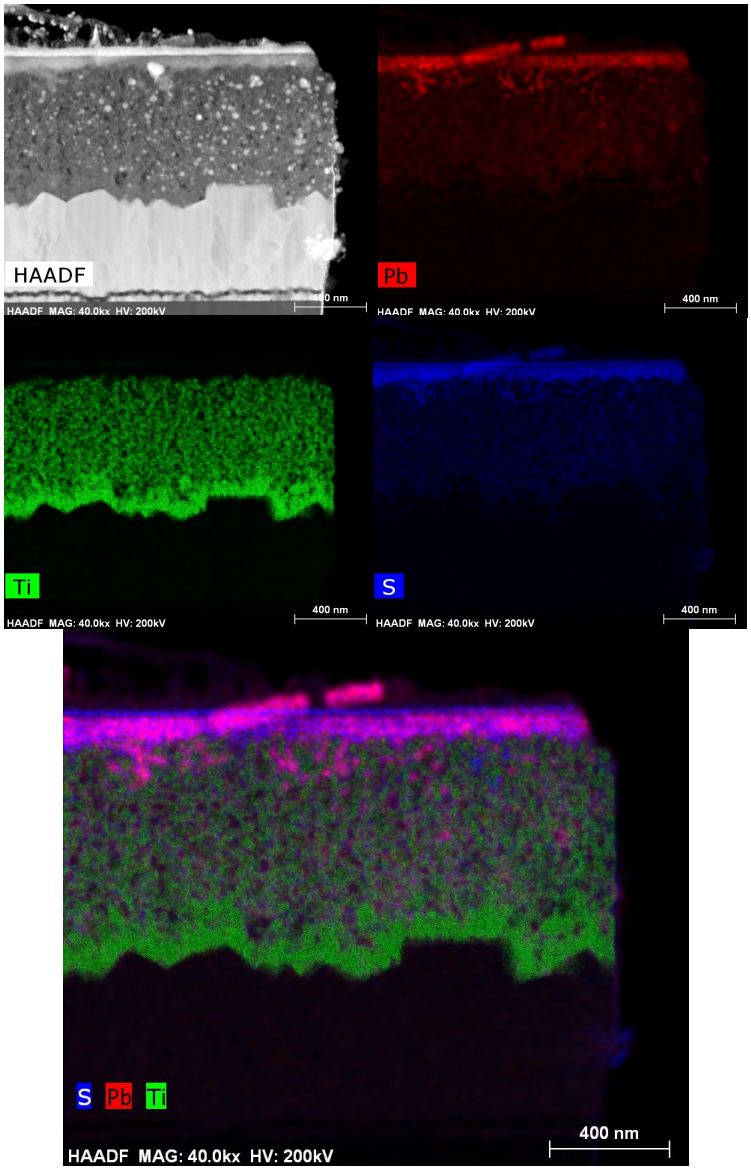

Figure 4.11: Cross sectional STEM-EDS images of PbS active layers atop TiO_2 layers. Pb signal is shown in red, penetration is obvious both in the Pb-only image in the upper

right, but also in the elemental overlay image below in which purple PbS is seen dispersed throughout pockets within the pores of the TiO_2 layer.

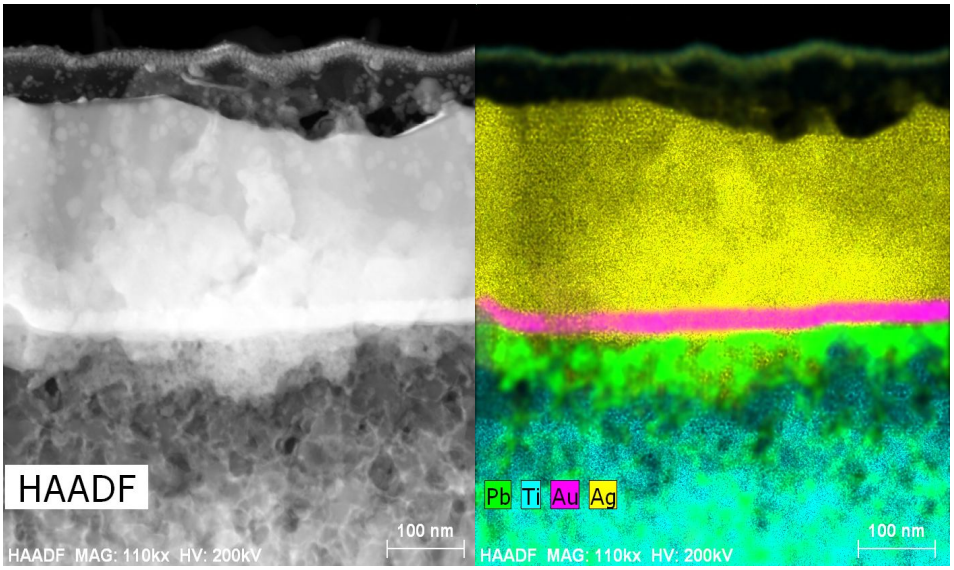

Figure 4.12: Additional STEM-EDS elemental mapping showing close up of green Pb signal trailing though pores of the TiO_2 layer. Capillary action is thought to pull QDs into the pores of the oxide hundreds of nanometers towards the FTO contact, an unexpected finding that has strong implications on current production and the understanding of band structure both at the p-n junction as well as within the active layer.

4.5.2 Implications on Electrical Modeling

The central question that is inherent in this realization revolves around its implications toward the way in which one is to understand the band structure dynamics of a system wherein, rather than a distinct heterojunction, the p-n interface is diffused over several hundred nanometers. Given that the electric field generated within a PV is a result of carrier exchange equilibration process at the p-n junction, how does the spatial extent of band banding within the PbS QD bulk layer change when a significant portion of the

TiO_2 charge exchange occurs within QDs lying inside the oxide? In other words, does the TiO_2 effectively become partially depleted by the QDs within its pores, thereby decreasing the amount of holes injected from the QD thin film and limiting the extent of the electric field in the active layer?

At this time, the methods needed for modeling studies to probe these questions are not at the disposal of this study. However, further EBIC-STEM-EDS correlative studies in which compact TiO_2 layer-based electrodes are compared to the norm should shed light on the effect of this QD intercalation.

Chapter V.

DEVELOPMENT AND IMPLEMENTATION OF SOLAR CELL FIELD TRIPS FOR RURAL AND INNER CITY HIGH SCHOOLS

5.1 Introduction

Often times, there exists a fundamental disconnect between canonized textbook science and the scientific process of experimentation and discovery. Pre-collegiate students are taught—necessarily and rightfully so—the laws of nature, the theories and mathematics explaining them and, ideally, the rationality and consistency of the scientific method. However, generally speaking, high school students, especially those in predominately rural settings, rarely get the chance to experience the cutting edge. Laboratory exercises at the high school level assist in visualizing the diffraction of light and acid-base reactions while introducing students to common techniques and equipment, but they rarely relate directly to current global topics or innovation. The job of a research scientist can be seen as esoteric and impossibly remote to students whom have little if any exposure to scientific discussion beyond those found in popular media outlets. This leads to a state of bewilderment in pre-collegiate students in which they perceive some insurmountable difficulty in dedicating to a hard science for their future occupation. Alleviating this bewilderment is critical to the development of students that are enthused towards much-needed careers in Science, Technology, Engineering and Mathematics (STEM) fields.

With this is mind we have developed an alternative energy-based hands-on field trip program at a bustling research setting. Vanderbilt University is a Tier 1 research institution located in a large metropolitan area surrounded by an extensive network of

rural communities in Middle Tennessee. These field trips prove time and time again to be extremely beneficial in fostering enthusiasm and removing the aforementioned stigma that may exist in high school students with respect to STEM careers. And, by incorporating instruction, experimentation and friendly competition, the participating students are constantly engaged in discussions to which they simply do not have the means in their normal academic settings.

5.2 Field Trip Overview

5.2.1. Scheduling and Preparation

Scheduling of the field trips was essentially a matter of casting a wide net of the entire middle Tennessee region. Public schools across this are were contacted and notified of the opportunity and possible dates.

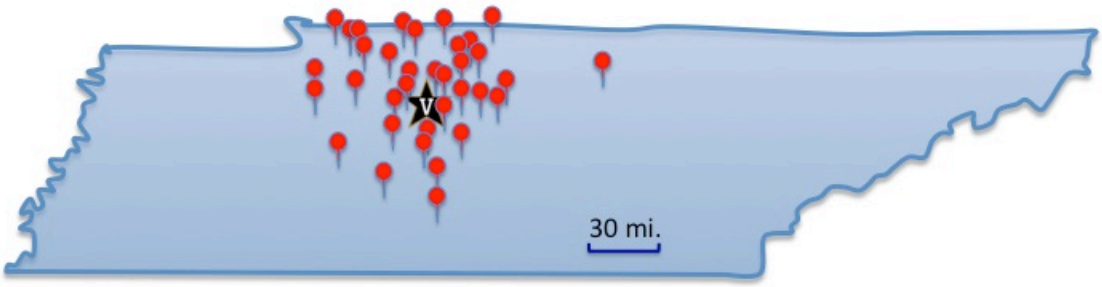

Figure 5.1: Map of Tennessee with red pins showing the positions of regional public high schools that were participants in the outreach fieldtrips.

The main form of preparation needed prior to the field trips revolves around the cleaning and construction of the FTO-TiO_2 electrodes. One of the most important logistical discoveries we made in learning to carryout these expansive field trips is the

need for both streamlined experimental portions as well as high output of materials with relative ease. Generally speaking, screen-printing or doctor blading are used to form thick TiO_2 layer on for usage in dye-sensitized solar cells at the time of assembling the devices. However, with the time restraints inherent in these public school field trips, it was found that pre-preparation of these electrodes was absolutely necessary. Furthermore, doctor blading was simply too time intensive and finicky to achieve the amount of electrodes needed for the students we found ourselves serving. It was determined that the most efficient method for the preparation of these electrodes was based upon spin coating of TiO_2 paste to form relatively thin yet still functional layers which could be sintered at once en masse in a tube furnace. The paste is made in house from simple and innocuous chemicals and was identical to the procedure described on page 49, Chapter 3 of this document. The FTO electrodes were given quick 10-minute sonication periods in Triton X-100 and rinsed with ethanol. The TiO_2 paste was dilute 3:1 in ethanol, and the substrates were spun on a spin coater at 2500 RPM for 25 seconds after being fully coated with the paste. These electrodes were then annealed at 500 °C for on hour to form robust layers. An equal amount of pure cleaned FTO slides were prepared for use as graphite-coated counter electrodes in the solar cells.

5.2.2 Presentations and Discussions

Each field trip day begins with two preparatory presentations; a safety presentation from a Vanderbilt faculty member followed by a lesson that outlines general alternative energies information as well as an introduction to dye-sensitized solar cells (DSSCs). The safety lesson serves to introduce the high school students to the typical

personal protective equipment (PPE) expected to be worn in a research environment. It also stresses the importance of safety data sheets when working with any chemical whatsoever. Students are also informed of their daily agendas at this time and given a short survey from Vanderbilt for their contact information regarding undergraduate recruitment.

The scientific lesson is given by a graduate student volunteer who also serves as the trip leader and instructor for the remainder of the day (Supplemental Information). The lesson gives the instructor an opportunity to familiarize and humanize themselves to the visiting students. We find that more often than not, the visiting students expect the interaction between them and the instructor to be under the same guise as their relationship with their schoolteacher. However, the goals of arousing enthusiasm towards STEM careers and finding a deeper understanding of alternative energy pursuits befit a more casual rapport. The lesson first addresses the topic of global climate change—its causes and effects—as well as society's means to generating energy, from fossil fuels to nuclear to several types of alternative energies. The simplified mechanism of a *p*-*n* junction Si solar cell is introduced as a "classic" photovoltaic, and the emergence of the DSSC is described as an archetype for a topic of current innovation and research interest in engineering and nanoscience. Group leaders are encouraged to embellish on connections between their research and the topics being discussed on nanoscience and innovation.

5.2.3. Laboratory Portion

After the morning presentations session, the students are each given proper PPE (disposable lab coats, safety glass and nitrile gloves) and led into a freshman chemistry laboratory by the trip leader and a separate volunteer we find beneficial for the laboratory portion. The hands-on experimental portion of the day revolves around groups of 2-4 students assembling and testing DSSCs based on a classic device architecture reported by Smestad and Grätzel[38]. Each group is asked to choose their own laboratory station equipped with the proper glassware and equipment needed to carry out the assembly of their devices. We find it beneficial if at this time the trip leader introduces the students to the different scientific equipment in the lab and explains to them that the team that manages to build the device producing the highest current output will receive commemorative t-shirts. A sense of competition tends to inject enthusiasm and fun into the laboratory session, of which many students have preconceived notions of arduousness. The students are given experimental procedures and asked to follow them as closely as possible. These detailed experimental procedures can are adopted from previous reports and can be furnished upon request. The devices consist of four main layers that the students are asked to functionalize and assemble. Raspberries and blackberries are distributed to each group (4-6 each) and the students proceed to grind them with a mortar and pestle, solvating the extracted anthocyanin dye in ethanol and water. After grinding the berries for roughly 10 minutes, the student groups are introduced to water aspirator vacuum flask setups and Büchner funnels. It should be emphasized that each step of the experimental procedure is used not only as an education in the chemistry and physics of solar energy and DSSCs, but equally as an exercise in

exposure to chemistry lab equipment not typically available to many rural schools. Once the groups have fully filtered their berry pulp and acquired a sufficient amount of juice, each group receives a TiO_2-coated FTO electrode and a pure FTO electrode. While soaking the TiO_2 electrode in their juice, the students begin forming a graphite layer on their FTO counter electrode. This junction generally serves as a good place for a short and general lesson on redox reactions and electrochemistry. Once the TiO_2 electrode is rinsed and dried, the two electrodes are clipped together and the group leader helps apply the I^-/I_3^- electrolyte to the device while explaining the process of capillary action taking place.

The students are then asked to leave their devices at their workbenches and are escorted back to the morning classroom. Each group is asked to decide upon their own humorous or creative team name and write it on a chalkboard. The groups are taken one at a time into the lab where the lights are dimmed and the devices are attached with alligator clips to a multimeter set to read current. The group leader holds the device under a solar simulator light source, while the group is asked to observe the multimeter for the maximum current value that can be produced. After each group tests their device, the group with highest current output is announced, and the t-shirt prizes are handed out.

5.2.4. Microscopy Tour

After having lunch in the undergraduate cafeteria, which generally seems to excite high school students, they are escorted by the group leader to an electron microscopy lab on campus. In this particular microscopy lab there are two separate scanning electron microscopes (SEM), which helps allow each student to have full view of the

demonstration. One faculty member is stationed at each of the SEMs and the students are asked to spread between the two, at which point they receive a lesson on the workings of electron microscopy and the length scales which they are able to image by relating them to everyday objects such as the width of a human hair. Prior to their arrival, the faculty members have loaded and focused upon identical TiO_2 electrodes as those that the students have just recently used in assembling their solar cells. After demonstrating the process of operating the microscopes and imaging the electrodes, the students are given the opportunity to drive the sample stage and use the SEM themselves. It is explained to the students both orally and through a custom binder of microscopy data ranging from optical bright field to single molecule scanning tunneling microscopy (STM) images, that they are actively imaging features that are roughly $1/100{,}000^{th}$ the width of a human hair.

5.3 Outreach Statistics and Conclusions

Over the first 3 years of these solar cell field trips we have witnessed immense success. There have been numerous news stories and media attention surrounding the enthusiasm from both the students involved as well as the public school administrators for the opportunity to expose these students to true research labs at a large university such as Vanderbilt. Through these trips we have been able to reach 837 students from 36 schools in 15 different counties, with hundred more to come in the spring of 2015. We feel the potential for this invaluable type of outreach strategy to be applied elsewhere is simply a matter of effort and willingness of the graduate students and administrators involved.

Chapter VI.

CONCLUSIONS AND FUTURE DIRECTIONS

With respect to the plasmonic $Cu_xIn_yS_2$ QDs, it seems clear that the novelty of this synthetic route, namely the surfactant and solvent species, plays a significant role in the realization of LSPRs. Whereas past reports of copper chalcogenides can attribute their NIR absorption to copper vacancies formed upon exposure to oxygen, the LSPRs reported herein seem to stem from a different phenomena. These QDs are synthesized under an inert atmosphere, and not only does their absorption spectra contain LSPR resonance immediately following synthesis, but the relative intensity and shape of their LSPR peak changes only marginally over time (measured up to two months after original synthesis). Additionally, no such copper vacancy formation is observed for CIS QDs synthesized according to the method developed by Klimov, et al.[15], which utilizes the identical surfactant species as the $Cu_{2-x}S$ QDs characterized recently by Alivisatos and coworkers[26] (assuming 1-dodecanethiol acts as the main surfactant species in this synthesis). Very recently, this assertion was corroborated with experimental findings that show similarly that amine-capped Cu-In-S QDs are able to support plasmonic modes, while those capped with thiols seem to not be susceptible to vacancy formation.[141] This is likely due to reasons outlined in another recent finding by Toro, et al., which describes "crystal bound" ligand species that exist in the typical thiol-capped $CuInS_2$ synthesis.[93]

Aside from light harvesting, these QDs may find relevance in nonlinear optics and quantum information processing.[25] Further experimental elucidation of the specific electronic characteristics, including accurate dopant densities of these QDs is necessary for their meticulous application to technologies. To be certain, at this point, the presence

of LSPRs is preceded by the necessity of extremely high dopant values (approaching that of metallic behavior). This presents the difficult realization that these QDs are perhaps not well suited for thin film absorber applications; with such high N_h values, depletion regions in these layers would be negligibly thick, requiring charge carriers to diffuse through the active layer rather than drift under influence of a depletion field. As far as photovoltaics are concerned they could perhaps find usage as p^+-type windows in p-i-n junction systems, however it may be that their most exciting application lies in a technology that could take advantage of their stable LSPR-on-semiconductor properties.

It is the highly chemically adaptable properties of Cu-In-S-containing QDs that have facilitated the non-plasmonic "twin" (non-plasmonic-CIS) that acts as a crucial experimental control in the important findings outlined in Chapter 3. With the presence of plasmonic modes giving rise to a relative efficiency enhancement of 11.5%, this preliminary proof of principle experiment prompts the pursuit of experimental avenues not only for applicability to technologies (photocatalytics, non-linear optics, etc.), but perhaps to the clearer elucidation of the relatively under-studied and perhaps underutilized field of semiconductor plasmonics. Due to the straightforward root cause of the LSPR modes in these and other semiconductor NC species, it appears reasonable to propose the chemists' ability to translate this phenomenon to a variety of other crystal types.

One important project that begs to be performed is the engineering of a high-refractive index matrix for a dispersion of plasmonic-CIS QDs. Wide band gap semiconductor nanocrystalline species such as ZnS, HgS and GaAs are all high refractive (n) index materials which could be utilized to shift the LSPR peak towards the visible

region in plasmonic CIS QDs thereby increasing the plasmon-exciton overlap region shown in Figure 3.9. With a sensitivity of ~250 nm/RIU, a high *n* material such as GaAs (n = 3.9), one could expect an LSPR peak blue shift of ~625 nm compared its position with respect to tetrachloroethylene. This shift should be immediately apparent in UV-VIS-IR spectra of the thin films formed. Furthermore, the insulating properties of fatty surfactant species should shield the LSPR mode from decaying into the semiconductor background.

The EBIC study presented in this thesis opens many doors for future studies. Indeed, the work presented here essentially lays a foundation for an entire method of characterization on this emergent technology. The field of EBIC is, of course, obscured by the difficulty of the measurements involved in its data collection. First, the assembly of any photovoltaic whatsoever is a difficult and frustratingly finicky process, which, in this case, is exacerbated by the fact that the devices tend to be air-sensitive. Clearly, even after considerable strides in device optimization towards replicating literature efficiency values, I was never able to reach much past 2% IPCE values. These deficiencies lie essentially completely in the J_{SC} values obtained in my devices—the V_{OC} values were equal to or better than the majority of reports on DH-CQD PVs in the literature, suggesting that my devices were functioning electronically similarly to published devices with higher IPCE values. Series resistance is likely much higher in my devices compares to those produced in major labs (Sargent, Bawendi, Bulovic) due to processing parameters that could simply never be optimized in my graduate career. Still, I am very confident that, due to the matching of voltage and FF values, these devices serve as valid and direct comparisons to those that they reference in the literature.

Further, the process of obtaining EBIC data, while fairly streamlined at this point for this project, requires a very extensive learning curve. The sample preparation step alone for a single cross section takes several hours, and often times a small mistake will botch the entire measurement requiring a total restart.

The potential for correlative EBIC-chemical treatment studies is vast. As mentioned before, one of the most exciting attributes specific to QDs is the dopant tunability through simple surface treatments, allowing one to tune from p- to n-type within the same batch of QDs. Currently, studies utilizing this variability rely, predictably, on macro electrical characterization for the optimization of their devices. The ability to directly image sites of current production in these solar cells, which utilize complex and difficult-to-model architectures, is an ideal way of compiling steadfast evidence for areas in need of improvement or proliferation. The results obtained through my and Amy Ng's collaborative effort is primarily an important vindication of the purported lack of diffusion current production in these solar cells. As the community begins the push to QD thin films approaching the ~1 μm goal, this study has shown that EBIC can be used to elucidate the state of progress by identifying the on-set of current production within the active layer. For instance, if a project were to chemically engineer QDs to hypothetically have low deep trap densities leading to high mobility and diffusions lengths, the effectiveness of the chemical treatments could be judged by assembling PVs with 1 μm-thick QD layers and assessing their current production profiles in EBIC maps.

We also view the discovery of extensive QD penetration in the TiO_2 electrode to be an important piece of understanding in the overall geometry of these solar cells. As

described before, this intercalation could have profound effects on the total band structure of the devices, as the space charge region within the QD layer may be diminished due to charge exchange occurring within the TiO_2 itself, rather than at and beyond the bulk p-n interface. It would be interesting to assemble a similar device with a compact, rather than mesoporous TiO_2 layer.

Perhaps the most apropos conclusion to this thesis is one that acknowledges the underlying theme of most of the state of the art QD studies: as the synthesis and physical characterization of QDs has become further refined to the point of deep understanding, the proliferation of new applications and new tunability within QD applications has begun to take hold. In the years since I began my graduate career, a transition in the literature has occurred in which QDs, which were once being touted for their band gap tunability and solution-processability, are now being further tailored to the needs of multitudinous applications befitting a true mainstay in the realm of materials science. This realization is the true theme that developed as my graduate work began to take shape, and it was the nexus of all the work I performed—the exploration of boundaries that were once-unapproachable with materials that were recently nonexistent.

Appendix

A. Hall Effect Measurements

A.1 Background and Rationale

Over the course of my research concerning development and design of solid-state QDPVs, it has occurred to me that an often under-utilized aspect of research in the realm of materials chemistry is the electrical engineering approach. It seems appropriate to note that perhaps the most marked solid-state QDPV scientist today, Edward Sargent, is a professor of electrical engineering. Fittingly, it is imperative to the pursuit of intelligently designed devices that attempts are made to understand the systematic theoretical electronic structure of their constituent parts, as well as the device as a whole.

Knowledge of Fermi level positions relative to vacuum is arguably the most important factor in the band alignment design of a solid-state device. This, along with other parameters, such as depletion width, can be extrapolated from equations relating these values to measurable quantities like dopant type and density. The Hall effect measurement is an established and relatively straightforward method for accurately determining three main parameters of conductive and semiconductive thin films; dopant type, carrier concentration, and carrier mobility. These types of parameters are relatively under-studied in the field of QD research, and particularly QDPVs. Methods of measurement for electrical parameters of QDs in general include Mott-Schottky analysis via capacitance-voltage measurements on whole devices[121], scanning tunneling spectroscopy (STM) spectra[142], construction and characterization of QD field effect transistors[143], and Hall effect measurements.[144,145] Hall measurements are the most apt characterization method QDs due to ease of preparation and a readily accessible testing

apparatus. The development of a consistent method of thin film formation suitable for Hall effect measurements is a necessary step in the direction of electrical engineering-guided design of QDPVs.

A.2 Measurement Method

The Hall effect, or the established Hall voltage, is a direct consequence of a magnetic field's force exerted on moving charge carriers. A representative Hall voltage measurement is shown in Figure 5.

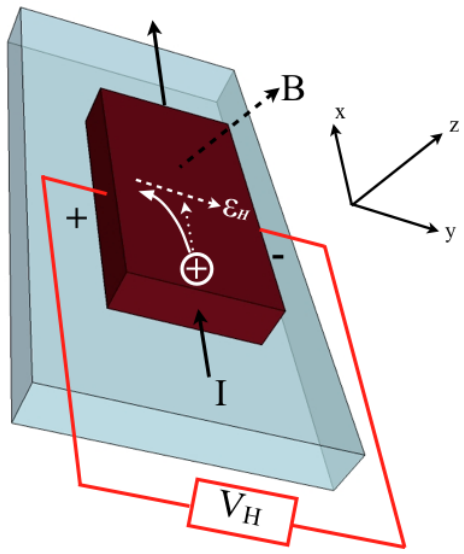

Figure A.1: Representative Hall voltage measurement apparatus. In this schematic, the dark red thin film is subjected to a known current (I) and a known external magnetic field (B). Carriers drift perpendicularly to the magnetic field, establishing a slight electric field, which is integrated across the width of the device to find the Hall voltage.

In Figure 5, the current carriers (travelling in the positive or negative *x*-direction if holes or electrons, respectively) experience a force perpendicular to both the current and the magnetic field. The deflection of charge carriers under this force in the negative *y*-direction establishes a charge imbalance that is spontaneously countered with an electric field, ε_H, in order to retain charge neutrality. Using Poisson's equation, integration of ε_H over the width of the device yields the Hall voltage, V_H. In its most fundamental measurement, a Hall effect device can be used to determine the dopant type (*n* or *p*) based upon the sign dependence of the Hall voltage on the charge carriers. Further, a so-called Hall coefficient can be calculated from experiment parameters as:

$$R_H = \frac{V_H}{J_x B}\frac{tL}{W} \tag{3}$$

where t, L and W are the height, length and width of the film, respectively, J_x is the applied current, and B is the applied magnetic field. From Equation 3, mobility, μ, and dopant density, *n* or *p*, can be deduced through the following relationship:

$$R_H = \frac{-1}{qn} = \mu\rho \tag{4}$$

where q the elementary charge and ρ is resistivity, which is equal to $R(A/l)$, where R is resistance and A and l are the cross sectional area and device length, respectively. Treating the entire device as a simple resistor, it becomes rather straightforward to determine the mobility. Additionally, for a *p*-type device, the sign of R_H will be reversed, therefore changing the sign of the "*-1"* in the numerator of (4).

A.3 Experimental Attempts

One of the difficulties in obtaining Hall voltages with QD samples lies in the device preparation. Macroscopic arrays of QDs must be obtained with defined areas that are reproducible and consistent. Colloidal suspensions complicate the task of forming such contacts; one is essentially left to choose between spin coating and drop casting as a method of QD deposition. QD ink printing is a separate option which has been pursued by other groups in the past, but this is beyond the resources of this project.[59] An ideal plan was devised for obtaining such substrates, which involves using adhesive tape as a device mold, with distinct area obtained through a rectangular hole punch (Figure 6).

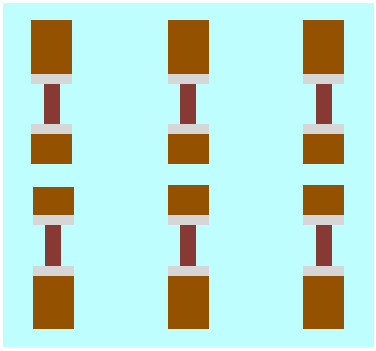

Figure A.2: Schematic of ideal Hall effect QD testing device showing glass substrate (blue), QD contacts (dark red), silver paint contact (silver) and copper tape for lead connections (brown).

In Figure 6, the brown copper tape contacts are used to ensure complete contact with the QD arrays, which is suspected to yield a more consistent current flow than simple point contacts. A magnetic field will be fluxed up through the device, and the Hall voltage will be read across its width.

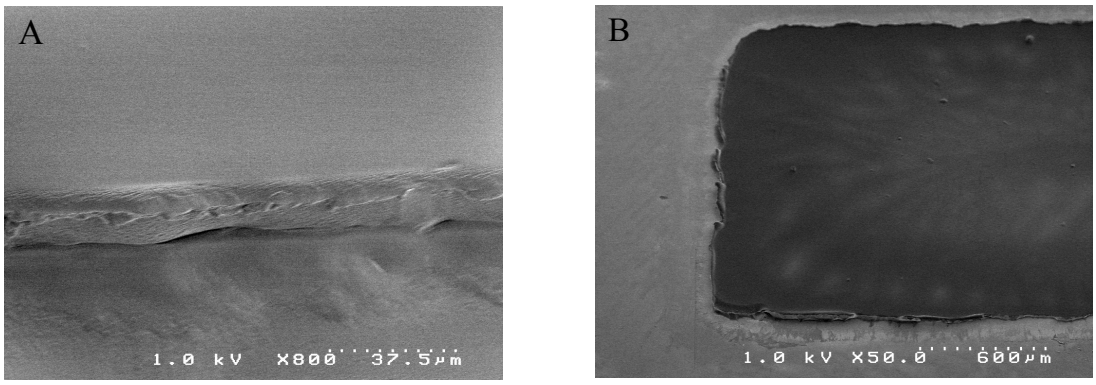

Figure A.3: SEM images of preliminary attempts at CIS QD Hall effect testing arrays. A cross sectional image of a film formed by two drops of QDs at 35 mg/mL (a), and a large-field image of one side of a single contact showing unevenness in contact thickness (b).

Initial attempts at device fabrication have proven unsuccessful in that the contacts seem to act as open circuits. This finding is unexpected due to the perceived high dopant density of the film, which should result is relatively reasonable conductance values. Figure 7a shows an SEM image of a representative contact formed by deposition of 2 drops of CIS QDs in toluene at a concentration of 35 mg/mL. The presence of two seemingly distinct layers, presumably from the two separate drops, is disconcerting as this may lead to defects in carrier transport within the film. Problematically, as QD concentration is increased with the prospect of gaining thicker films in a single drop, highly detrimental cracks begin to form within the contact. Figure 7b shows a contact formed with a single drop of 35 mg/mL QD solution. Although no cracks are observed, there are inconsistencies in the film thickness, as witnessed in the lighter and darker portions in the bulk of the contact. It is suspected that at a certain concentration of QDs

suspended in a solvent of specific vapor pressure will yield continuous and uniform contacts.

B. CYCLIC VOLTAMMETRY OF QD THIN FILMS

B.1. Past Reports and Goals

Cyclic voltammetry (CV) is an electrochemical technique in which a voltage is swept through a working electrode to preset endpoints in a continuous and cyclic manner. Redox potentials can be obtained by plotting working electrode current vs. applied voltage. Historically, CV has been extremely useful in the determination of electron transfer kinetics, the presence intermediate redox reactions, and the stability of reaction products, among many other applications.

There have been many reports on the usage of CV in determining the conduction and valence band energies with respect to vacuum in QD systems. With respect to QDs, researchers have correlated electronic and optical band gaps in CdS particles[146], determined conduction and valence band edges for band engineering in PbSe QD solar cells[122], visualized defect state energies[147], etc.[148-150] The purpose of the CV experiments I undertook was to obtain electronic energy level values for certain QDs our group was investigating, the values of which were not yet reported in the literature. As other studies have found, electronic band gap values can deviate from values determined through UV-VIS spectra as optical transitions, in one case by nearly 0.3 eV.[146] This is an energy amount that is crucial in the engineering of a PV, and can spell the difference between efficient charge injection and a flat band potential at a junction. Clearly, for material systems that have yet to be fully characterized, simple optical absorption peak values are not sufficient to accurately describe the electronic HOMO-LUMO transition in the QD.

B.2. Experimental

The CV experiments described in this section were performed on a potentiostat in the Cliffel laboratory. Platinum tipped working electrodes were polished before each use with the spinning wheel polisher with Al_2O_3 powder and rinsed thoroughly with DI H_2O. QDs were cleaned and dispersed to 50 mg/mL in octane. It was found that toluene and hexanes tended to evaporated so quickly that "coffee ring" formation resulted in very uneven layers on the working electrode. Deposition of the QDs onto the Pt tip simply consisted of a dropwise layer formation of QDs, allowing the solution to dry completely between each drop. The electrode can be held and tilted in order to ensure that the QDs form a continuous and fairly even layer over the Pt contact. This is repeated until the Pt metal is just barely coated to the point be invisible.

A measurement beaker is prepared in which the working electrode (connected to the green wire), the counter electrode (red wire) and reference electrode (Ag/AgCl, white wire) are submersed together in a 0.1 M solution of tetrabutylammonium perchlorate in acetonitrile with a mechanical stir bar. The software used was under the name "CHI66OA" with the option "T" to CV data. Scan polarity was set to positive, with initial value 0.0 V, swept to ±1.4 V with a step size of 0.05 V or less, and 2.5 sweeps. This process was performed several types of QDs as well as the bare Pt electrode over the course of several weeks, some of the results of which can be seen in the figures below.

B.3. Results and Corroboration with Reported Conduction Band Values

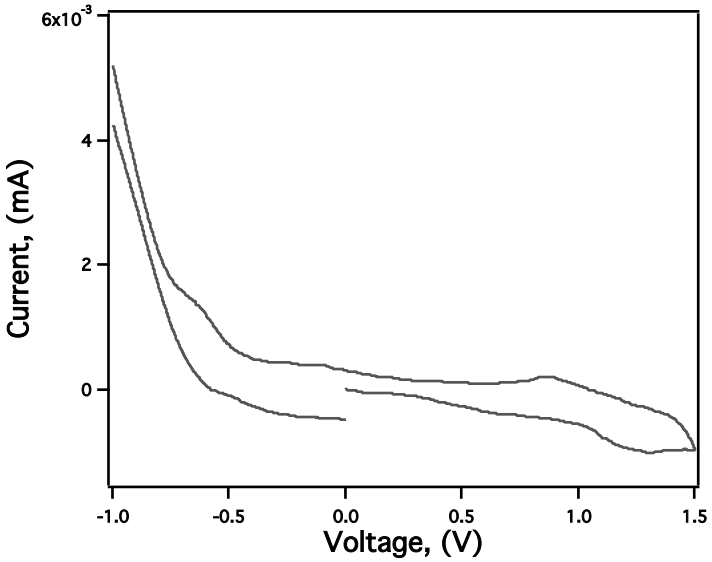

Figure B.1: CV curve of bare Pt working electrode in 0.1 M bath of tetrabutylammonium perchlorate.

The curve seen in Figure B.1 for the bare Pt electrode does indicate some redox activity in the form of bumps in the curve throughout the sweep, however it is difficult to use this data as a control because the current values are so much higher than those seen in the system when coated with QDs due to the inherent resistivity of QD films. Still, as will be shown in the data for QD sample, the analysis of the CV data correlates very well with published values on well-known systems.

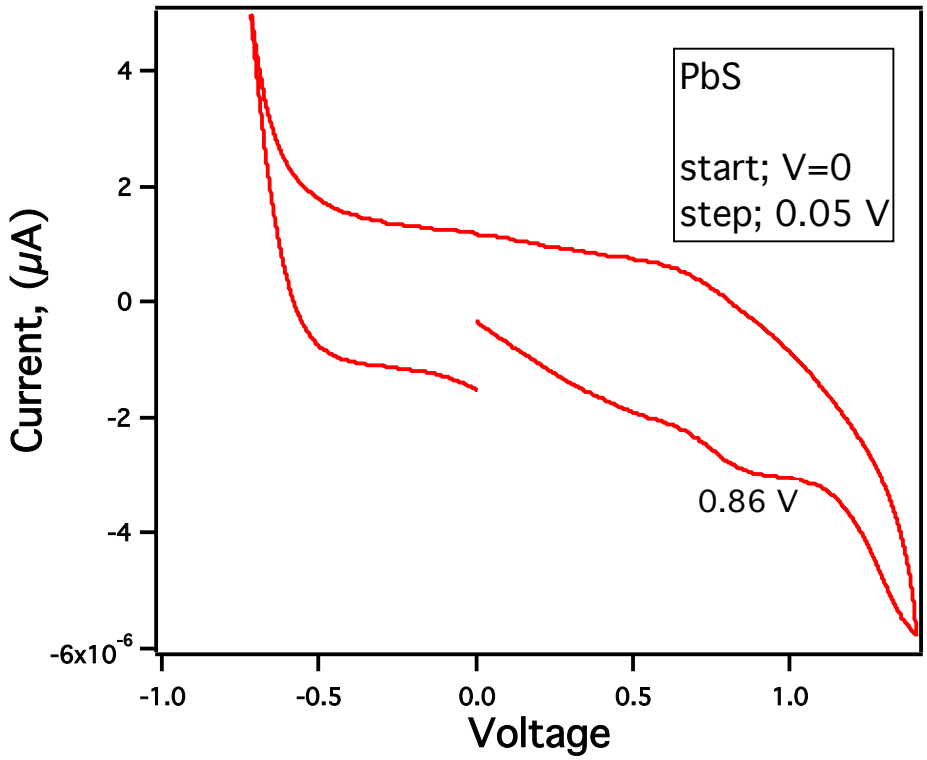

Figure B.2: CV curve of HOA-coated PbS QD thin film. The peak first excitation of these QDs was at 955 nm (1.3 eV) and are identical to the most commonly used PbS QD utilized in depleted heterojunction colloidal quantum dot photovoltaics such as though produced in the Sargent lab and The University of Toronto. Importantly, these dots are measured here as synthesized, without any form of ligand exchange that is present in every QD thin film for PV applications.

The interpretation of these CV curves is quite straightforward for gaining base-level interpretation of the position, relative to vacuum, of the conduction band edge. My focus throughout this CV work was this value because throughout my work with thin film solar cells, metal oxide wide band gap semiconductors (in this case, TiO_2) were used as

heterojunctions and electron acceptors. If the conduction band energy level of the QDs one is attempting to use as an absorber is deeper than the conduction band level of TiO_2, electron transfer from the QDs in to the oxide will be unfavorable and device performance will suffer greatly. The Bard lab published a report in 2001 in which they succinctly outlined the interpretation of CV curves on QDs such as these, which was used the basis for drawing conclusions from the data seen in this Chapter.[146] Simply put, valence and conduction band edges can be assigned to the negative oxidation peak and positive reduction peak, respectively, that lay furthest from the 0 V point. The vacuum level energy can be calculated relative to the reference electrode Fermi level, which has been previously shown to be -4.9 eV for $Ag/AgCl_2$ electrodes.[151] In this way, our data allows us to estimate the conduction band edge energy of the E_g = 1.3 eV PbS QDs to -4.9 V + 0.86 V = -4.04 V (-4.04 eV) relative to vacuum. This value compares well with published energy values for PbS QDs, including one published study utilizing this very method.[128,152]

In seeking to apply this method to cross reference similar published values for separate QD systems, I attempted to same experiment with $CuInS_2$ (CIS) particles synthesized following a procedure from the Klimov group (Figure B.3).[59] Electron injection studies for these tetrahedral particles generally place the conduction band edge for ~3 nm diameter CIS QDs at ~-3.0 eV. Applying the same principles described for the PbS QDs to this system, we arrive at a conduction band edge energy for CIS of -4.9 + 1.7 = -3.2 eV. This offset in conduction band values is much larger with respect to TiO_2 than in the case of PbS QDs, so one might expect increased electron injection rate.

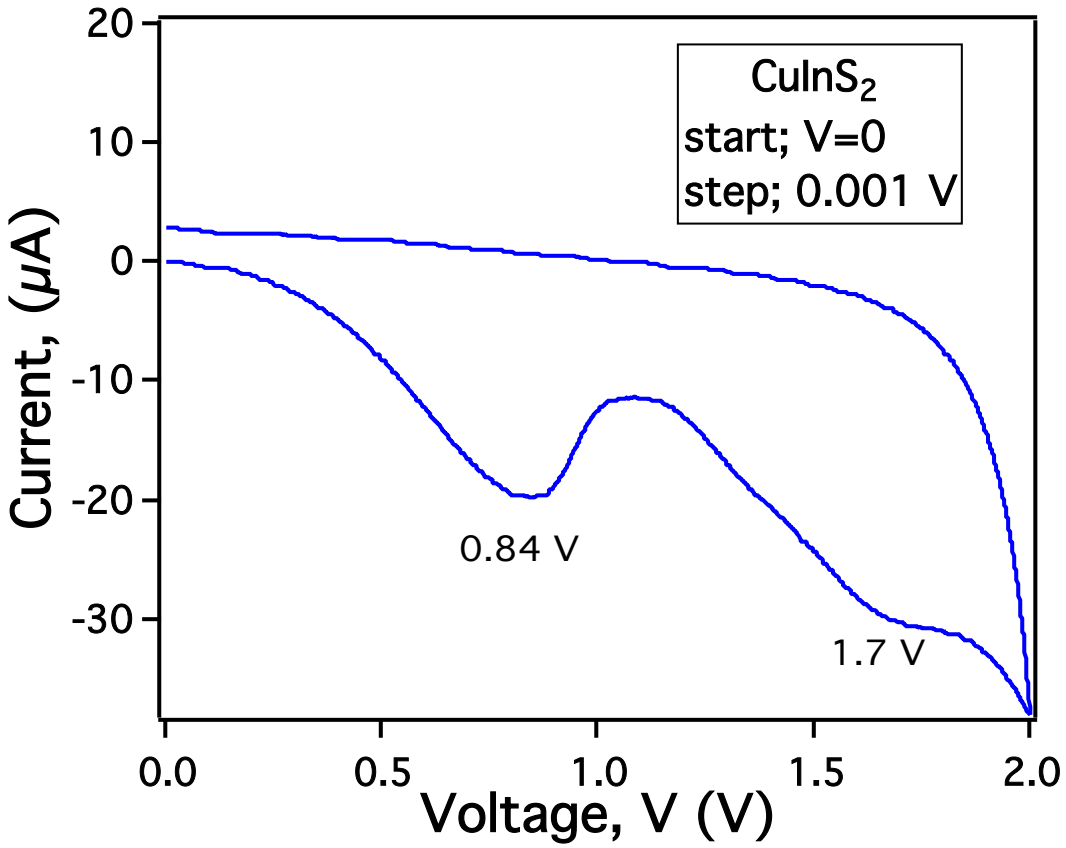

Figure B.3: CV curve of ~3 nm, E_g = 2.0 eV $CuInS_2$ QDs. The 1.7 V peak can be used to calculate the conduction band edge energy value to -3.2 eV, which agrees rather well with previously published reports and should facilitate good acceleration of electrons from CIS to TiO_2.

Finally, a collaborative effort in 2011 with Dr. Melissa Harrison, a former graduate student in the Rosenthal lab, focused on the attempted determination of alloyed CdPbSe QDs, which were under consideration for usage as active absorbers in PVs similar to those described above with a TiO_2 heterojunction.

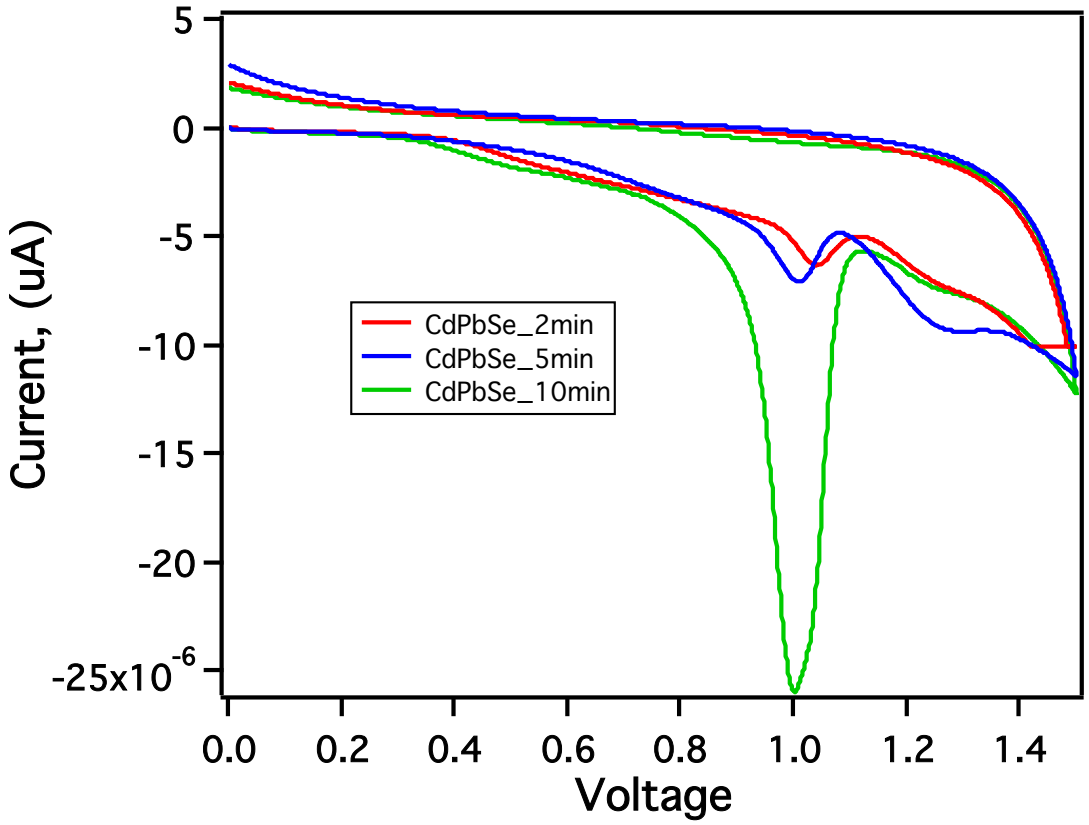

Figure B.4: CV curves of CdPbSe QD thin films corresponding to 2, 5 and 10 minute growth times. Two peaks exists in each curve, both of which shift with changes in QD growth time.

As can be seen in Figure B.4, the CV curves feature two prominent curves in the positive region of the voltage sweep. The sharp peaks near the 1.0 V mark shift towards lower voltage with increased growth time, from roughly 1.05 to 1.0 V through 10 minutes of growth. The smaller peaks in the 1.3 V region undergo similar shifts of roughly 0.04-0.05 V as well. Also of note are the relative intensities of the two peaks within a given curve. The higher voltage peak becomes negligible after the 10 minutes of growth time, which may suggest that this peak corresponds to a particular crystal. Interestingly, the

roughly 1.2 V peak would lead to a conduction band edge value of ~-3.7 eV, which agrees rather well with published values CdSe. Similarly, the lower voltage peak leads to ~-3.9 eV band edges which correspond to values in lead chalcogens such as those described above. Overall, this trend hints a sort of gradual alloying which has been seen in a related study performed in our group.[16] Beyond this, however, there was not much to be taken from this experiment beyond the fact that both the peaks in the CV curve for all of ever time mark in this reaction lied well above the conduction band value for TiO_2, suggesting that they would serve as suitable candidates for sensitization.

C. ON-PARTICLE LIGAND MODIFICATION WITHOUT EXCHANGE

C.1. Motivation and Background

The expansive field of nanocrystal research has evolved to find application in topics ranging from biological labeling to photovoltaics to fundamental physical studies. One critical aspect that is a nexus between these and other nanocrystal pursuits is perhaps simultaneously their most chemically interesting and finicky aspect: the surface. This is, of course, not revelatory in the least. Researchers are now privy to the fact that surface chemistry heavily influences solubility, doping, wave function distribution, photoluminescence (PL) quantum yield, band edge energy, superlattice packing, etc.[148,153-158] Most often, experiments involving the need for a custom-functionalized surface involve running established synthetic protocols and ligand exchanging unwanted and generally bulky native ligands for a functionally relevant species. However, in solution this process is no small task; particles have a strong tendency to agglomerate and concentration is of utmost importance. In solid-state thin film exchanges, native insulating ligands are replaced layer-by-layer with differing types of thiolates which have strong binding capacities but are unfortunately known to introduce hole traps and decrease stability of the colloid in air.[159] The ideal ligand exchange scenario—that which follows Occam's razor most closely—is one that happens pre-synthetically in a lab notebook.

C.2. Proposed Experiments and Hypothetical Applications

This project would encompass two main pursuits: (1) the synthesis of multiple types of QDs (CdSe, PbS) with a prototype short-chain oleic acid (HOA) analog, and (2)

the post synthetic chemical modification of these new native ligands to groups of interest in varied applications. With the second goal in mind, a suitable starting point for this "prototype" in goal (1) would be 3-butenoic acid (Figure C.1). The short length of its carbon chain—similar to that of the commonplace 3-mercaptopropionic acid (MPA)—should facilitate charge transport in thin film applications, while the carboxylate binding group simultaneously retains the beneficial passivation properties (high QY) of HOA and the like.

The presence of a terminal alkene group opens a range of chemical modification options that can introduce easily tailorable groups designed to controllably alter the QD's electronic and chemical properties. A suitable proof-of-principle experiment for this modification process would be a simple dibromination of the terminal C-C double bond. Elemental bromine reacts rapidly and in near unity yield with alkene groups through the well-studied bromonium ion formation and subsequent nucleophilic Br^- attack to add Br_2 across a double bond, which should be evidenced in IR spectra of QD samples by a disappearance of alkene stretches in the 1600 cm^{-1} region and growth of strong stretches between 500-600 cm^{-1} corresponding to C-Br bonds.

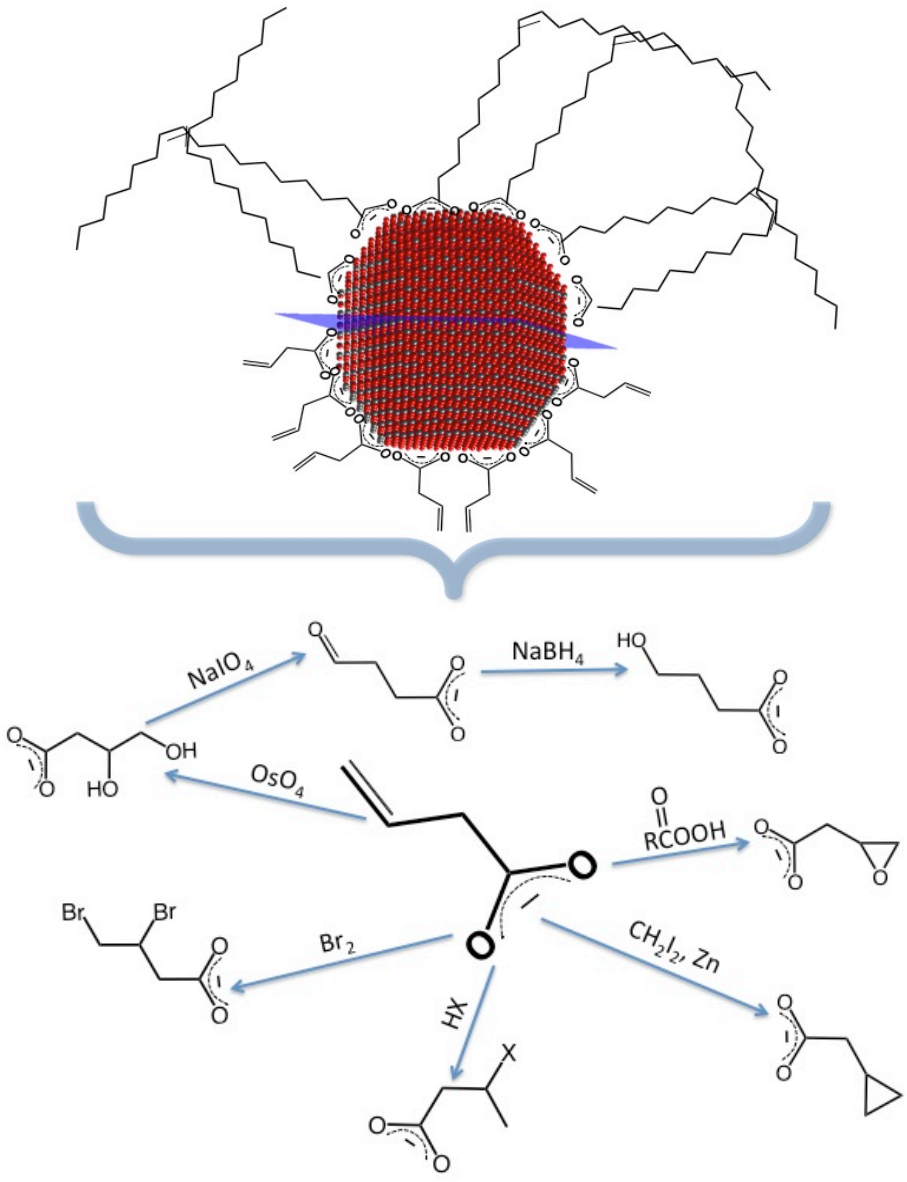

Figure C.1: (top) Representative QD cartoon depicting the length difference of oleic acid (top half) and 3-butenoic acid (bottom half). With similar length to commonly implemented ligands in charge transport applications such as benzene dithiol and 3-mercaptopropionic acid, 3-butenoic acid would allow for dot-to-dot electronic coupling *as synthesized.* (bottom) Scheme outlining several possible synthetic modifications to the alkene group.

The use of 3-butenoic acid, if successful, would instigate investigation of the commercially available, but more expensive, 3-butynoic acid for use in any number of click chemistry reactions such as cylcoadditions and Diels-Alder processes. Furthermore, owing to the usefulness and, azide-functionalized drug derivatives could be used to perform Cu-catalyzed Huisgen-like click reactions *in situ* between QDs and site-specific drug molecules through the following general mechanism:

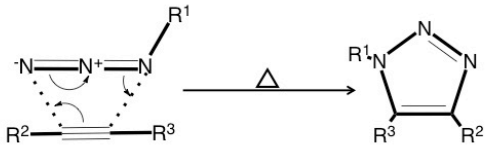

These high yield and idealized coupling reactions open possibilities in projects such as multi-modal cell surface tracking of QDs as highly site-specific fluorescent probes in biological studies, QD-silica attachment without altering QD surface chemistry, and covalent linkage and electronic coupling to polymers of interest like poly-3-hexylthiophene (P3HT) (Figure C.2).

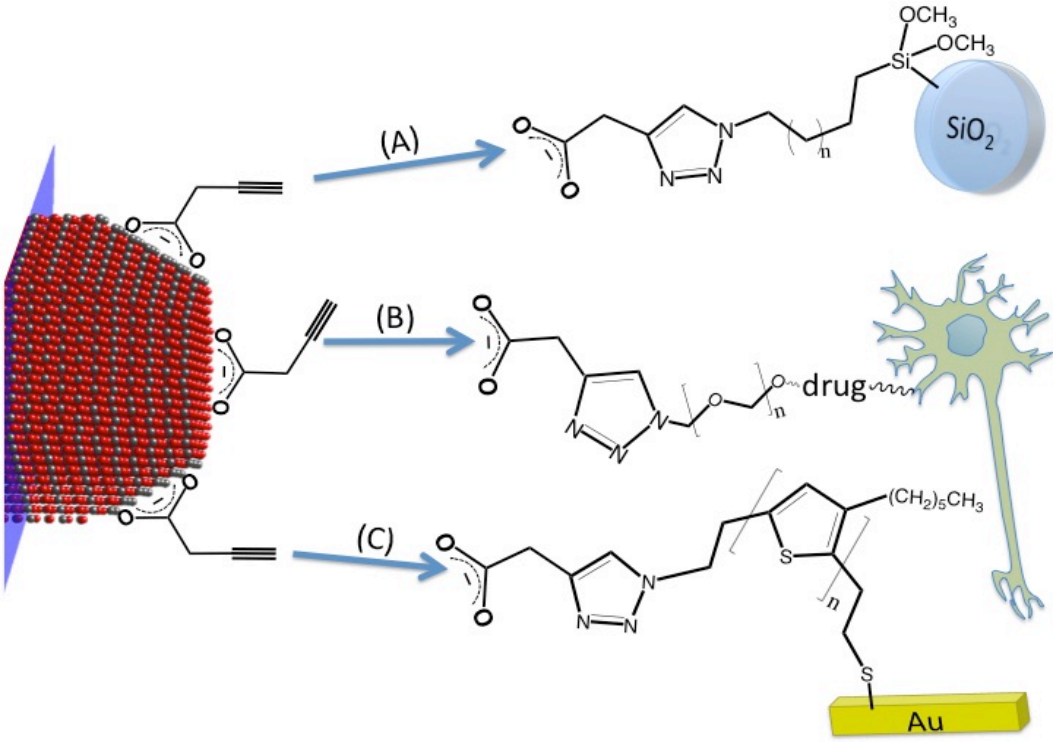

Figure C.2. Schemes displaying several possible applications of Huisgen-derived click chemistry for selective binding of QD-ligated alkynes with azide-functionalized targets: (A) binding to silica surface with azide-alkyl trimethoxysilane linkers; (B) linking to cellular surface-bound proteins with azide-tagged PEG-drug derivative moieties; (C) Au functionalization, shown here with modified P3HT chains for molecular wire directed charge transport between QD and Au electrode.

Importantly, the success of this project would not hinge solely upon the viability of 3-butenoic acid as an as-synthesized ligand. There are several predictable difficulties that could prove too troublesome to overcome for a given QD material: agglomeration may predominate with such short ligands during the growth process; solubility of precursors may be prohibitively different from that of the formed QDs, leading to unstable reaction environments. Commercially available 3-decenoic acid is an attractive

candidate for use in syntheses that mimics the procedure by Scholes and coworkers[107], yielding the HOA-capped PbS particles mentioned previously, as well as any number of methods using Cd-oleate as a precursor to cadmium chalcogenide cores or core/shells.[16] While shorter than HOA, 3-decenoic acid would still render the ligated particles highly hydrophobic. And, as a precursor it should have similar solubility properties as HOA pre-synthesis, suggesting that it may be viable as a more straightforward replacement. Cleavage of the alkene group of bound 3-decenoic acid can be achieved through the oxidative route using first OsO_4 to form a diol, followed by cleavage with $NaIO_4$ to the aldehyde outlined in Figure 1, yielding equivalent ligand moieties as those seen when starting with 3-butenoic acid. However, the oxidative processes needed to cleave the alkene in longer-chain ligands may prove detrimental to QDs, limiting their application to core/shell systems in which the emissive core is insulated from the chemistry of the surface.

C.3. Preliminary Attempts at Simple On-Particle Chemistry, 3-decenoic Acid Synthesis

Few attempts at experiments outlined in this section have been tried, as it was largely conceived toward the end of my graduate career. That being said, there was one set of treatments that were performed over the course of several weeks that met limited success. These treatments dealt with the halogenation of alkenes on on-particle ligands, as briefly outline in Figure C.1. The quantum dots used were HOA-coated CdSSe graded alloy particles based on a synthesis published by a previous Rosenthal group graduate student Melissa Harrison.[16] These particles were chosen based upon their ease of

synthesis, good quantum yields, stability to air and oxidation in general, as well as the fact they are synthesized using carboxylate ligands. Initially, these assays were attempted with 3-decenoic acid as a ligating species. To my knowledge, this is the first time anyone has used 3-decenoic as a ligand in the synthesis of QDs. Its implementation was rather straightforward, and it was simply substituted for HOA in an adaptation of the published synthesis mentioned above.

Briefly, for the synthesis of both 3-decenoic-ligated or HOA-ligated QDs, 1 mmol CdO (0.128 g), 1.3 mL oleic acid (HOA) or 0.8 mL 3-decenoic acid, and 20 mL 1-octadecene (ODE) were heated to 100 °C under vacuum for 10 minutes, and subsequently purged with Ar. The temperature was increased to 260 °C and the conversion of red CdO to colorless Cd-oleate was monitored to completion, after which the reaction temperature is reduced to 220 °C. Solutions of 0.75 M S: and Se:TBP in ODE were prepared separately and 0.8 mL aliquots of each were pulled into the same syringe. The S/Se syringe was swiftly injected into the Cd-oleate flask at 220 °C and the reaction proceeded for 2 hours. The nanocrystals were cooled and precipitated with a 3:1 mixture of butanol and ethanol, resuspended in toluene, and precipitated twice more with pure ethanol. After being finally suspended in toluene, the nanocrystals were passed through a 0.45 μm PTFE syringe filter and stored.

UV-VIS spectra are shown in figure C.3 for the evolution of the 3-decenoic acid ligated CdSSe QDs. 3-decenoic can act as a viable ligand and the evolution of the CdSSe QDs throughout the reaction is mirrored between that of the HOA and 3-decenoic syntheses.

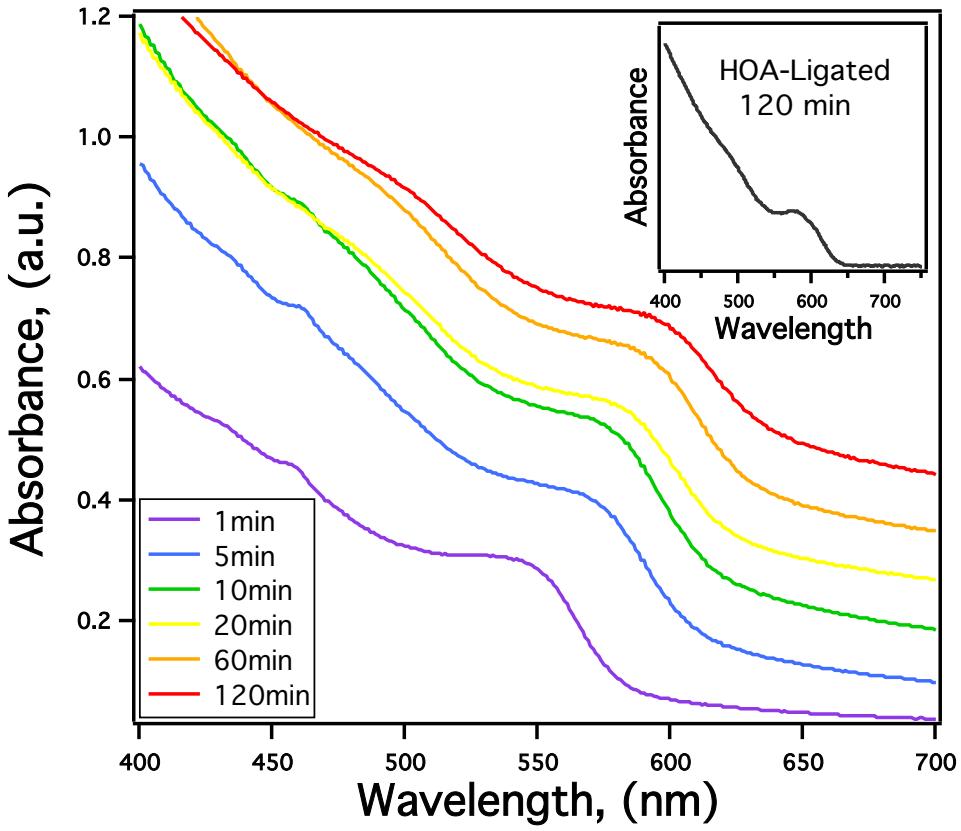

Figure C.3: Evolution of 3-decenoic acid-ligated CdSSe QDs over two hours, with HOA-coated for comparison (inset). 3-decenoic acid seems to perform very similarly to HOA. To the best of my knowledge, this is the first time this ligand has been used for synthesis of QDs—it may be found to be successful in other applications.

Both HOA and 3-decenoic acid are monounsaturated alkyl compounds, and the initial attempts at on-particle ligand modification, as mentioned before, was the halogenation of these double bonds followed by a phase transfer from organic (hexanes) to polar solvent (acetonitrile, AcN) through complexation to polyethylene glycol (PEG) moieties in a manner described in Figure C.4.

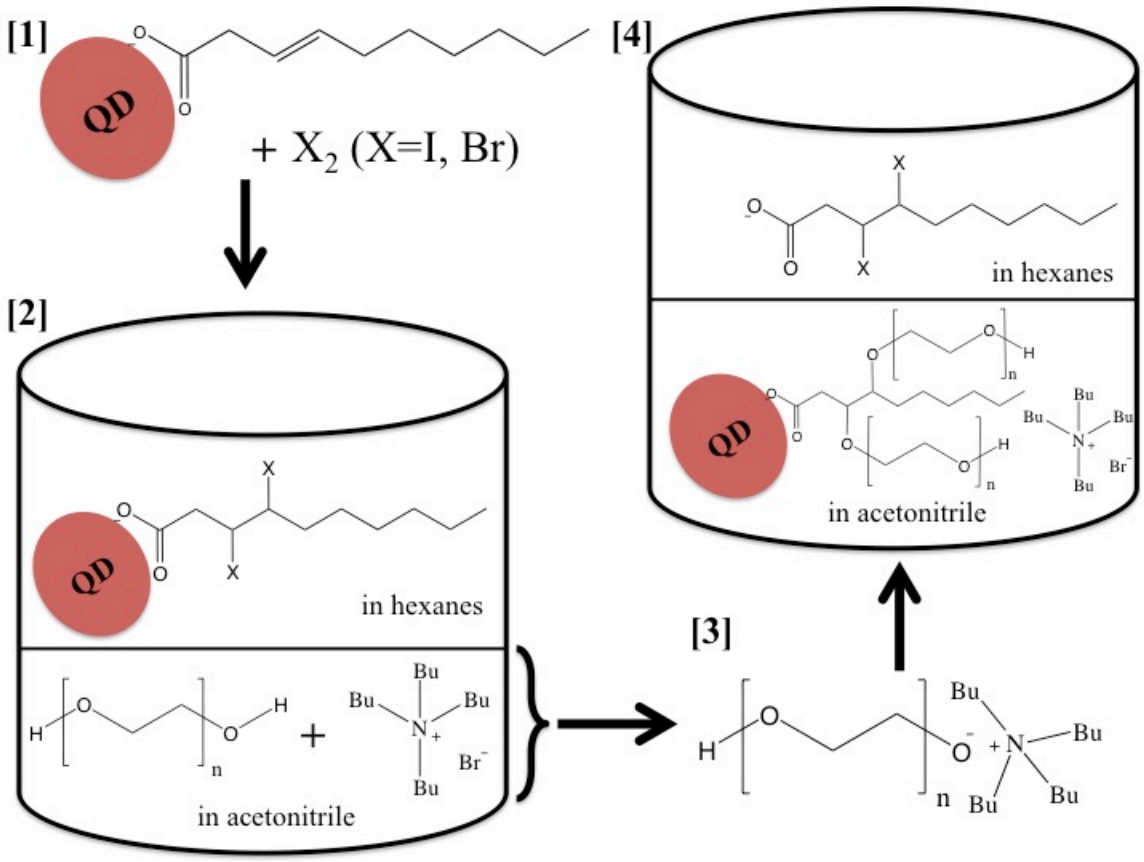

Figure C.4: Schematic outline the phase change PEGylation process of CdSSe ligated with 3-decenoic acid. In the proposed mechanism, PEG-400 and tert-butylammonium bromide (as a phase change catalyst) are used to perform an SN2 reaction on the halogenated carbon in the ligands chains. Hypothetically, this PEGylation will render the QDs soluble in aqueous solvents without modifying their surface coverage.

Many variations of concentrations were attempted within the general system shown in Figure C.3. The stepwise procedure that seemed to yield the best results was as follows:

(1) 0.8 mL of 1 mg/mL $N(Bu)_4Br$ in AcN plus 0.2 mL PEG-400 in small vial

(2) Cleaned dots are dispersed in hexanes and diluted to an optical density of 10, 1.0 mL placed in a small eppendorf tube

(3) 3 drops of 0.01 M I_2 in hexanes are added to the QDs

(4) QDs are pipetted into the PEG vial as an organic layer, the vial is magnetically stirred for 1 hour.

Procedures such as this eventually yield vials such those seen in Figure C.5.

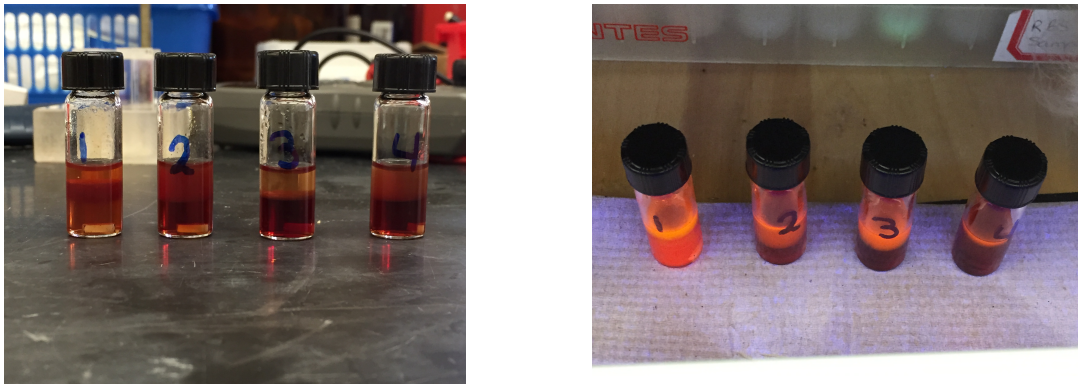

Figure C.5: Images of vials containing attempted phase exchange procedures. Vial 1 retains a large portion of its fluorescence after the phase transfer process (QY = 6.3%), and follows the procedure described above. All procedures results in soluble QDs in polar solvent (as seen in the picture to the left), however often times the there is considerable

PL quenching. Vials 2, 3 and 4 that result in phase-transferred QDs with quenched PL differ from vial 1 in their concentration of $N(Bu)_4Br$ catalyst.

While these results may at first seem very promising, I was quickly discouraged to find that, in fact, I_2 does not readily reduce alkene bonds and that the proposed halogenation reaction would only occur and be stable at low temperatures. To test this, I placed a small about of I_2 solution in a vial of the otherwise inert solvent octadecene (ODE) and stirred the purple solution overnight. No color change was apparent, whereas, if the same test was performed with a solution of brown bromine in ODE, the solution of Br_2 went clear immediately as it contacted the ODE indicating rapid bromination of the alkene to form the colorless dibrominated alkane. This lead me to believe that rather than attaching PEG chains at the 3- and 4-carbons, the mechanism more resembles a deprotonation and stabilization of charged PEG-400 by the $N(Bu)_4Br$ catalyst followed by gradual replacement of native HOA ligands with charged PEG chains.

When attempting to use Br_2 in place of the 10 mM I_2 solution in hexanes, PL seemed to drop off precipitously at any concentration of bromine, hinting at its much higher reactivity. However, with a single drop of 5mM Br_2 in 1 mL of OD =10 QDs, PL was still apparent but the exchange reaction results were similar to that of I_2.

A final attempt was made in which the goal was synthesize CdSSe QDs with pre-brominated HOA. In the typical reaction described above, 1.3 mL HOA (4 mmol) is use to create the Cd-oleate precursor. Accordingly, 1.3 mL of HOA was placed in a typical 3-neck round bottom reaction flask, into which a total of 5 mmol (0.25 mL) of pure Br_2 was added dropwise at room temperature. Due to the excess of Br_2 in the addition volume, the resultant solution was dark brown, however the addition of the ODE was expected to

quench any free Br_2 in the solution. The addition ODE did indeed lighten the flask some, but the solution was still pale yellow. Regardless, 0.128 g CdO was added to the flask and the conversion to Cd-oleate was attempted under typical conditions at 260 °C, which resulted in a black solution that was an obvious failure. Regardless of Br_2 volume, the Cd-oleate conversion process always failed due to the creation of unwanted materials stemming from the presence in some form of bromine. At this point, the project was put aside due to time constraints and focus was given to other more prescient projects. I do believe, though, that these pursuits hold quite a bit of promise and are fitting projects for chemistry undergraduates or as side projects for graduate students with downtime between experiments. There are myriad possibilities within this general idea—all of which require very little QD volume—which makes it possible to simply use "off-the-shelf" chemicals highly experimentally and quickly.

REFERENCES

1 Radisavljevic, B., Radenovic, A., Brivio, J., Giacometti, V. & Kis, A. Single-layer MoS2 transistors. *Nature Nanotechnology* **6**, 147-150, doi:10.1038/nnano.2010.279 (2011).

2 Mak, K. F., Lee, C., Hone, J., Shan, J. & Heinz, T. F. Atomically Thin MoS2: A New Direct-Gap Semiconductor. *Physical Review Letters* **105**, doi:10.1103/PhysRevLett.105.136805 (2010).

3 Anker, J. N. *et al.* Biosensing with plasmonic nanosensors. *Nature Materials* **7**, 442-453, doi:10.1038/nmat2162 (2008).

4 Linic, S., Christopher, P. & Ingram, D. B. Plasmonic-metal nanostructures for efficient conversion of solar to chemical energy. *Nature Materials* **10**, 911-921, doi:10.1038/nmat3151 (2011).

5 Liu, M., Johnston, M. B. & Snaith, H. J. Efficient planar heterojunction perovskite solar cells by vapour deposition. *Nature* **501**, 395-+, doi:10.1038/nature12509 (2013).

6 Burschka, J. *et al.* Sequential deposition as a route to high-performance perovskite-sensitized solar cells. *Nature* **499**, 316-+, doi:10.1038/nature12340 (2013).

7 Kojima, A., Teshima, K., Shirai, Y. & Miyasaka, T. Organometal Halide Perovskites as Visible-Light Sensitizers for Photovoltaic Cells. *Journal of the American Chemical Society* **131**, 6050-+, doi:10.1021/ja809598r (2009).

8 Extance, A. *New Ion Continues Perovskite Solar's Flat Out Progress*, <http://www.rsc.org/chemistryworld/2015/01/new-ion-continues-perovskite-solar-cell-record-flat-out-progress> (2015).

9 Keene, J. D., McBride, J. R., Orfield, N. J. & Rosenthal, S. J. Elimination of Hole-Surface Overlap in Graded CdSxSe1-x Nanocrystals Revealed by Ultrafast Fluorescence Upconversion Spectroscopy. *Acs Nano* **8**, 10665-+, doi:10.1021/nn504235w (2014).

10 Orfield, N. J., McBride, J. R., Keene, J. D., Davis, L. M. & Rosenthal, S. J. **- 9**, - 839 (2014).

11 Underwood, D. F., Kippeny, T. & Rosenthal, S. J. Ultrafast carrier dynamics in CdSe nanocrystals determined by femtosecond fluorescence upconversion spectroscopy. *Journal of Physical Chemistry B* **105**, 436-443, doi:10.1021/jp003088b (2001).

12 Rosenthal, S. J. Bar-coding biomolecules with fluorescent nanocrystals. *Nature Biotechnology* **19**, 621-622, doi:10.1038/90213 (2001).

13 Bentzen, E. L. *et al.* Surface modification to reduce nonspecific binding of quantum dots in live cell assays. *Bioconjugate Chemistry* **16**, 1488-1494, doi:10.1021/bc0502006 (2005).

14 Rosenthal, S. J., Chang, J. C., Kovtun, O., McBride, J. R. & Tomlinson, I. D. Biocompatible Quantum Dots for Biological Applications. *Chemistry & Biology* **18**, 10-24, doi:10.1016/j.chembiol.2010.11.013 (2011).

15 Niezgoda, J. S., Harrison, M. A., McBride, J. R. & Rosenthal, S. J. Novel Synthesis of Chalcopyrite CuxInyS2 Quantum Dots with Tunable Localized Surface

Plasmon Resonances. *Chemistry of Materials* **24**, 3294-3297, doi:10.1021/cm3021462 (2012).
16 Harrison, M. A., Ng, A., Hmelo, A. B. & Rosenthal, S. J. CdSSe Nanocrystals with Induced Chemical Composition Gradients. *Israel Journal of Chemistry* **52**, 1063-1072, doi:10.1002/ijch.201200040 (2012).
17 Bowers, M. J., McBride, J. R. & Rosenthal, S. J. White-light emission from magic-sized cadmium selenide nanocrystals. *Journal of the American Chemical Society* **127**, 15378-15379, doi:10.1021/ja055470d (2005).
18 Swafford, L. A. *et al.* Homogeneously alloyed CdSxSe1-(x) nanocrystals: Synthesis, characterization, and composition/size-dependent band gap. *Journal of the American Chemical Society* **128**, 12299-12306, doi:10.1021/ja063939e (2006).
19 Ng, A., Poplawsky, J. D., Li, C., Pennycook, S. J. & Rosenthal, S. J. Direct Electronic Property Imaging of a Nanocrystal-Based Photovoltaic Device by Electron Beam-Induced Current via Scanning Electron Microscopy. *Journal of Physical Chemistry Letters* **5**, 856-860, doi:10.1021/jz402752k (2014).
20 Schreuder, M. A. *et al.* Encapsulated white-light CdSe nanocrystals as nanophosphors for solid-state lighting. *Journal of Materials Chemistry* **18**, 970-975, doi:10.1039/b716803a (2008).
21 Rosson, T. E., Claiborne, S. M., McBride, J. R., Stratton, B. S. & Rosenthal, S. J. Bright White Light Emission from Ultrasmall Cadmium Selenide Nanocrystals. *Journal of the American Chemical Society* **134**, 8006-8009, doi:10.1021/ja300132p (2012).
22 Niezgoda, J. S., Yap, E., Keene, J. D., McBride, J. R. & Rosenthal, S. J. Plasmonic CuxInyS2 Quantum Dots Make Better Photovoltaics Than Their Nonplasmonic Counterparts. *Nano Letters* **14**, 3262-3269, doi:10.1021/nl500645k (2014).
23 Smith, N. J., Emmett, K. J. & Rosenthal, S. J. Photovoltaic cells fabricated by electrophoretic deposition of CdSe nanocrystals. *Applied Physics Letters* **93**, doi:10.1063/1.2965464 (2008).
24 Ekimov, A. I., Efros, A. L. & Onushchenko, A. A. QUANTUM SIZE EFFECT IN SEMICONDUCTOR MICROCRYSTALS. *Solid State Communications* **56**, 921-924, doi:10.1016/s0038-1098(85)80025-9 (1985).
25 Rossetti, R., Nakahara, S. & Brus, L. E. QUANTUM SIZE EFFECTS IN THE REDOX POTENTIALS, RESONANCE RAMAN-SPECTRA, AND ELECTRONIC-SPECTRA OF CDS CRYSTALLITES IN AQUEOUS-SOLUTION. *Journal of Chemical Physics* **79**, 1086-1088, doi:10.1063/1.445834 (1983).
26 Vossmeyer, T. *et al.* CDS NANOCLUSTERS - SYNTHESIS, CHARACTERIZATION, SIZE-DEPENDENT OSCILLATOR STRENGTH, TEMPERATURE SHIFT OF THE EXCITONIC-TRANSITION ENERGY, AND REVERSIBLE ABSORBENCY SHIFT. *Journal of Physical Chemistry* **98**, 7665-7673, doi:10.1021/j100082a044 (1994).
27 Dai, Q. Q. *et al.* Size-Dependent Composition and Molar Extinction Coefficient of PbSe Semiconductor Nanocrystals. *Acs Nano* **3**, 1518-1524, doi:10.1021/nn9001616 (2009).

28 Yu, W. W., Qu, L. H., Guo, W. Z. & Peng, X. G. Experimental determination of the extinction coefficient of CdTe, CdSe, and CdS nanocrystals. *Chemistry of Materials* **15**, 2854-2860, doi:10.1021/cm034081k (2003).
29 Booth, M., Brown, A. P., Evans, S. D. & Critchley, K. Determining the Concentration of CuInS2 Quantum Dots from the Size-Dependent Molar Extinction Coefficient. *Chemistry of Materials* **24**, 2064-2070, doi:10.1021/cm300227b (2012).
30 Alivisatos, A. P. Semiconductor clusters, nanocrystals, and quantum dots. *Science* **271**, 933-937, doi:10.1126/science.271.5251.933 (1996).
31 Shockley, W. & Queisser, H. J. Detailed Balance Limit of Efficiency of p-n Junction Solar Cells. *Journal of Applied Physics* **32**, 510-519 (1960).
32 Kao, C.-S., Chen, F.-C., Liao, C.-W., Huang, M. H. & Hsu, C.-S. Plasmonic-enhanced performance for polymer solar cells prepared with inverted structures. *Applied Physics Letters* **101**, doi:10.1063/1.4766736 (2012).
33 Atwater, H. A. & Polman, A. Plasmonics for improved photovoltaic devices. *Nature Materials* **9**, 205-213, doi:10.1038/nmat2629 (2010).
34 Green, M. A. Third generation photovoltaics: Ultra-high conversion efficiency at low cost. *Progress in Photovoltaics* **9**, 123-135 (2001).
35 Rand, B. P., Peumans, P. & Forrest, S. R. Long-range absorption enhancement in organic tandem thin-film solar cells containing silver nanoclusters. *Journal of Applied Physics* **96**, 7519-7526, doi:10.1063/1.1812589 (2004).
36 Goh, C., Scully, S. R. & McGehee, M. D. Effects of molecular interface modification in hybrid organic-inorganic photovoltaic cells. *Journal of Applied Physics* **101**, doi:114503
10.1063/1.2737977 (2007).
37 Gowrishankar, V., Scully, S. R., McGehee, M. D., Wang, Q. & Branz, H. M. Exciton splitting and carrier transport across the amorphous-silicon/polymer solar cell interface. *Applied Physics Letters* **89**, doi:252102
10.1063/1.2408641 (2006).
38 Smestad, G. P. & Gratzel, M. Demonstrating electron transfer and nanotechnology: A natural dye-sensitised nanocrystalline energy converter. *Journal of Chemical Education* **75**, 752-756 (1998).
39 Zhang, D. *et al.* Enhanced performance of dye-sensitized solar cells using gold nanoparticles modified fluorine tin oxide electrodes. *Journal of Physics D-Applied Physics* **46**, doi:10.1088/0022-3727/46/2/024005 (2013).
40 Hetsch, F., Xu, X. Q., Wang, H. K., Kershaw, S. V. & Rogach, A. L. Semiconductor Nanocrystal Quantum Dots as Solar Cell Components and Photosensitizers: Material, Charge Transfer, and Separation Aspects of Some Device Topologies. *Journal of Physical Chemistry Letters* **2**, 1879-1887, doi:10.1021/jz200802j (2011).
41 Shen, Y.-J. & Lee, Y.-L. Assembly of CdS quantum dots onto mesoscopic TiO(2) films for quantum dot-sensitized solar cell applications. *Nanotechnology* **19**, doi:10.1088/0957-4484/19/04/045602 (2008).
42 Kamat, P. V. Quantum Dot Solar Cells. Semiconductor Nanocrystals as Light Harvesters. *Journal of Physical Chemistry C* **112**, 18737-18753, doi:10.1021/jp806791s (2008).

43 Klimov, V. I. Mechanisms for photogeneration and recombination of multiexcitons in semiconductor nanocrystals: Implications for lasing and solar energy conversion. *Journal of Physical Chemistry B* **110**, 16827-16845, doi:10.1021/jp0615959 (2006).
44 Nozik, A. J. *et al.* Semiconductor Quantum Dots and Quantum Dot Arrays and Applications of Multiple Exciton Generation to Third-Generation Photovoltaic Solar Cells. *Chemical Reviews* **110**, 6873-6890, doi:10.1021/cr900289f (2010).
45 Nozik, A. J. Quantum dot solar cells. *Physica E-Low-Dimensional Systems & Nanostructures* **14**, 115-120 (2002).
46 Lan, X., Masala, S. & Sargent, E. H. Charge-extraction strategies for colloidal quantum dot photovoltaics. *Nature Materials* **13**, 233-240, doi:10.1038/nmat3816 (2014).
47 Chuang, C.-H. M., Brown, P. R., Bulovic, V. & Bawendi, M. G. Improved performance and stability in quantum dot solar cells through band alignment engineering. *Nature Materials* **13**, 796-801, doi:10.1038/nmat3984 (2014).
48 Kramer, I. J. & Sargent, E. H. Colloidal Quantum Dot Photovoltaics: A Path Forward. *Acs Nano* **5**, 8506-8514, doi:10.1021/nn203438u (2011).
49 Zhao, Y. *et al.* Plasmonic Cu2-xS Nanocrystals: Optical and Structural Properties of Copper-Deficient Copper(I) Sulfides. *Journal of the American Chemical Society* **131**, 4253-4261, doi:10.1021/ja805655b (2009).
50 Brown, M. D. *et al.* Plasmonic Dye-Sensitized Solar Cells Using Core-Shell Metal-Insulator Nanoparticles. *Nano Letters* **11**, 438-445, doi:10.1021/nl1031106 (2011).
51 Torimoto, T. *et al.* Plasmon-Enhanced Photocatalytic Activity of Cadmium Sulfide Nanoparticle Immobilized on Silica-Coated Gold Particles. *Journal of Physical Chemistry Letters* **2**, 2057-2062, doi:10.1021/jz2009049 (2011).
52 Luther, J. M., Jain, P. K., Ewers, T. & Alivisatos, A. P. Localized surface plasmon resonances arising from free carriers in doped quantum dots. *Nature Materials* **10**, 361-366, doi:10.1038/nmat3004 (2011).
53 Li, D. S., Zou, Y. & Yang, D. R. Controlled synthesis of luminescent CuInS(2) nanocrystals and their optical properties. *Journal of Luminescence* **132**, 313-317, doi:10.1016/j.jlumin.2011.08.030 (2012).
54 Liu, S. Y., Zhang, H., Qiao, Y. & Su, X. G. One-pot synthesis of ternary CuInS(2) quantum dots with near-infrared fluorescence in aqueous solution. *Rsc Advances* **2**, 819-825, doi:10.1039/c1ra00802a (2012).
55 Li, S. J. *et al.* Alloyed (ZnSe)(x)(CuInSe(2))(1-x) and CuInSe(x)S(2-x) Nanocrystals with a Monophase Zinc Blende Structure over the Entire Composition Range. *Inorganic Chemistry* **50**, 11958-11964, doi:10.1021/ic201083r (2011).
56 Scheer, R., Alt, M., Luck, I. & Lewerenz, H. J. Electrical properties of coevaporated CuInS2 thin films. *Solar Energy Materials and Solar Cells* **49**, 423-430, doi:10.1016/s0927-0248(97)00127-x (1997).
57 Pan, D. C. *et al.* Synthesis of Cu-In-S ternary nanocrystals with tunable structure and composition. *Journal of the American Chemical Society* **130**, 5620-+, doi:10.1021/ja711027j (2008).

58 Xie, R. G., Rutherford, M. & Peng, X. G. Formation of High-Quality I-III-VI Semiconductor Nanocrystals by Tuning Relative Reactivity of Cationic Precursors. *Journal of the American Chemical Society* **131**, 5691-5697, doi:10.1021/ja9005767 (2009).

59 Li, L. A. *et al.* Efficient Synthesis of Highly Luminescent Copper Indium Sulfide-Based Core/Shell Nanocrystals with Surprisingly Long-Lived Emission. *Journal of the American Chemical Society* **133**, 1176-1179, doi:10.1021/ja108261h (2011).

60 Panthani, M. G. *et al.* Synthesis of CuInS(2), CuInSe(2), and Cu(In(x)Ga(1-x))Se(2) (CIGS) Nanocrystal "Inks" for Printable Photovoltaics. *Journal of the American Chemical Society* **130**, 16770-16777, doi:10.1021/ja805845q (2008).

61 Kruszynska, M., Borchert, H., Parisi, J. & Kolny-Olesiak, J. Investigations of solvents and various sulfur sources influence on the shape-controlled synthesis of CuInS(2) nanocrystals. *Journal of Nanoparticle Research* **13**, 5815-5824, doi:10.1007/s11051-011-0381-4 (2011).

62 Kruszynska, M., Borchert, H., Parisi, J. & Kolny-Olesiak, J. Synthesis and Shape Control of CuInS(2) Nanoparticles. *Journal of the American Chemical Society* **132**, 15976-15986, doi:10.1021/ja103828f (2010).

63 Nose, K., Soma, Y., Omata, T. & Otsuka-Yao-Matsuo, S. Synthesis of Ternary CuInS(2) Nanocrystals; Phase Determination by Complex Ligand Species. *Chemistry of Materials* **21**, 2607-2613, doi:10.1021/cm802022p (2009).

64 Castro, S. L., Bailey, S. G., Raffaelle, R. P., Banger, K. K. & Hepp, A. F. Nanocrystalline chalcopyrite materials (CuInS2 and CuInSe2) via low-temperature pyrolysis of molecular single-source precursors. *Chemistry of Materials* **15**, 3142-3147, doi:10.1021/cm034161o (2003).

65 Look, D. C. & Manthuruthil, J. C. ELECTRON AND HOLE CONDUCTIVITY IN CUINS2. *Journal of Physics and Chemistry of Solids* **37**, 173-180, doi:10.1016/0022-3697(76)90157-8 (1976).

66 Taylor, J., Kippeny, T. & Rosenthal, S. J. Surface stoichiometry of CdSe nanocrystals determined by Rutherford backscattering spectroscopy. *Journal of Cluster Science* **12**, 571-582, doi:10.1023/a:1014246315331 (2001).

67 Feldman, L. C. & Mayer, J. W. *Fundamentals of Thin Film Surface Analysis*. (North Holland Elsevier, 1986).

68 Shim, M. & Guyot-Sionnest, P. N-type colloidal semiconductor nanocrystals. *Nature* **407**, 981-983, doi:10.1038/35039577 (2000).

69 Kamlet, M. J., Abboud, J. L. & Taft, R. W. SOLVATOCHROMIC COMPARISON METHOD .6. PI-STAR SCALE OF SOLVENT POLARITIES. *Journal of the American Chemical Society* **99**, 6027-6038, doi:10.1021/ja00460a031 (1977).

70 Leatherdale, C. A. & Bawendi, M. G. Observation of solvatochromism in CdSe colloidal quantum dots. *Physical Review B* **63**, doi:10.1103/PhysRevB.63.165315 (2001).

71 Manthiram, K. & Alivisatos, A. P. Tunable Localized Surface Plasmon Resonances in Tungsten Oxide Nanocrystals. *Journal of the American Chemical Society* **134**, 3995-3998, doi:10.1021/ja211363w (2012).

72 Malinsky, M. D., Kelly, K. L., Schatz, G. C. & Van Duyne, R. P. Chain length dependence and sensing capabilities of the localized surface plasmon resonance of silver nanoparticles chemically modified with alkanethiol self-assembled monolayers. *Journal of the American Chemical Society* **123**, 1471-1482, doi:10.1021/ja003312a (2001).

73 Jain, P. K. & Ei-Sayed, M. A. Surface plasmon resonance sensitivity of metal nanostructures: Physical basis and universal scaling in metal nanoshells. *Journal of Physical Chemistry C* **111**, 17451-17454, doi:10.1021/jp0773177 (2007).

74 Rosenthal, S. J., McBride, J., Pennycook, S. J. & Feldman, L. C. Synthesis, surface studies, composition and structural characterization of CdSe, core/shell and biologically active nanocrystals. *Surface Science Reports* **62**, 111-157, doi:10.1016/j.surfrep.2007.02.001 (2007).

75 Polman, A. APPLIED PHYSICS Plasmonics Applied. *Science* **322**, 868-869, doi:10.1126/science.1163959 (2008).

76 Stuart, H. R. & Hall, D. G. Absorption enhancement in silicon-on-insulator waveguides using metal island films. *Applied Physics Letters* **69**, 2327-2329, doi:10.1063/1.117513 (1996).

77 Choi, H., Chen, W. T. & Kamat, P. V. Know Thy Nano Neighbor. Plasmonic versus Electron Charging Effects of Metal Nanoparticles in Dye-Sensitized Solar Cells. *Acs Nano* **6**, 4418-4427, doi:10.1021/nn301137r (2012).

78 Qi, J., Dang, X., Hammond, P. T. & Belcher, A. M. Highly Efficient Plasmon-Enhanced Dye-Sensitized Solar Cells through Metal@Oxide Core-Shell Nanostructure. *Acs Nano* **5**, 7108-7116, doi:10.1021/nn201808g (2011).

79 Chen, X. Q., Yang, X., Fu, W. F., Xu, M. S. & Chen, H. Z. Enhanced performance of polymer solar cells with a monolayer of assembled gold nanoparticle films fabricated by Langmuir-Blodgett technique. *Materials Science and Engineering B-Advanced Functional Solid-State Materials* **178**, 53-59, doi:10.1016/j.mseb.2012.10.024 (2013).

80 Salvador, M. *et al.* Electron Accumulation on Metal Nanoparticles in Plasmon-Enhanced Organic Solar Cells. *Acs Nano* **6**, 10024-10032, doi:10.1021/nn303725v (2012).

81 Gao, H. L. *et al.* Plasmon enhanced polymer solar cells by spin-coating Au nanoparticles on indium-tin-oxide substrate. *Applied Physics Letters* **101**, doi:10.1063/1.4754839 (2012).

82 Kalfagiannis, N. *et al.* Plasmonic silver nanoparticles for improved organic solar cells. *Solar Energy Materials and Solar Cells* **104**, 165-174, doi:10.1016/j.solmat.2012.05.018 (2012).

83 Konda, R. B. *et al.* Surface plasmon excitation via Au nanoparticles in n-CdSe/p-Si heterojunction diodes. *Applied Physics Letters* **91**, doi:10.1063/1.2807277 (2007).

84 Kirkengen, M., Bergli, J. & Galperin, Y. M. Direct generation of charge carriers in c-Si solar cells due to embedded nanoparticles. *Journal of Applied Physics* **102**, doi:10.1063/1.2809368 (2007).

85 Green, M. A. & Pillai, S. Harnessing plasmonics for solar cells. *Nature Photonics* **6**, 130-132 (2012).

86 Scotognella, F. *et al.* Plasmon Dynamics in Colloidal Cu2-xSe Nanocrystals. *Nano Letters* **11**, 4711-4717, doi:10.1021/nl202390s (2011).
87 Hessel, C. M. *et al.* Copper Selenide Nanocrystals for Photothermal Therapy. *Nano Letters* **11**, 2560-2566, doi:10.1021/nl201400z (2011).
88 Dorfs, D. *et al.* Reversible Tunability of the Near-Infrared Valence Band Plasmon Resonance in Cu2-xSe Nanocrystals. *Journal of the American Chemical Society* **133**, 11175-11180, doi:10.1021/ja2016284 (2011).
89 Zhang, J., Tang, Y., Lee, K. & Ouyang, M. Tailoring light-matter-spin interactions in colloidal hetero-nanostructures. *Nature* **466**, 91-95, doi:10.1038/nature09150 (2010).
90 Lee, J., Hernandez, P., Lee, J., Govorov, A. O. & Kotov, N. A. Exciton-plasmon interactions inmolecular spring assemblies of nanowires and wavelength-based protein detection. *Nature Materials* **6**, 291-295, doi:10.1038/nmat1869 (2007).
91 Okamoto, K. *et al.* Surface-plasmon-enhanced light emitters based on InGaN quantum wells. *Nature Materials* **3**, 601-605, doi:10.1038/nmat1198 (2004).
92 Akimov, A. V. *et al.* Generation of single optical plasmons in metallic nanowires coupled to quantum dots. *Nature* **450**, 402-406, doi:10.1038/nature06230 (2007).
93 Turo, M. J. & Macdonald, J. E. Crystal-Bound vs Surface-Bound Thiols on Nano crystals. *Acs Nano* **8**, 10205-10213, doi:10.1021/nn5032164 (2014).
94 Yue, W. *et al.* CuInS2 quantum dots synthesized by a solvothermal route and their application as effective electron acceptors for hybrid solar cells. *Journal of Materials Chemistry* **20**, 7570-7578, doi:10.1039/c0jm00611d (2010).
95 Shen, F., Que, W., Liao, Y. & Yin, X. Photocatalytic Activity of TiO2 Nanoparticles Sensitized by CuInS2 Quantum Dots. *Industrial & Engineering Chemistry Research* **50**, 9131-9137, doi:10.1021/ie2007467 (2011).
96 Shen, F. *et al.* Enhanced Photocatalytic Activity of ZnO Microspheres via Hybridization with CuInSe2 and CuInS2 Nanocrystals. *Acs Applied Materials & Interfaces* **4**, 4087-4092, doi:10.1021/am3008533 (2012).
97 Li, T.-L., Lee, Y.-L. & Teng, H. CuInS2 quantum dots coated with CdS as high-performance sensitizers for TiO2 electrodes in photoelectrochemical cells. *Journal of Materials Chemistry* **21**, 5089-5098, doi:10.1039/c0jm04276e (2011).
98 Li, T. L., Cai, C. D., Yeh, T. F. & Teng, H. S. Capped CuInS2 quantum dots for H-2 evolution from water under visible light illumination. *Journal of Alloys and Compounds* **550**, 326-330, doi:10.1016/j.jallcom.2012.10.157 (2013).
99 Kuo, K.-T., Liu, D.-M., Chen, S.-Y. & Lin, C.-C. Core-shell CuInS2/ZnS quantum dots assembled on short ZnO nanowires with enhanced photo-conversion efficiency. *Journal of Materials Chemistry* **19**, 6780-6788, doi:10.1039/b907765k (2009).
100 Chang, J.-Y., Su, L.-F., Li, C.-H., Chang, C.-C. & Lin, J.-M. Efficient "green'' quantum dot-sensitized solar cells based on Cu2S-CuInS2-ZnSe architecture. *Chemical Communications* **48**, 4848-4850, doi:10.1039/c2cc31229h (2012).

101 Hu, X. *et al.* Aqueous colloidal CuInS2 for quantum dot sensitized solar cells. *Journal of Materials Chemistry* **21**, 15903-15905, doi:10.1039/c1jm12629f (2011).
102 Li, T.-L., Lee, Y.-L. & Teng, H. High-performance quantum dot-sensitized solar cells based on sensitization with CuInS2 quantum dots/CdS heterostructure. *Energy & Environmental Science* **5**, 5315-5324, doi:10.1039/c1ee02253a (2012).
103 Wang, X. *et al.* A General Synthesis of Cu-In-S Based Multicomponent Solid-Solution Nanocrystals with Tunable Band Gap, Size, and Structure. *Journal of Physical Chemistry C* **114**, 17293-17297, doi:10.1021/jp103572g (2010).
104 Migliorato, P., Shay, J. L., Kasper, H. M. & Wagner, S. Analysis of the Electrical and Luminescent Properties of CuInSe2. *Journal of Applied Physics* **46**, 1777-1782 (1975).
105 Tell, B., Shay, J. L. & Kasper, H. M. Room‐Temperature Electrical Properties of Ten I‐III‐VI_2 Semiconductors. *Journal of Applied Physics* **43**, 2469-2470 (1972).
106 Hens, Z. & Martins, J. C. A Solution NMR Toolbox for Characterizing the Surface Chemistry of Colloidal Nanocrystals. *Chemistry of Materials* **25**, 1211-1221, doi:10.1021/cm303361s (2013).
107 Hines, M. A. & Scholes, G. D. Colloidal PbS nanocrystals with size-tunable near-infrared emission: Observation of post-synthesis self-narrowing of the particle size distribution. *Advanced Materials* **15**, 1844-1849, doi:10.1002/adma.200305395 (2003).
108 Krasovec, U. O., Berginc, M., Hocevar, M. & Topic, M. Unique TiO2 paste for high efficiency dye-sensitized solar cells. *Solar Energy Materials and Solar Cells* **93**, 379-381, doi:10.1016/j.solmat.2008.11.012 (2009).
109 Sinton, R. A. & Cuevas, A. Contactless determination of current-voltage characteristics and minority-carrier lifetimes in semiconductors from quasi-steady-state photoconductance data. *Applied Physics Letters* **69**, 2510-2512, doi:10.1063/1.117723 (1996).
110 Ip, A. H. *et al.* Hybrid passivated colloidal quantum dot solids. *Nature Nanotechnology* **7**, 577-582, doi:10.1038/nnano.2012.127 (2012).
111 Santra, P. K., Nair, P. V., Thomas, K. G. & Kamat, P. V. CuInS2-Sensitized Quantum Dot Solar Cell. Electrophoretic Deposition, Excited-State Dynamics, and Photovoltaic Performance. *Journal of Physical Chemistry Letters* **4**, 722-729, doi:10.1021/jz400181m (2013).
112 Plass, R., Pelet, S., Krueger, J., Gratzel, M. & Bach, U. Quantum dot sensitization of organic-inorganic hybrid solar cells. *Journal of Physical Chemistry B* **106**, 7578-7580, doi:10.1021/jp020453l (2002).
113 Shen, Q., Sato, T., Hashimoto, M., Chen, C. C. & Toyoda, T. Photoacoustic and photo electrochemical characterization of CdSe-sensitized TiO2 electrodes composed of nanotubes and nanowires. *Thin Solid Films* **499**, 299-305, doi:10.1016/j.tsf.2005.07.019 (2006).

114 Gunes, S. *et al.* Hybrid solar cells using HgTe nanocrystals and nanoporous TiO2 electrodes. *Advanced Functional Materials* **16**, 1095-1099, doi:10.1002/adfm.200500638 (2006).
115 Niitsoo, O. *et al.* Chemical bath deposited CdS/CdSe-sensitized porous TiO2 solar cells. *Journal of Photochemistry and Photobiology a-Chemistry* **181**, 306-313, doi:10.1016/j.jphotochem.2005.12.012 (2006).
116 Yu, P. *et al.* Nanocrystalline TiO2 solar cells sensitized with InAs quantum dots. *Journal of Physical Chemistry B* **110**, 25451-25454, doi:10.1021/jp064817b (2006).
117 Lin, S.-C., Lee, Y.-L., Chang, C.-H., Shen, Y.-J. & Yang, Y.-M. Quantum-dot-sensitized solar cells: Assembly of CdS-quantum-dots coupling techniques of self-assembled monolayer and chemical bath deposition. *Applied Physics Letters* **90**, doi:10.1063/1.2721373 (2007).
118 Lee, H. J. *et al.* Anchoring cadmium chalcogenide quantum dots (QDs) onto stable oxide semiconductors for QD sensitized solar cells. *Bulletin of the Korean Chemical Society* **28**, 953-958 (2007).
119 Diguna, L. J., Shen, Q., Kobayashi, J. & Toyoda, T. High efficiency of CdSe quantum-dot-sensitized TiO2 inverse opal solar cells. *Applied Physics Letters* **91**, doi:10.1063/1.2757130 (2007).
120 Kamat, P. V., Christians, J. A. & Radich, J. G. Quantum Dot Solar Cells: Hole Transfer as a Limiting Factor in Boosting the Photoconversion Efficiency. *Langmuir* **30**, 5716-5725, doi:10.1021/la500555w (2014).
121 Pattantyus-Abraham, A. G. *et al.* Depleted-Heterojunction Colloidal Quantum Dot Solar Cells. *Acs Nano* **4**, 3374-3380, doi:10.1021/nn100335g (2010).
122 Choi, J. J. *et al.* PbSe Nanocrystal Excitonic Solar Cells. *Nano Letters* **9**, 3749-3755, doi:10.1021/nl901930g (2009).
123 Luther, J. M. *et al.* Schottky Solar Cells Based on Colloidal Nanocrystal Films. *Nano Letters* **8**, 3488-3492, doi:10.1021/nl802476m (2008).
124 Leschkies, K. S., Beatty, T. J., Kang, M. S., Norris, D. J. & Aydil, E. S. Solar Cells Based on Junctions between Colloidal PbSe Nanocrystals and Thin ZnO Films. *Acs Nano* **3**, 3638-3648, doi:10.1021/nn901139d (2009).
125 Ng, A. *Characterization of Nanocrystal-Based Photovoltaics: Electron Microscopy & Electron Beam-Induced Current via Scanning Electron Microscopy* Ph.D. thesis, Vanderbilt University, (2014).
126 Brown, P. R. *et al.* Improved Current Extraction from ZnO/PbS Quantum Dot Heterojunction Photovoltaics Using a MoO3 Interfacial Layer. *Nano Letters* **11**, 2955-2961, doi:10.1021/nl201472u (2011).
127 Zhitomirsky, D. *et al.* Colloidal Quantum Dot Photovoltaics: The Effect of Polydispersity. *Nano Letters* **12**, 1007-1012, doi:10.1021/nl2041589 (2012).
128 Hyun, B.-R. *et al.* Electron Injection from Colloidal PbS Quantum Dots into Titanium Dioxide Nanoparticles. *Acs Nano* **2**, 2206-2212, doi:10.1021/nn800336b (2008).
129 Oregan, B., Moser, J., Anderson, M. & Gratzel, M. VECTORIAL ELECTRON INJECTION INTO TRANSPARENT SEMICONDUCTOR MEMBRANES AND ELECTRIC-FIELD EFFECTS ON THE DYNAMICS OF LIGHT-INDUCED CHARGE

SEPARATION. *Journal of Physical Chemistry* **94**, 8720-8726, doi:10.1021/j100387a017 (1990).
130 Nakade, S. *et al.* Enhancement of electron transport in nano-porous TiO2 electrodes by dye adsorption. *Electrochemistry Communications* **5**, 804-808, doi:10.1016/j.elecom.2003.07.008 (2003).
131 Zaban, A., Meier, A. & Gregg, B. A. Electric potential distribution and short-range screening in nanoporous TiO2 electrodes. *Journal of Physical Chemistry B* **101**, 7985-7990, doi:10.1021/jp971857u (1997).
132 Debnath, R. *et al.* Ambient-Processed Colloidal Quantum Dot Solar Cells via Individual Pre-Encapsulation of Nanoparticles. *Journal of the American Chemical Society* **132**, 5952-+, doi:10.1021/ja1013695 (2010).
133 Tang, J. & Sargent, E. H. Infrared Colloidal Quantum Dots for Photovoltaics: Fundamentals and Recent Progress. *Advanced Materials* **23**, 12-29, doi:10.1002/adma.201001491 (2011).
134 Sargent, E. H. Colloidal quantum dot solar cells. *Nature Photonics* **6**, 133-135 (2012).
135 Voznyy, O. *et al.* A Charge-Orbital Balance Picture of Doping in Colloidal Quantum Dot Solids. *Acs Nano* **6**, 8448-8455, doi:10.1021/nn303364d (2012).
136 Ning, Z. *et al.* Graded Doping for Enhanced Colloidal Quantum Dot Photovoltaics. *Advanced Materials* **25**, 1719-1723, doi:10.1002/adma.201204502 (2013).
137 Wang, H., Kubo, T., Nakazaki, J. & Segawa, H. PbS colloidal quantum dot/ZnO-based bulk-heterojunction solar cells with high stability under continuous light soaking. *Physica Status Solidi-Rapid Research Letters* **8**, 961-965, doi:10.1002/pssr.201409461 (2014).
138 Ding, B., Wang, Y., Huang, P.-S., Waldeck, D. H. & Lee, J.-K. Depleted Bulk Heterojunctions in Thermally Annealed PbS Quantum Dot Solar Cells. *Journal of Physical Chemistry C* **118**, 14749-14758, doi:10.1021/jp502356d (2014).
139 Barkhouse, D. A. R. *et al.* Depleted Bulk Heterojunction Colloidal Quantum Dot Photovoltaics. *Advanced Materials* **23**, 3134-+, doi:10.1002/adma.201101065 (2011).
140 Kramer, I. J. *et al.* Ordered Nanopillar Structured Electrodes for Depleted Bulk Heterojunction Colloidal Quantum Dot Solar Cells. *Advanced Materials* **24**, 2315-2319, doi:10.1002/adma.201104832 (2012).
141 Sakamoto, M. *et al.* (2015).
142 Mocatta, D. *et al.* Heavily Doped Semiconductor Nanocrystal Quantum Dots. *Science* **332**, 77-81, doi:10.1126/science.1196321 (2011).
143 Choi, J.-H. *et al.* Bandlike Transport in Strongly Coupled and Doped Quantum Dot Solids: A Route to High-Performance Thin-Film Electronics. *Nano Letters* **12**, 2631-2638, doi:10.1021/nl301104z (2012).
144 Prosser, J. H., Brugarolas, T., Lee, S., Nolte, A. J. & Lee, D. Avoiding Cracks in Nanoparticle Films. *Nano Letters* **12**, 5287-5291, doi:10.1021/nl302555k (2012).

145 Bao, Y. *et al.* Electrical and thermal conductivity of Ge/Si quantum dot superlattices. *Journal of the Electrochemical Society* **152**, G432-G435, doi:10.1149/1.1897365 (2005).
146 Haram, S. K., Quinn, B. M. & Bard, A. J. Electrochemistry of CdS nanoparticles: A correlation between optical and electrochemical band gaps. *Journal of the American Chemical Society* **123**, 8860-8861, doi:10.1021/ja0158206 (2001).
147 Kucur, E., Bucking, W., Giernoth, R. & Nann, T. Determination of defect states in semiconductor nanocrystals by cyclic voltammetry. *Journal of Physical Chemistry B* **109**, 20355-20360, doi:10.1021/jp053891b (2005).
148 Jasieniak, J., Califano, M. & Watkins, S. E. Size-Dependent Valence and Conduction Band-Edge Energies of Semiconductor Nanocrystals. *Acs Nano* **5**, 5888-5902, doi:10.1021/nn201681s (2011).
149 Medintz, I. L. *et al.* Interactions between Redox Complexes and Semiconductor Quantum Dots Coupled via a Peptide Bridge. *Journal of the American Chemical Society* **130**, 16745-16756, doi:10.1021/ja805456x (2008).
150 Bard, A. J., Ding, Z. F. & Myung, N. in *Semiconductor Nanocrystals and Silicate Naoparticles* Vol. 118 *Structure and Bonding* (eds X. Peng & D. M. P. Minogos) 1-57 (2005).
151 Fan, R. & Peterson, S. J. *Semiconductor Device-Based Sensors for Gas, Chemical and Bio-Medical Sensors*. 1 edn, 6 (CRC Press, 2011).
152 Dissanayake, D. M. N. M., Lutz, T., Curry, R. J. & Silva, S. R. P. Measurement and validation of PbS nanocrystal energy levels. *Applied Physics Letters* **93**, doi:10.1063/1.2964203 (2008).
153 Moreels, I. *et al.* Size-Tunable, Bright, and Stable PbS Quantum Dots: A Surface Chemistry Study. *Acs Nano* **5**, 2004-2012, doi:10.1021/nn103050w (2011).
154 Fafarman, A. T. *et al.* Thiocyanate-Capped Nanocrystal Colloids: Vibrational Reporter of Surface Chemistry and Solution-Based Route to Enhanced Coupling in Nanocrystal Solids. *Journal of the American Chemical Society* **133**, 15753-15761, doi:10.1021/ja206303g (2011).
155 Nag, A. *et al.* Metal-free Inorganic Ligands for Colloidal Nanocrystals: S2-, HS-, Se2-, HSe-, Te2-, HTe-, TeS32-, OH-, and NH2- as Surface Ligands. *Journal of the American Chemical Society* **133**, 10612-10620, doi:10.1021/ja2029415 (2011).
156 Knowles, K. E., Frederick, M. T., Tice, D. B., Morris-Cohen, A. J. & Weiss, E. A. Colloidal Quantum Dots: Think Outside the (Particle-in-a-)Box. *Journal of Physical Chemistry Letters* **3**, 18-26, doi:10.1021/jz2013775 (2012).
157 Peterson, M. D. *et al.* The Role of Ligands in Determining the Exciton Relaxation Dynamics in Semiconductor Quantum Dots. *Annual Review of Physical Chemistry, Vol 65* **65**, 317-339, doi:10.1146/annurev-physchem-040513-103649 (2014).
158 Choi, J. J. *et al.* Controlling Nanocrystal Superlattice Symmetry and Shape-Anisotropic Interactions through Variable Ligand Surface Coverage. *Journal of the American Chemical Society* **133**, 3131-3138, doi:10.1021/ja110454b (2011).

159 Nadeau, J. L., Carlini, L., Suffern, D., Ivanova, O. & Bradforth, S. E. Effects of beta-Mercaptoethanol on Quantum Dot Emission Evaluated from Photoluminescence Decays. *Journal of Physical Chemistry C* **116**, 2728-2739, doi:10.1021/jp209832h (2012).